POLITECNICO
MILANO 1863

SCUOLA DI INGEGNERIA INDUSTRIALE
E DELL'INFORMAZIONE

Calibration of a cardiac electro-mechanics model in view of Cardiac Resynchronization Therapy

TESI DI LAUREA MAGISTRALE IN
MATHEMATICAL ENGINEERING - INGEGNERIA MATEMATICA

Author: **Emilia Capuano**

Student ID: 945025
Advisor: Prof. Christian Vergara
Co-advisors: Simone Stella
Academic Year: 2021-22

Abstract

The mathematical modelling of heart function aimed at supporting clinical therapies for cardiac electrophysiology has made great progress in the last two decades. The focus of this thesis is on the Cardiac Resynchronization Therapy (CRT), that is a medical procedure consisting in the implantation of a device that is able to send electrical stimuli to heart chambers using three wires, called leads. This technique is adopted to restore a coordinated ventricular contraction and improve systolic function in heart failure (HF) patients presenting ventricular dyssynchrony (VD), usually due to a *left bundle branch block* (LBBB) condition, which is a disorder of the cardiac conduction system of the heart leading to a late electrical and mechanical activation of the left ventricle (LV). However, since 30% of patients undergoing CRT implantation are non-reponders, the procedure needs to be optimized.

This work analyzes three patient-specific cases provided by the Hospital of S. Maria del Carmine in Rovereto (TN), Italy, that were diagnosed with LBBB and were treated with Cardiac Resynchronization Therapy.

The primary objective of the thesis is to use pre-CRT clinically measured electrical and mechanical data and reconstructed patients' LV geometries to perform the first complete calibration of an existing electromechanical (EM) computational model of the left ventricle, the *Eikonal-Reaction-Mechanics* (ERM) model, estimating the physical parameters that can reproduce the *pre-operative* scenario in the most accurate way.

After this preliminary phase, *virtual* CRT scenarios can be simulated using the patients' calibrated models, imposing the points of electrical stimulation along the LV external surface to surrogate the leads of the CRT device. Based on clinical and computational studies reported in literature, the settings to be varied for optimization of the procedure are identified together with suitable biomarkers evaluating acute outcomes of the therapy. At the end of every simulation obtained changing CRT settings, such biomarkers are computed from the numerical solution and the *optimal virtual* scenario is identified for every patient.

Keywords: Cardiac Resynchronization Therapy, Left Bundle Branch Block, Ventricular Dyssynchrony, Left Ventricle Electromechanics, ERM model, Patient-specific Calibration

Abstract in lingua italiana

La modellistica matematica della funzionalità del cuore a supporto delle terapie cliniche per l'elettrofisiologia cardiaca ha fatto grandi progressi negli ultimi due decenni. Questa tesi si focalizza sulla Terapia di Resincronizzazione Cardiaca (CRT), una procedura medica che consiste nell'impianto di un dispositivo capace di inviare impulsi elettrici alle camere cardiache per mezzo di tre cavi. Questa tecnica è utilizzata per ripristinare la coordinazione nella contrazione ventricolare e per migliorare la funzione sistolica in pazienti con insufficienza cardiaca e dissincronia ventricolare, spesso causata dal *blocco di branca sinistra* (LBBB), un disturbo del sistema di conduzione cardiaca che porta a un ritardo nell'attivazione elettrica e meccanica del ventricolo sinistro (LV). Tuttavia, è necessario riuscire ad ottimizzare la terapia CRT, dal momento che circa il 30% dei pazienti non ne beneficia.

Questo lavoro analizza tre casi clinici di pazienti con diagnosi di LBBB e trattati con la CRT, forniti dall'Ospedale di S. Maria del Carmine di Rovereto (TN), Italia.

L'obiettivo primario della tesi è usare dati clinici pre-CRT elettrici e meccanici e geometrie dei pazienti ricostruite per ottenere una prima calibrazione completa di un modello elettromeccanico già esistente per il ventricolo sinistro, il modello *Eikonal-Reaction-Mechanics* (ERM), stimando i parametri che garantiscano la migliore accuratezza nel riprodurre il contesto *pre-operatorio*.

Dopo questa fase preliminare, la CRT può essere riprodotta virtualmente utilizzando il modello calibrato sul paziente, scegliendo dei punti lungo la superficie ventricolare esterna che possano surrogare gli elettrodi del dispositivo CRT. Partendo da studi clinici e computazionali in letteratura, sono state identificate le impostazioni della terapia da variare al fine di ottimizzarla, insieme a dei biomarker appropriati che possano valutarne i risultati in acuto. Al termine di ogni simulazione, ottenuta variando tali impostazioni, vengono calcolati i biomarker a partire dalla soluzione numerica, in modo da identificare per ogni paziente lo scenario *virtuale* migliore.

Parole chiave: Terapia di Resincronizzazione Cardiaca, Blocco di Branca Sinistra, Dissincronia Ventricolare, Elettromeccanica del ventricolo sinistro, Modello ERM, Calibrazione paziente-specifica

Contents

1 | Introduction

Cardiovascular diseases (CVDs) are the first cause of morbidity and mortality globally, taking 17.9 million lives each year. In 2019 they represented the 32% of all global deaths, as reported in [136]. CVDs affect the function and/or the structures of the heart. Some examples are arrhythmias, congenital heart disease, coronary artery disease, heart attack, heart muscle disease (cardiomyopathy), heart failure, cardiac conduction disorders.

Besides advances in medical research oriented to the treatment of these diseases, in the last decades mathematics has assumed an important role in this field. Several mathematical and numerical models have been developed in order to describe and virtually reproduce the physics governing the cardiovascular system [100], with the purpose of better understanding its functioning and provide answers to clinical problems.

In this thesis we will address the clinical condition of ventricular dyssynchrony (VD), arising when the ventricles of the heart fail to beat in a coordinated pattern. This phenomenon can emerge as a consequence of different pathologies, such as heart attack, arrhythmias or other electrical conduction disorders (like left bundle branch block). The most common treatment for this pathology is Cardiac Resynchronization Therapy (CRT), which consists in the implantation of a device, called biventricular pacemaker, that sends electrical signals to both right and left ventricles forcing them to contract in a more coordinated way.

In order to study and reproduce the pathological scenario of VD and consequently optimize the outcome of CRT, we will use a patient-specific mathematical model describing left ventricular activity, consisting of a set of equations for the electrical activation, the mechanical contraction and relaxation of the cardiac muscle coupled with a simplified fluid dynamics model for blood circulation.

Outline

The thesis is structured as follows:

- Chapter 1 gives an overview of cardiac anatomy, physiology and the main pathologies addressed in this work together with their diagnosis. Then, the implantation

procedure and the optimization techniques of Cardiac Resynchronization Therapy are explained. Finally the state of the art of computational electromechanical methods and the aim of the present thesis are addressed.

- Chapter 2 presents the mathematical formulation of the coupled electromechanical (EM) model employed in this work and its numerical approximation in time and space, the latter is carried out using the Finite Element Method (FEM). Additionally, a brief digression on the necessary geometric information to be included in the model is given.

- Chapter 3 focuses on the personalization of the EM model on patient-specific cases coming from the Hospital of S. Maria del Carmine in Rovereto (TN), Italy. First the reconstruction of patient-specific geometries and anatomical structures is addressed. Then, the procedure for the tuning of electrical, mechanical and hemodynamic parameters is explained and the final results of calibration are showed for every patient.

- Chapter 4 exhibits the use of the EM computational model to simulate different virtual scenarios of CRT obtained varying the settings of the therapy. The final aim is CRT optimization on a patient-specific level defining suitable quantities to evaluate acute outcomes of each simulated CRT procedure.

- Chapter 5 draws conclusions of the present work, addressing its limitations and possible future developments to improve the simulation and evaluation of an optimal virtual CRT.

1.1. Anatomo-physiology of the heart and the Clinical Problem

1.1.1. Anatomy

The heart is a muscular pump exploiting two complementary functions:

1. collecting deoxygenated blood from the tissues of the body and pump it to the lungs to pick up oxygen and release carbon dioxide.

2. collecting oxygenated blood from the lungs and pump it to all tissues of the body.

The heart assumes an oblique position in the thorax, with two-thirds to the left of midline of the thoracic cavity.
The internal anatomy of the heart, extensively discussed in Chapter 4 of [57], is composed of four chambers (see Figure 1.1).
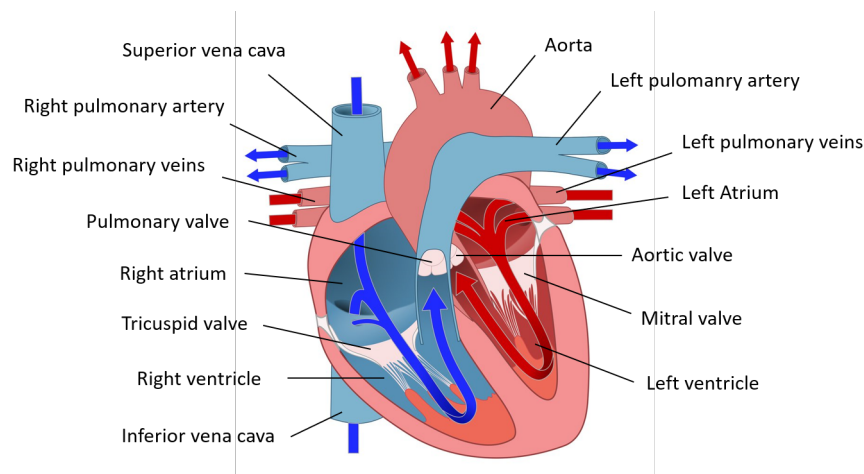
Figure 1.1: Cardiac anatomy and blood circulation in the chambers (taken from [5])

The right and left atria (RA and LA) are the two upper chambers and their main function is to collect blood, they are separated by a wall-like structure called *interatrial septum*. The right and left ventricles (RV and LV) are the two lower chambers, which are much stronger and function to pump blood and the *interventricular septum* is the structure dividing them. All four chambers are connected to the circulatory system: the LV through the *Aorta*, the RV through the *pulmonary arteries*, the LA through the *pulmonary veins*, and the RA through the *superior and inferior venae cavae*. The last important components allowing blood to flow in one direction are the valves, which prevent backflow. The atrioventricular valves (*tricuspid* between RA and RV, *bicuspid* or *mitral* between LA and

LV) allow blood to flow only from atria to ventricles: they open when atrial pressure is higher than ventricular pressure and they close when blood flow becomes retrograde. The semilunar valves (*pulmonary* between RV and pulmonary artery and *aortic* between LV and Aorta) allow blood to flow only from the ventricles out of the heart and through the great arteries with a mechanism that is similar to the one described above for atriventricular valves.

The path of blood flow (Figure 1.1) in the right heart starts in the RA where blood enters through the superior and inferior venae cavae, it is pumped into the RV and subsequently into the pulmonary circulation through the pulmonary valve. Afterwards, lungs oxygenate blood, which returns to the LA through the pulmonary veins, it enters the LV and finally it is pushed into the systemic circulation through the main artery, the aorta, through the aortic valve.

The wall of the heart is made of three layers (see Figure 1.2): the outer *pericardium*, the middle *myocardium* and the inner *endocardium*, [83]. The pericardium protects the heart reducing friction and its internal component, in contact with the heart, is the *epicardium*. The myocardium is the cardiac muscle and it is responsible of pumping blood out of the heart. In conclusion, the endocardium is made up of connective tissue and it has specialized cardiac muscle fibers called *Purkinje fibers*.
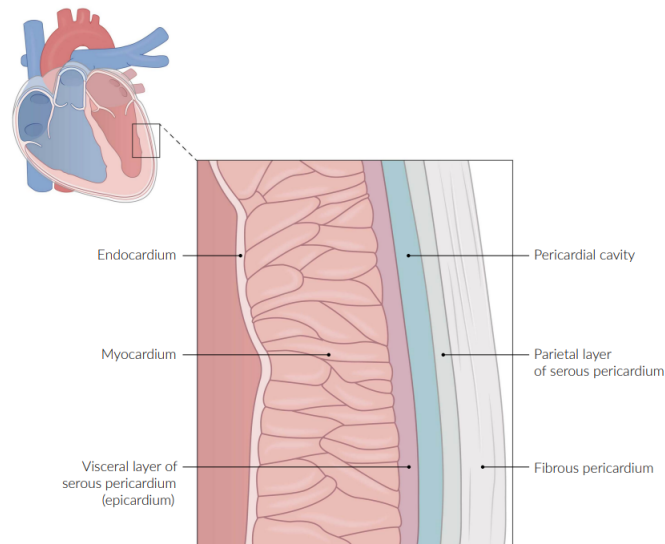
Figure 1.2: Layers of the heart wall (taken from [4])

The conduction system

The mechanical contraction of the heart is regulated by the transmission of electrical impulses that pass through specialized cardiac muscle cells (the *cardiac conduction system*, CCS) located within the myocardium, that ensure synchronous contraction of the left and right sides of the heart and the sequential contraction of the atria and ventricles [90]. An exhaustive description of conduction system anatomy and functioning is reported in Chapter 9 of [57]. Following an initiating activation (*depolarization*) inside the myocardium, this electrical excitation spreads throughout the heart in a rapid and coordinated way.

The main components of the conduction system [83] are the following (see Figure 1.3):

- The *sinoatrial node* (SA node) is the natural pacemaker of the heart, because its cells manifest spontaneous depolarization, initiating activation.

- The *atrioventricular node* is the normal conduction pathway between atria and ventricles.

- the *bundle of His* let the signal pass into the interventricular septum.

- The *right and left main bundle branches* arise from the bundle of His and run along the two sides of septum.

- The *Purkinje fibers* originate from the bundle branches, curve around the ventricles and pass over their lateral walls, they act as preferential conduction pathways to provide rapid ventricular activation and coordinate the excitation pattern within the regions of the ventricular myocardium.
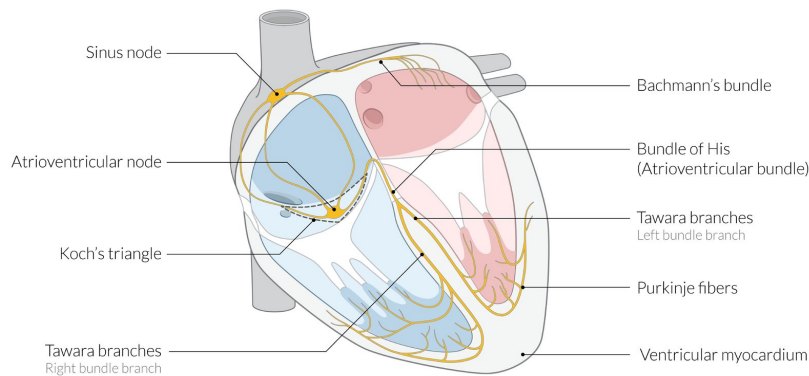
Figure 1.3: Conduction system anatomy (taken from [5])

The coronary system

Myocardium itself needs blood supply in order to function efficiently. This is guaranteed by the *coronary system*, which is a complex of vessels running along the epicardium. The three primary components of the coronary system are the *coronary arteries*, the *capillaries* and the *coronary veins* (see Chapter 6 of [57] for a detailed description).

In this thesis we will deal with coronary veins anatomy and their location on the left ventricle surface, in order to simulate different CRT scenarios, but we give here a very brief description of the whole coronary system for completeness.

The main coronary arteries are the *right coronary artery* (RCA), the *posterior descending artery* (PDA), the *left circumflex* (LCX) and *left anterior descending* (LAD) arteries. Their function is to supply blood to the myocardium.

Capillaries are very thin vessels whose task is to ensure every myocyte (i. e. a muscle cell) receives nutrients and they serve as connection between arterial and venous system. Finally, we focus on the component of the coronary circulation that is more of interest for us: the system of cardiac veins (Figure 1.4).
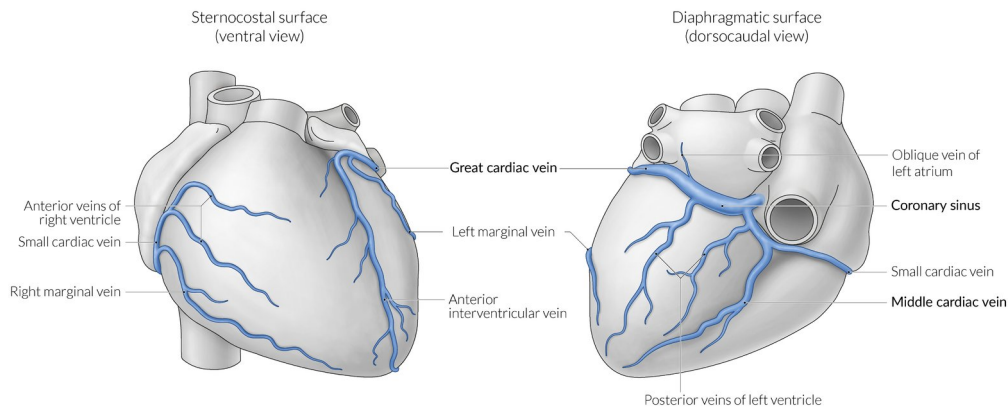
Figure 1.4: Coronary veins (taken from [4])

The most important coronary vein is the *coronary sinus* (CS), which is on the posterior surface of the heart in the left atrioventricular groove. The main vessels flowing into the CS are the *great cardiac vein*, the *oblique vein of Marshall*, the *lateral and posterior veins* of LV, the *middle cardiac vein* and the *small cardiac vein*. The *anterior interventricular vein* (i. e. great cardiac veins) drains the circulation of the ventricular septum and anterior ventricular walls. The oblique vein of Marshall enters the CS traveling along the posterior surface of the left atrium. The middle cardiac vein runs along the posterior surface of the LV alongside the PDA. The small cardiac vein drains the right ventricular and right atrial circulation.

1.1.2. Physiology

The main function of the heart is to maintain blood circulation and ensure blood supply to the body through its continuous pumping action. In order to accomplish this task, the cardiac muscle is able to exceed the resistance in the arteries (blood pressure of about 70 $mmHg$ in the aorta and 10 $mmHg$ in the pulmonary artery) due to the reaction of the elastic vessel wall to the deformation induced by blood flow.

The energy needed for pumping blood (see Chapter 5 of [100]) is obtained by the consumption of oxygen that is provided to the heart by the coronary circulation.

Electrical Propagation

The most significant phenomenon responsible of blood ejection is ventricular contraction, which is allowed by the transmission of electrical impulses that pass through the cardiac conduction system thanks to the propagation of an electrical potential along the myocardium, called *action potential*. The action potential (AP) occurs thanks to the ability of *cardiomyocytes* (Chapter 8 of [57]), the heart cells, to generate a variation in *transmembrane (or membrane) potential*, defined as the difference in electrical potential between the interior and the exterior of the cells. The change in membrane potential is due to several ion channels that open and close letting a ionic current (mainly of sodium Na^+, calcium Ca^{2+} and potassium K^+) pass through the cell membrane. The AP has five phases [90, 113] represented in Figure 1.5a:

1. *Phase 0 - Depolarization*: "Fast" Na^+ ionic channels open letting a flow of positive ions enter the cell, causing an increase of membrane potential from the rest value of $\sim -90\ mV$ to $\sim 20\ mV$ in a period of about 2 ms. When the threshold of $\sim -70\ mV$ is reached, any further depolarization results in a phenomenon known as the action potential, which completely depolarizes the cell (*all-or-none law*).

2. *Phase 1 - Early Repolarization*: The potential begins to decrease due to an outward flow of K^+ ions, occurring after the inactivation of the "fast" Na^+ channels.

3. *Phase 2 - Plateau*: Na^+ and Ca^{2+} ions enter through "slow" membrane channels, but there is also a slow outward movement of K^+ ions which keeps the plateau relatively steady to 0 mV. This phase lasts for $200 - 300\ ms$ and the Ca^{2+} influx allows these ions to bind with *troponin* giving rise to the *excitation–contraction coupling* process. Meanwhile, a new AP cannot be initiated because the "fast" Na^+ channels are inactivated, we talk about *refractory period* of the cardiomyocytes.

4. *Phase 3 - Rapid Repolarization*: "Slow" Na^+ and Ca^{2+} channels become inactive,

while an efflux of K^+ ions allows for repolarization of the membrane until the normal resting potential of $\sim -90\ mV$ is reached and normal transmembrane ionic concentration gradients are restored.

5. *Phase 4 - Resting*: The cell returns to its excitable state and the potential remains constant until the next electrical stimulation thanks to a constant outward flow of K^+.
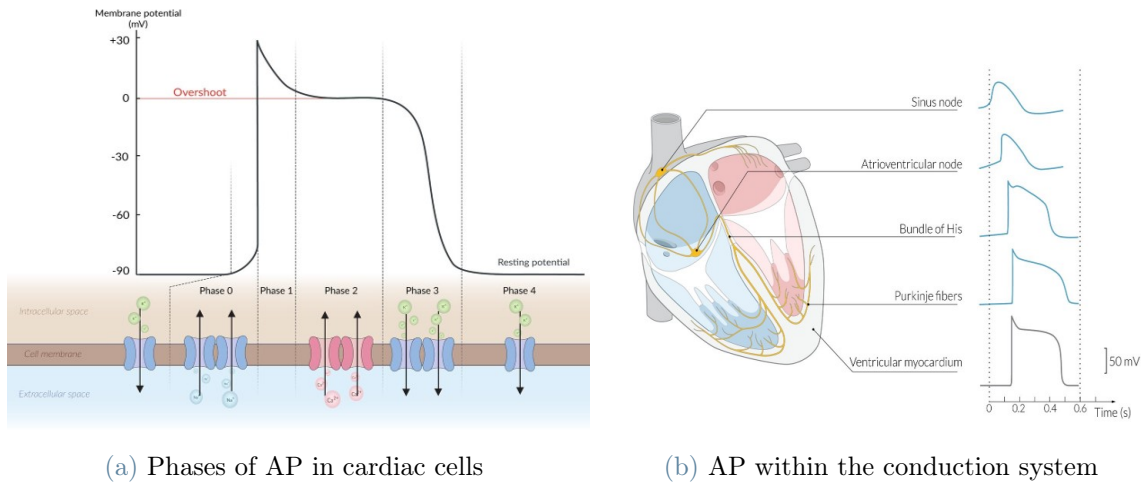
(a) Phases of AP in cardiac cells   (b) AP within the conduction system

Figure 1.5: Action potential trend (taken from [5])

The transmission of the electrical potential from a single cell to the neighbouring ones is possible thanks to the presence of *gap junctions*, which are channels with low resistance located between cardiomyocytes membranes.

The path followed by the electrical signal is the following (Figure 1.5b):

1. The electrical excitation first starts in the SA node, which imposes its rhythm on the entire myocardium (*sinusal rhythm* $\sim 60 - 90$ heartbeats per minute) and it is propagated to cardiomyocytes of the atria causing their almost simultaneous contraction.

2. The conduction velocity is faster in the direction of the ventricles ($\sim 200\ cms^{-1}$), allowing the electrical impulse to arrive to the AV node, that gives the pace to all ventricle stimulation, where the propagation is delayed of $\sim 120\ ms$ because of the small diameter of the fibers. This delay allows complete contraction of the atria and ventricular filling before ventricles contraction starts.

3. The depolarization wave is propagated along the interventricular septum through the bundle of His and to the ventricles via the two bundle branches, with a fast conduction of about $\sim 350\ cms^{-1}$.

4. Finally, the signal arrives to Purkinje fibers which propagate it to the entire endo-cardium almost simultaneously and, through *Purkinje muscle junctions*, i. e. the terminal points of Purkinje network, all myocardium is activated towards the epi-cardium after a delay of $\sim 10\ ms$ with a reduced conduction velocity of $\sim 80\ cms^{-1}$.

In this work the focus will be on the ventricular spreading of electrical signal, in particular in the left ventricle. The electrical propagation in the ventricles occurs along the *fibers direction*, intended as a macroscopic average cell orientation which varies when passing from the endocardium to the epicardium. The velocity of the electrical potential is twice along the fibres compared to the other directions. Fibers are in turn organized in *sheets* of collagen. Therefore, we can distinguish three different directions: fibers, sheets and normal (see Section 2.3.2 in Chapter 2).

Cardiac Cycle

In a normal scenario, heart chambers contract in a coordinated way in order to pump blood efficiently. The contraction phase is called *systole* (atrial and ventricular), the relaxation phase is *diastole*, ventricular systole happens during atrial diastole and vice versa. We can distinguish between right and left heart: the right heart collects venous blood, while the left heart pumps oxygenated blood, but the mechanism of collection and consequent ejection of blood is the same but for pressure values.

We focus on the left heart and describe the cardiac cycle dividing it in 4 phases. Table 1.1 sketches the correlation in time of electrical and mechanical events during a cardiac cycle. The behavior of pressures, volumes and potential in the left heart during a heartbeat are represented in Figure 1.6.

1. *Isovolumetric Contraction* (IVC): After atrial contraction, LV is filled with blood and starts contracting (while LA relaxes) causing a pressure increase that makes the mitral valve close because of retrograde flow. Once the valve is closed, vol-ume is maintained constant because of blood incompressibility, and it is called *End Diastolic Volume* (EDV).

2. *Ejection*: Pressure in LV eventually reaches the pressure threshold of $\sim 70\ mmHg$ characteristic of the aorta, causing the opening of the aortic valve with consequent flow in the main artery. As long as LV contraction goes on, pressure keeps increasing whilst volume begins to decrease. When pressure also starts decreasing, it provokes negative blood flow that cause the closing of the aortic valve.

3. *Isovolumetric Relaxation* (IVR): once the aortic valve is closed, the ventricle starts relaxing without a change in volume, whose value is indicated as *End Systolic Vol-*

ume (ESV), resulting in a pressure drop.

4. *Ventricular Filling*: When atrial pressure exceeds ventricular pressure, mitral valve opens at ~ 10 $mmHg$ and blood begins flowing from LA to LV, first in a passive way and in a second phase the atrium starts actively contracting in order to eject all remaining blood.
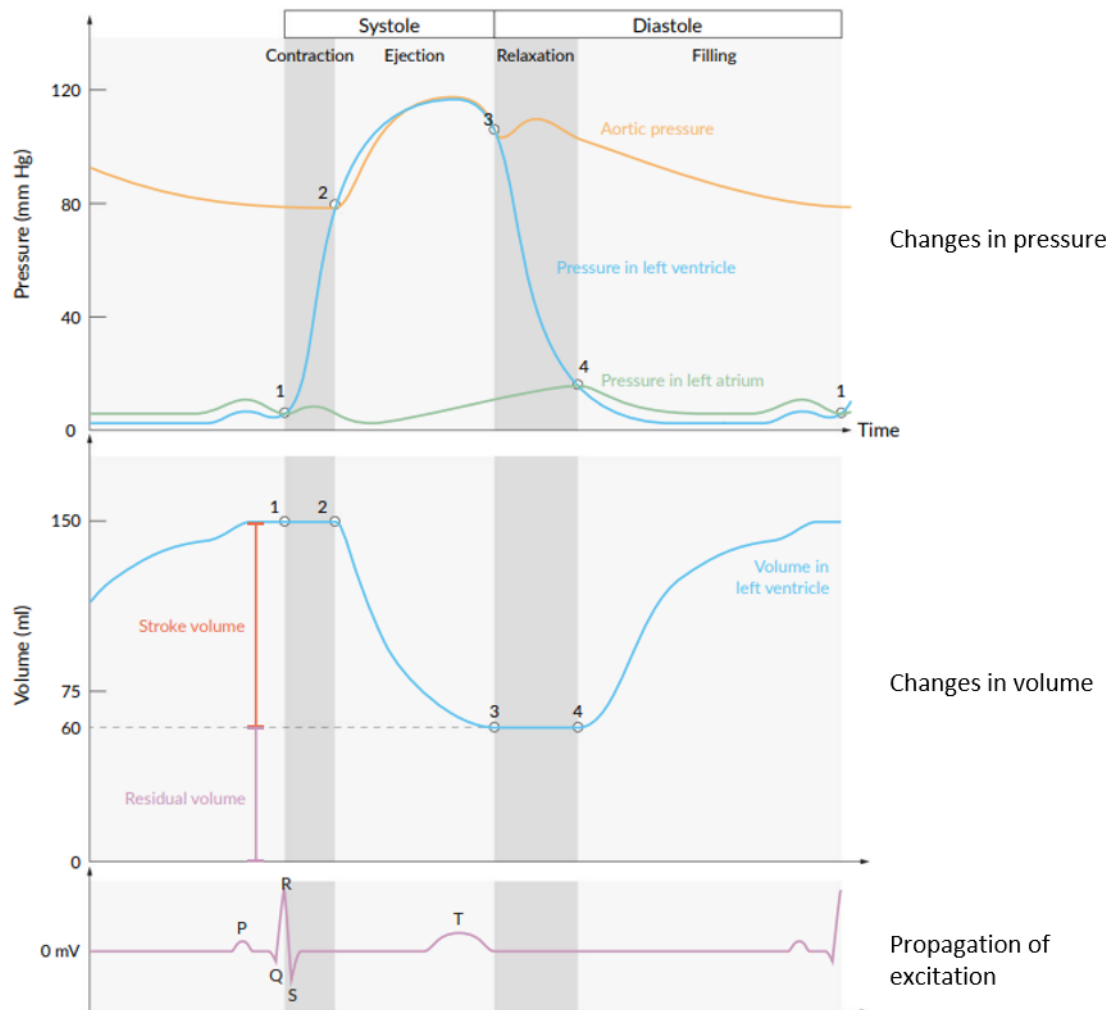
Figure 1.6: Phases of the cardiac cycle in the left heart (taken from [5]). In the propagation of excitation plot: P wave is atrial depolarization originating in the SA node, QRS complex is ventricular depolarization, T wave is ventricular repolarization.

A common plot used to measure cardiac performance and that gives a more clear idea of the cardiac cycle is the *pressure-volume diagram*, for simplicity PV loop. An example is reported in Figure 1.7.

Location	Electrical event	Time [ms]	ECG	Mechanical event
SA node	Impulse generation	0		
Atria	Activation	0 − 85	P	Atrial systole starts
AV node	Impulse arrival	50		
	Impulse departure	125		Atrial systole ends
Purkinje fibers	Activation	125 − 150		
Endocardium (septum)	Depolarization ends	175	R peak	IVC starts
Endocardium (LV)	Depolarization ends	190		
Epicardium (LV)	Depolarization ends	225	S	IVC ends

Table 1.1: Correlation between electrical and mechanical events in LV
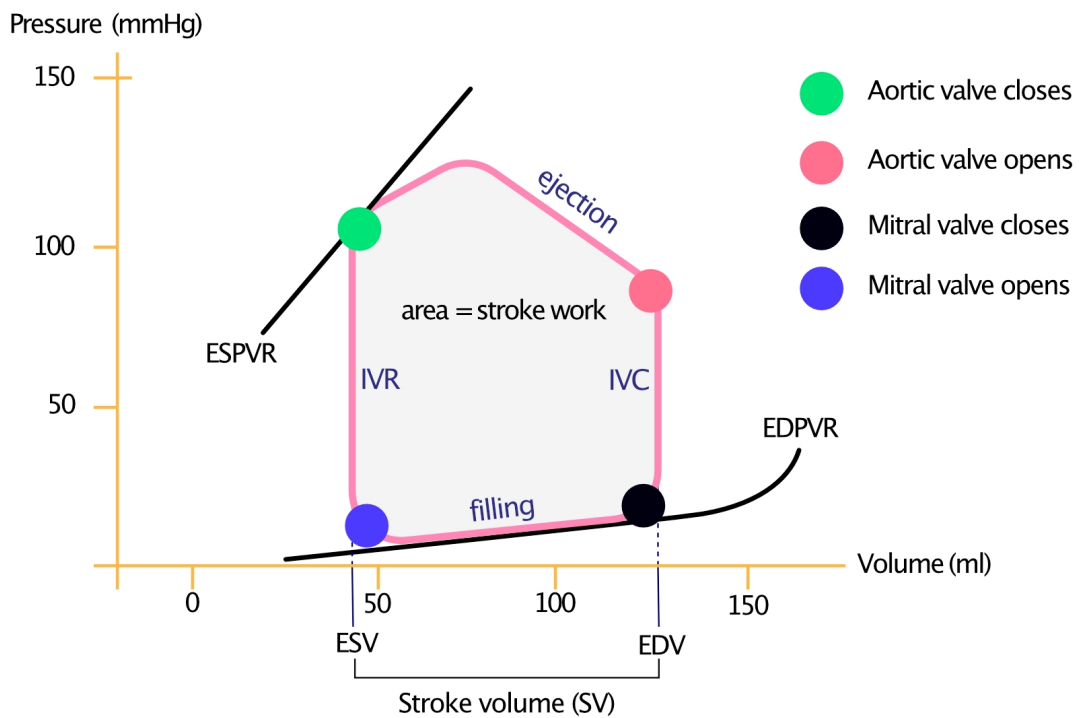
Figure 1.7: Pressure-volume diagram in the LV during a cardiac cycle (taken from [42])

Clinical Quantities of Interest

Some relevant quantities that can be easily recovered from the PV loop are the following:

- *End Diastolic Volume, EDV*

- *End Systolic Volume, ESV*

- *Stroke Volume, SV* defined as

$$SV = EDV - ESV$$

  . Physiological value is around $95mL$ [78].

- *Ejection Fraction, EF* defined as

$$EF = \frac{SV * 100}{EDV}.$$

  It is the percentage of blood volume ejected in each cardiac cycle and it is a representation of LV systolic performance [31]. Physiological value is between $52\% - 74\%$, EF below 50% suggests disease and below 30% is associated with high mortality. [31].

- *Stroke Work, SW* is the area within the loop. It represents the work needed to move blood from LV into the aorta [42].

- *End Systolic Pressure, ESP*, is the peak pressure reached during the cardiac cycle. It corresponds to the *aortic valve closing pressure, P_{AVC}*.

- *End Diastolic Pressure, EDP*, is the pressure value attained at the end of the ventricular filling phase. It corresponds to the *mitral valve closing pressure, P_{MVC}*.

- *Mitral valve opening pressure P_{MVO}*.

- *Aortic valve opening pressure P_{AVO}*, commonly called *diastolic pressure.*

- *Cardiac Output, CO* defined as

$$CO = SV * HR.$$

  It is the amount of blood pumped per minute. HR is the *heart rate.*

- *End Diastolic Pressure-Volume Relationship, EDPVR*

- *End Systolic Pressure-Volume Relationship, ESPVR*

1.1.3. Electrical Disfunctions and Dyssynchrony

As one can infer in Section 1.1.2, well functioning of the cardiac conduction system ensures a correct electrical propagation in the whole cardiac muscle, in terms of velocity and path of the impulse, and consequently a coordinated mechanical contraction, since it is triggered by the electrical activation of cardiomyocytes (*excitation-contraction* coupling). There are some pathologies, going under the name of *conduction disorders* [26, 85], characterized by an electrical signal which is not produced properly and/or it does not travel along the heart following the physiological path described in previous sections. When this kind of diseases appear, they also affect the mechanical behavior of myocardium altering contraction capacity and synchronism. There are many types of conduction disorders that can happen anywhere along the CCS: at the SA node, the AV node, or the bundle branches [85]. What causes some of these pathologies, like sick sinus syndrome and bundle branch blocks, is aging, because of normal changes to the conduction system when getting older [26]. Other conditions can be genetic or due to autoimmune diseases, heart and blood vessel diseases, muscular dystrophy, problems with thyroid hormone levels, but also some medicines that treat other heart conditions or mental illnesses.

Left Bundle Branch Block

Bundle branch block, right (RBBB) or left (LBBB), denotes a conduction defect in one of the bundle-branches, which can occur in a single portion of the bundle branch or in several distinct areas of the CCS. The consequence is that activation of the ventricle located on the side of the block must await initiation by the opposite ventricle.
In LBBB, due to the block of the left bundle branch, RV activation occurs first, it is then transmitted to the LV endocardium usually at the level of the mid-septum and it is propagated with a delay but still homogeneously to the rest of the LV (Figure 1.8), the latest site of activation occurs in the lateral basal area of the epicardium [122].
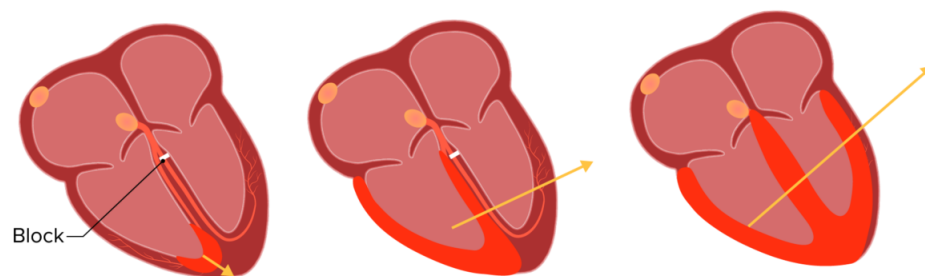
Figure 1.8: Electrical conduction and ventricular contraction on the left and LBBB scenario on the right (taken from [87])

Therefore, the electrical activation sequence is significantly prolonged during LBBB, and can reduce LV pump function substantially [50, 94].

Usually, LBBB is present in the patient together with other cardiac diseases [18], like ischaemic heart disease, hypertension, dilated cardiomyopathy. Moreover, LBBB is the most common conduction disorder in patients with advanced heart failure (HF), appearing in 30% of them [121]. The term *heart failure* refers to the reduced ability of the heart to pump or fill with blood leading to an abnormal cardiac output [107].

Cardiac Fibrosis

Cardiac fibrosis is another noteworthy condition for the purposes of the thesis. It is a scarring process characterized by the *cardiac fibroblast* (typical cells of connective tissue) activation and differentiation into myofibroblasts and excessive deposition of collagen [39]. The consequence is mechanical stiffness and diastolic dysfunction, leading to the development of cardiac arrhythmias. Increased collagen deposition results in myocyte electrical decoupling, affecting both electrical conduction and impulse formation [39, 55].
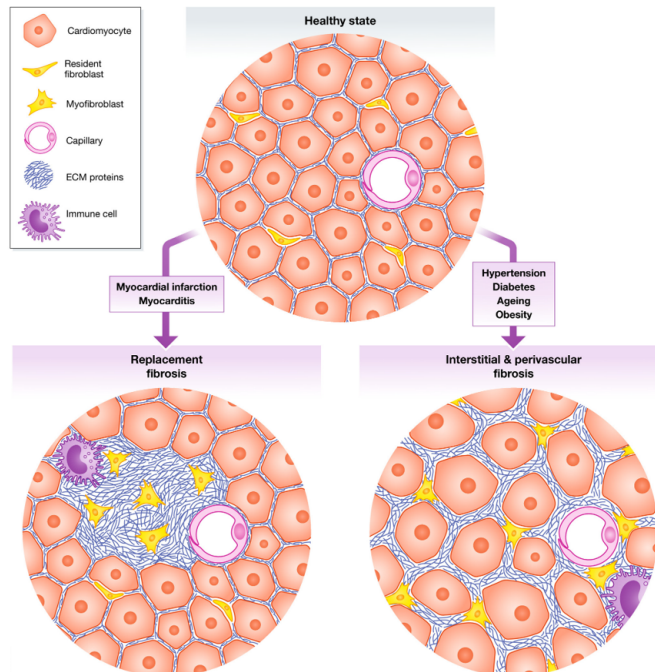
Figure 1.9: Myocardial fibrosis (taken from [120])

Two forms of fibrosis can be distinguished (Figure 1.9): *interstitial fibrosis* [32] characterized by progressive increase in the extracellular space between cardiomyocytes and *replacement fibrosis* [32, 39] consisting in the formation of collagen-based scars to replace dead cardiomyocytes in response to cardiac injury. Fibrotic scars of the cardiac muscle

often occur after *myocardial infarction*, commonly known as heart attack, in which blood flow in coronary arteries is decreased or stopped. Other conditions leading to cardiac fibrosis are hypertensive heart disease, diabetic hypertrophic cardiomyopathy and idiopathic dilated cardiomyopathy [39, 55].

Ischemic heart disease and endomyocardial fibrosis are in turn the primary causes of end-stage heart failure [55].

Ventricular Dyssynchrony

*Electrical dyssynchrony* is associated to a higher conduction time in the ventricles detected through a prolonged QRS duration [111]. This leads to *mechanical dyssynchrony*, which denotes a mechanical discoordination due to simultaneous contraction and stretch in different segments of LV. Ventricular dyssynchrony (VD) can be either *interventricular* or *intraventricular* [65, 111]:

- *Interventricular dyssynchrony* occurs when LV and RV does not contract simultaneously, because the whole LV is activated with a delay.

- *Intraventricular dyssynchrony* consists in an abnormal movement of LV because there is a part of the chamber which is activated with a delay with respect to the rest of the ventricle. It leads to LV contraction that is inferior in both effectiveness and energy efficiency.

When the timing of ventricular contractions is not synchronous, the ability of the cardiac muscle to pump blood is reduced and blood can accumulate in the ventricles, possibly leading to *congestive heart failure* [65, 71]. Indeed, the hemodynamic consequences of ventricular dyssynchrony are decreased SV and SW, a slower rate of rising of LV pressure ($dP/dt|_{max}$) and increased LV end-systolic wall stress [68, 111]. Approximately 50% of HF patients have significant mechanical dyssynchrony. This percentage increases if an electrical conduction defect is present [94, 139].

Dyssynchrony is often itself the consequence of an underlying degenerative conduction system disease and/or a dilated ventricle (dilated cardiomyopathy) [71]. Indeed, LBBB is a major cause of ventricular dyssynchrony, because of the resulting abnormal electrical conduction in LV. The ventricular septum is activated during isovolumetric contraction before aortic valve opening causing a stretch of the other regions of the ventricular wall, vice versa posterior and lateral walls are activated later in systole with consequent passive stretching of the septal wall. This dyssynchronous motion extends isovolumic contraction and relaxation times and results in decreased contraction efficiency [122].

Moreover, the study reported in [77] also demonstrated that LV myocardium regional

variation in interstitial fibrosis is closely related to LV intraventricular dyssynchrony. VD and fibrosis might reinforce with each other forming a vicious cycle: myocardial fibrosis might have adverse effects on myocyte excitability, cell-to-cell coupling and impaired intracellular and intercellular calcium handling, all of which are potential mechanisms leading to dyssynchrony [69]; on the other hand, VD can cause regional variations in interstitial fibrosis because of higher stretches in late-activated regions [76].

1.1.4. Diagnosis

The diagnosis of **left bundle branch block** is performed using two main tools [80]:

- *Electrocardiogram* (ECG or EKG) which records electrical activity of the heart via electrodes positioned on the body surface (Figure 1.10).

- *Echocardiogram* which provides images of the heart's structure and thickness by means of sound waves. It can be used to detect the cause of the block.
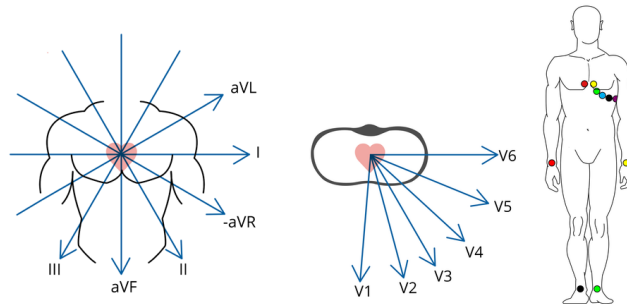
Figure 1.10: Electrode locations of 12-lead ECG: 4 on the extremities and 6 on the thorax (taken from [19])

In particular, detecting LBBB is easy through ECG measurements observing the QRS complex duration and morphology, see [122] for details. QRS complex duration greater than 120 *ms* is usually an index of the presence of LBBB.

Concerning **cardiac fibrosis** detection, the gold standard is the measurement of the interstitial collagen content using *endomyocardial biopsy* (EMB) [39, 55, 59]. However, since this procedure is really invasive, imaging techniques or *serum collagen biomarkers* may be used [59]. *Diffusion-weighted MRI* (DW-MRI) generates contrast in MRI images using water molecules and it is becoming a very powerful tool for fibrosis detection, even if it is not a common procedure in daily clinical practice [113]. Contrast-enhanced *cardiac*

magnetic resonance imaging (CMRI) or *cineCMRI*, the most common methods for determining LV volume and mass [55], are the reference non-invasive imaging techniques for fibrosis detection through the identification of interstitial fibrosis as hyperenhanced bright areas [32, 39], with the drawback of being very expensive. A particular MRI sequence that is frequently used is *steady-state free precession (SSFP)* imaging or *cineSSFP*.

Once MRI images are acquired, a common technique used to infer information about fibrosis distribution in the LV myocardium is the 17-segment division model, called *bullseye plot* [20]. The LV endocardium surface is subdivided into 17 regions (see Figure 1.11) and each region can be identified as healthy or fibrotic, eventually with its degree of diffusion [113].

Basal portion:
1 – Anterior
2 – Anteroseptal
3 – Inferoseptal
4 – Inferior
5 – Inferolateral
6 – Anterolateral

Mid portion:
7 – Anterior
8 – Anteroseptal
9 – Inferoseptal
10 – Inferior
11 – Inferolateral
12 – Anterolateral

Apical portion:
13 – Anterior
14 – Septal
15 – Inferior
16 - Lateral
17 – Apex
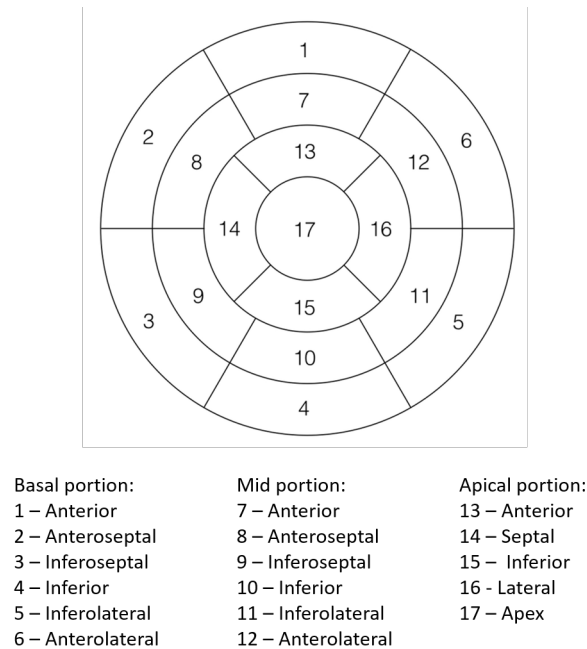
Figure 1.11: LV bullseye plot

In conclusion, the diagnosis of **left ventricular dyssynchrony** (i. e. intraventricular dyssynchrony) is principally assessed through echocardiografic techniques, like M-mode, Tissue Doppler imaging (TDI), speckle tracking echocardiography (STE), 3D echocardiography [111], [128], and the subsequent evaluation of indices indicating the presence of dyssynchrony:

- Septal to posterior wall motion delay (SPWMD) [68], obtained with M-mode, is defined as the time difference between septal and posterior wall contraction. SPWMD $> 130\ ms$ is considered pathological [81].

- Interventricular mechanical delay (IVMD) [128], obtained with pulsed-wave Doppler

signals in a standard echocardiogram, is the delay in onset of outflow between the LV and RV. LV dyssynchrony lengthens the LV pre-ejection period, increasing IVMD, a value $> 40\ ms$ is used as a determinant of the pathology.

- Standard deviation (SD) of the average timings to peak systolic velocities (Ts-SD) [111], [81], [68], starting from the onset of QRS in correspondence of different LV segments. It is measured by means of TDI and a value $> 32\ ms$ is considered as index of dyssynchrony (and a predictor of CRT response, see next paragraph 1.2).

- Maximum delay between peak systolic strain of two segments (usually anteroseptal and posterolateral walls) and SD of time to peak systolic strain, taken as dyssynchrony index of the LV (similarly to Ts-SD), are measured using speckle tracking echocardiography (STE) [60], [68] (a myocardial deformation imaging technique like TDI but covering the whole ventricular wall [68]). The cutoff value for radial dyssynchrony is around $130\ ms$ [81], [68].

- Systolic Dyssynchrony Index (SDI) [128], evaluated with 3D echocardiography which provides a dataset containing the entire LV [68], is defined as the SD of the average timings needed by multiple LV segments to reach minimum ESV, expressed as a percentage of a cardiac cycle duration [60]. Higher SDI denotes increasing intraventricular dyssynchrony and the threshold value is about 9.8% [128].

In the last decades, a huge number of studies have been carried out and showed that, although there is an association between wide QRS and mechanical dyssynchrony, ECGs are not precise enough to quantify VD and that imaging approaches, based on echocardiography and measuring tissue velocity and strain, are superior in the detection of dyssynchrony [81]. For more information about dyssynchrony indices and their cut-off values (all deriving from several clinical trials) see tables in [128] and [81].

1.2. Cardiac Resynchronization Therapy

Cardiac Resynchronization Therapy (CRT) is a treatment aimed at restoring a coordinated contraction in dyssynchronous ventricles and improving systolic function in heart failure patients with depressed ejection fraction and affected by a conduction system disorder, which in most cases is left bundle branch block [2]. The working mechanism of CRT is the optimization of the mechanical activation pattern of the LV, which is often achieved in clinical practice by pre-excitation of the region that is activated late at baseline leading to delayed intrinsic conduction [112]. This treatment is similar to having a pacemaker implanted in which RA and/or RV are excited, but in this case there is a third wire

connected to the LV (*Bi-V pacing* standing for bi-ventricular pacing) so that both sides of the heart are kept in proper rhythm [80].

Pharmaceutical efforts to improve systole have been useful in the short-term, but they revealed to be detrimental in the long-term [69]. On the other hand, CRT is the only clinical treatment that can both acutely and chronically improve cardiac systolic function while also increasing cardiac work and improving mortality and heart failure hospitalizations [69], moreover, it induces a significant reduction in LV volumes and mitral valve regurgitation [36].

1.2.1. CRT implantation procedure

A CRT implant consists of two components (Figure 1.12) [14]:

- The *device* or pulse generator, implanted under the skin, typically just below the collarbone, produces electrical impulses to coordinate the heart's pumping action and treats fast, irregular or slow heart rhythms depending on the type of CRT device:

  – CRT-P (*pacemaker*) functioning like a normal pacemaker for slow heart rhythms with the addition of a third wire allowing for coordinated ventricular contraction [14].

  – CRT-D (*defibrillator*) also includes a built-in *implantable cardioverter defibrillator* (ICD) and it is indicated for patients at risk of sudden cardiac death. It is able to detect fast heart rhythms (arrhythmias) and to deliver a shock to the heart in order to stop the abnormal rhythm, that otherwise can lead to sudden cardiac arrest [14].

- The three wires, called *leads*, transmit the electrical signals to the heart and send information about heart activity back to the device. Nowadays, they are inserted with a transvenous approach under *x-ray* guidance into a vein that leads to the heart chambers, usually subclavian or cephalic [54].

  1. The first lead is placed into the right atrium with the goal of synchronizing atrial and ventricular contractions. It can record ECGs.

  2. The second lead goes into the right ventricle passing from the superior vena cava and the RA, it usually positioned at the apex.

  3. The third lead stimulates the left ventricle epicardium by insertion in the CS and consequently in one of its tributaries.
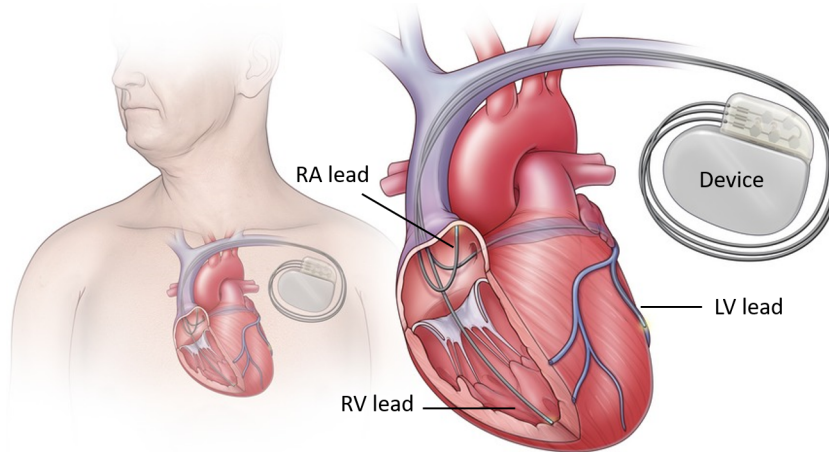
Figure 1.12: CRT implantation of device and leads (taken from [40])

The electrical signals propagating from the three leads are not simultaneous. The *atrio-ventricular delay* (AVD) is the time of activation of the RV lead with respect to the RA lead. On the other hand, the *ventriculo-ventricular delay* (VVD) or inter-ventricular delay represents the time difference between the impulse generation from the LV lead and from the RV lead. In the present work, a positive VVD will indicate that the LV is paced after a time interval equal to VVD with respect to the RV stimulation.

1.2.2. Patients Selection and Response to CRT

Patients affected by HF with reduced ejection fraction and concomitant LBBB represent a major target group for CRT [122]. In particular, 2021 guidelines for CRT implantation coming from European Society of Cardiology (ESC) and the European Heart Rhythm Association (EHRA) [49] recommend CRT for patients with HF in sinus rhythm with left ventricle $EF < 35\%$, QRS duration $\geq 150\ ms$, and LBBB QRS morphology (see Section 1.1.4). CRT may be considered but it is not recommended if either QRS duration $\geq 130\ ms$ or in presence of non-LBBB QRS morphology. Indeed, in the last two decades, also different clinical trials, like MADIT-CRT ((Multicenter Automatic Defibrillator Implantation Trial With Cardiac Resynchronization Therapy) [109] demonstrated that patients with $EF < 35\%$ and QRS duration $> 120\ ms$ would benefit from CRT in terms of HF symptoms/hospitalizations and mortality. However, in a subgroup of MADIT-CRT as well as in REVERSE trial [125], patients with QRS duration $< 150\ ms$ did not appear to benefit from CRT. Additionally, it was also shown that presence of LBBB was associated with improvement in outcomes after CRT. The effect of CRT on cardiovascular and mortality outcomes on patients with $EF > 30\% - 35\%$ remains uncertain.

Drawbacks of the procedure

After application of the current patient selection criteria, a substantial percentage of patients do not benefit from CRT [37]. This fact has been showed by several clinical studies, such as MIRACLE (Multicenter InSync Randomized Clinical Evaluation) [118] and the MIRACLE-ICD (Multicenter InSync Implantable Cardioverter Defibrillator) trials. Up to 30% of patients do not attain symptomatic benefit due to inappropriate selection for CRT, presence of myocardial scar, suboptimal LV lead position, and inadequate post-implant device programming [66].

Focusing on the first factor concerning patient selection, duration of the QRS complex is a controversial criterion to be used because of the aforementioned high percentage of non-responders. Indeed, QRS duration is a poor indicator of mechanical dyssynchrony, which is in turn an important determinant of CRT response: it has been demonstrated that the hemodynamic benefits of CRT depend on whether LV mechanical dyssynchrony can be restored [36].

Over the last two decades various studies, like the PROSPECT trial [27], have tried to identify echocardiographic markers of dyssynchrony that may predict the response to CRT (some of which are reported in section 1.1.4). However, no reliable measure had enough predictive value to be recommended as selection criteria for CRT beyond current guidelines.

1.2.3. Long and Short Term Outcomes Evaluation

When talking about CRT outcomes, it is important to distinguish between long term and short term.

In the **long-term** CRT is expected to produce symptomatic improvements in quality of life and exercise capacity in HF patients. It is associated with LV reverse remodeling and improved myocardial efficiency that may predict long-term survival.

Left ventricular *reverse remodeling* is related to LV size and function and it is typically assessed 3 –12 months after CRT. It is evaluated by reduction in LV volumes (ESV and EDV) and consequent higher EF, improved systolic and diastolic function, and decreased severity of mitral valve regurgitation [2, 72, 118]. In [112] effects of long-term CRT (after 7.2 ± 1.6 months on a relative small number of patients) on systolic and diastolic *hemodynamic parameters* were invasively evaluated observing pressure-volume loops (PV loops): CO, SV, ESV and EDV, LV EF, ESP and EDP, and maximal and minimal rate of LV pressure change ($dP/dt|_{max}$, $dP/dt|_{min}$) were measured. Similarly to MIRACLE trial results [118], increased EF and CO and decreased volumes were indices of LV re-

verse remodeling. Moreover, $dP/dt|_{min}$ reached higher values indicating improved active relaxation, while improved SW, *end-systolic elastance*, defined as $E_{ES} = ESP/ESV$ and $dP/dt|_{max}$ entailed better systolic function.

However, the degree of improvement of $dP/dt|_{max}$ between pre and post CRT may be rather a measure of response than of prognosis for long term outcomes, as showed in more recent and larger studies [119], [12]. It is better to consider the level at baseline or measured during CRT, which can predict 1-year survival.

Concerning **short term** outcomes, the hemodynamic and contractility responses can be assessed acutely after initiation of CRT and they are useful for optimization methods of the therapy, like lead placement and delays programming (AV and VV, see 1.2.4) [12].

The most common quantity used to evaluate acute heamodynamic condition is LV $dP/dt|_{max}$ [12, 119], since it occurs during isovolumetric contraction phase, it is regarded as a surrogate for contractility and an index of reshynchronization. Its significant increase was used in several studies with the aim of establishing acute hemodynamic response after settings variation of the procedure in order to obtain the optimal one [27, 34, 41, 92, 108, 124, 140, 141].

Also other parameters have been investigated besides the maximum rate of pressure change. In [106] the assessment of acute hemodynamics was made using *LV outflow velocity time integral* LVOT VTI (echocardiographic marker of SV), while acute contractility (implying acute improvement in pump function) was evaluated with the global peak of *LV radial strain*, measured via STE. Moreover, changes in PV loops were considered, including EDP for acute diastolic function [89] or ESP and *pulse pressure* $PP = ESP - ESV$ [8, 135] to evaluate acute outcomes after AV delay optimization. In [132], acute measures of dyssynchrony were assessed evaluating metrics of LV activation delay after CRT and their correlation with reverse remodeling was investigated.

1.2.4.   Optimization of the procedure

In Section 1.2.2 we discussed about clinical trials showing that up to 30% of people fulfilling selection criteria do not benefit from CRT [27]. Therefore, there is a constant research of predictors of favourable midterm and long-term outcome in order to optimize the response to the procedure. CRT non-response may be due to different factors including patient substrate and non-optimal implantation settings [74]: baseline LV dyssynchrony, optimal LV lead position, optimal AV/VV delay and extent/location of myocardial scar have been proposed as determinants of midterm and long-term outcome after CRT [37, 74].

Left ventricular lead positioning

The left ventricular pacing site is a determinant both for acute hemodynamic effects and long-term benefits of CRT for patients affected by LBBB [17, 34]. One preliminary trial that investigated the relation between LV lead location and improved CRT outcomes was the Pacing Therapies in Congestive Heart Failure (PATH-CHF) study [9], in which an association between pulse pressure (PP), $dP/dt|_{max}$ and LV pacing site was found [7]. In particular, this two parameters increased more at mid-lateral epicardial sites and, on the contrary, they had the worst increase at middle-anterior locations (Figure 1.13).
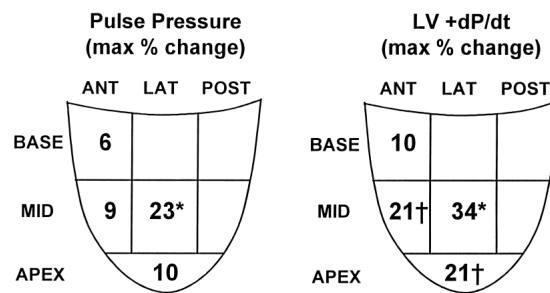

Figure 1.13: Change in systolic parameters from baseline with left ventricular pacing at multiple sites in 5 patients of PATH-CHF study. *Greater than every other site; † greater than anterior-base (taken from [7])

This finding is coherent with the fact that in LBBB cases the lateral LV wall is the last region contracting during systole (Section 1.1.3), therefore pre-excitation of the left lateral wall may decrease its delayed mechanical contraction, which may improve ventricular synchronization and pumping effectiveness [7, 17]. Additionally, PATH-CHF showed that pacing at apical or mid-anterior sites was better than pacing at the base.

Although, successive trials, MADIT-CRT [109] and REVERSE [125], proved that apical position is the worst area for LV lead placement (Figure 1.14), on the other hand, according to [109], there was no difference between anterior, posterior or lateral pacing. Detrimental effects of stimulation at the apex can be explained by the fact that the apex is generally activated early, moreover it would imply a reduced interelectrode distance from the RV lead, while the two stimulation points should be ideally positioned as far away as possible.

A further investigation [38] also assessed that pacing at the CS or at the lateral wall was rarely optimal.

Several studies based their analysis on the fact mentioned above: stimulating a later-activated LV region produces a larger response because it more effectively restores activation synchrony. Indeed, in current standard CRT procedure the LV lead is often placed
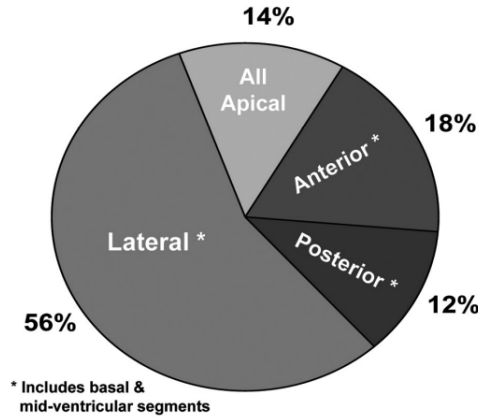
Figure 1.14: The distribution of apical vs nonapical location of the LV lead in MADIT-CRT trial (taken from [109])

at the latest electrically activated site (LEAS). In [140], pacing at the latest activated site yielded the best acute improvement in LV $dP/dt|_{max}$ in 31 of 32 patients. Afterwards, [75, 138] evaluated outcomes of a 6 months follow-up after lead placement at LEAS: in [75] the percentage of responders (defined such if they had a decrease $> 15\%$ in ESV) was higher for the group of patients with left lead implanted at the latest activated site.

However, choosing a-priori a region of LV pacing that is globally optimal is limitative and ineffective, as we deduce from studies mentioned above whose results were not always coherent with each other.

A reasonable point of view is to search for the best pacing site between randomly distributed locations on a patient-specific level [38], selecting the one corresponding to the best improvement in $dP/dt|_{max}$, index of greater hemodynamic outcome. This idea was followed in [41], where the maximum increase of $dP/dt|_{max}$ was obtained in the postero-lateral or lateral veins for most patients, and in the TARGET trial [67], the first study showing the benefit of a targeted approach to LV lead placement in CRT.

Concerning the relation between acute and chronic optimal site, it has been shown that in the majority of cases the best region for LV lead positioning remained the same also at 6 months follow-up [74, 125].

AV and VV delays programming

Another level of optimization is finding the best AVD and VVD (Section 1.2.1), while holding the pacing location fixed. This technique has shown improvements in the acute hemodynamic response because delay optimization has the ability to partially compensate for suboptimal LV lead placement [74]. Analogously to LV pacing site optimization strategy, delays programming is patient-specific. The effect on LV chronic remodeling is still

uncertain, because optimal values may change over time, consequently there is the need for regular reevaluation of such delays as the heart remodels. Although the biophysical model employed in [74] predicted that acutely determined optimal delays remained the same after 6 months at a fixed pacing site, with a diminished benefit.

For the purposes of this thesis, we will only focus on VV delay programming.

Sequential CRT, i. e. imposing VVD different from 0, was tested for the first time by RHYTHM II study [13] varying VVD between $\pm 20\ ms$, $\pm 40\ ms$ and $\pm 80\ ms$. Successive studies evaluated benefits on LV systolic function in a range of interventricular delays from $-20\ ms$ to $20\ ms$ [74, 110].

The hemodynamic quantities employed to quantify optimal delay are usually pressure values and rates of change of pressure dP/dt [92]. Another study [132] computed dyssynchrony indices to evaluate sensitivity of resynchronization to VVDs and showed by means of a computational model that VV delays producing better acute hemodynamic outcomes were longer than those required to minimize electrical dyssynchrony, but this was not clinically proved.

Pacing in proximity of scars

The presence of scar tissue in the region where the LV pacing lead is placed may be a cause of nonresponse to CRT. The slow conduction regions characterizing scar tissue may cause the electrical stimulation not to be translated in an effective mechanical activation [58] with consequent persistence of dyssynchrony post-CRT [11]. A possible solution could be the optimization of VV delay, imposing a longer LV pre-activation time interval [66]. On the other hand, analyzing cases of scar tissue located far from the pacing site, in [58] CRT outcomes did not differ much from the case without scar. However, a more recent study [37] found that presence of myocardial scar, either in the stimulated segment or in large regions of the myocardium, lead to lower response rate to CRT.

1.3. Computational Methods for Cardiac Electromechanics

There are three main physics governing heart functioning: the electrical propagation, the cardiac mechanics and the blood fluid dynamics in the chambers. Several mathematical and numerical strategies have been developed [100], consisting of systems of coupled differential equations describing each of the three phenomena.

Cardiac modeling can be more or less simplified depending on the number of physics that one decides to describe and on the order of the chosen models.

The most complete model ideally takes into account all the three physics described within a 3D framework, together with valve modelling that allows managing of the behavior of the system (i. e. the left ventricle) at the interface with the systemic and pulmonary circulation. However, this solution is still too expensive from the computational point of view: a higher accuracy in the mathematical description entails a larger number of equations to be solved and consequently a superior computational cost. The two most common combinations for the study of the cardiovascular system are electromechanical modelling, that is also the context of this thesis, or fluid–structure interaction models.

1.3.1.   Overview of the cardiac mathematical modeling

An exhaustive discussion of available cardiac mathematical models and their numerical resolution is reported in [98, 100]. The methods that will be employed in this thesis are explained in Chapter 2.

Here we will give a brief idea of the logic behind heart modelling.

The electrical activation of the heart is described at both microscopic and macroscopic scales, by means of ordinary differential equations (ODEs) for ionic currents generation and partial differential equations (PDEs) for the action potential propagation, respectively. The *bidomain equations* [47] or their simplified versions, *monodomain equation* or *Eikonal-diffusion equation* [46], give the macroscopic description of the trans-membrane potential travelling in a domain given by the union of myocardium, epicardium and endocardium. On the other hand, the so-called *ionic models*, like *FitzHugh–Nagumo* model [45] and *Bueno-Orovio* model [16], allow the closure of the electrophysiological (EP) model providing the ionic current travelling through the cell membrane.

Concerning the mechanical behavior of the cardiac muscle, a finite elasticity model must be used because of the large displacements encountered by cardiomyocytes. The *Piola-Kirchhoff* stress tensor is made of two contributions [84]: the *passive stress* needed to obtain a certain deformation of the passive myocardium and the *active stress* representing the force that is necessary to obtain the contraction induced by the electrical signal. Therefore, the last term needs information about electrical propagation that triggers active mechanical contraction (*excitation-contraction* coupling process), which is given by the trans-membrane potential or the calcium concentration computed in the electrical model. On the other hand, the electrical problem is influenced itself by the motion of the domain described through finite elasticity (*mechano-electrical feedback*), in particular, conductivities and ionic current depend on the deformation, as well as the spatial derivatives appearing in the bidomain/monodomain equations. This interdependence leads to the *coupled electromechanical* (EM) *problem* [48]. Lastly, ventricular fluid dynam-

ics models blood flow as a homogeneous, Newtonian, incompressible fluid by means of *Navier-Stokes equations* defined in a moving domain, usually in the *arbitrary Lagrangian-Eulerian* (ALE) formulation [25]. The displacement of the domain is computed by the finite elasticity equation and for this reason, the coupling of mechanical and fluid problems is addressed as *fluid-structure interaction* (FSI) problem.

When the coupled electromechanical problem is considered, the whole system of equations, including also fluid dynamics, becomes an *Electrical fluid-structure interaction* (EFSI) problem [98], see Figure 1.15.
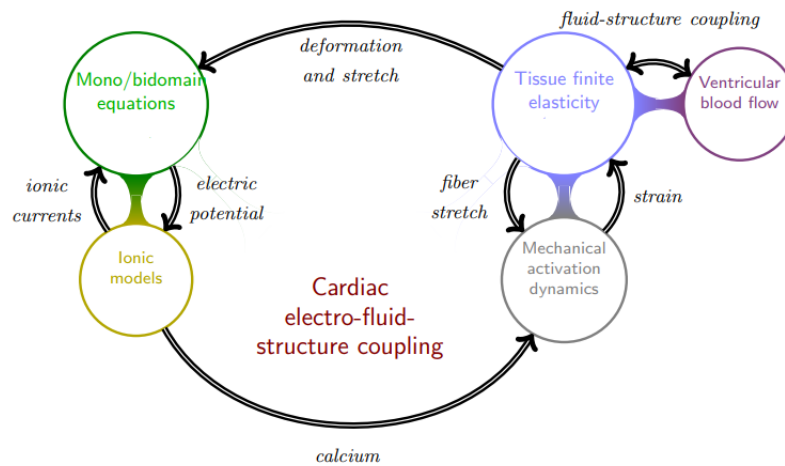

Figure 1.15: Structure of the EFSI problem (taken from [98])

In many applications, reduced-dimensional models are derived from the 3D formulations in order to reduce the complexity of the problem, also in terms of computational cost for their resolution [100]. For instance, in the EFSI problem, the fluid dynamics equations can be reduced to 1D or 0D if one needs to focus on the electromechanical behavior rather than on blood flow, as it happens in the present work. The coupling between 3D, 1D and 0D models is addressed as *geometric multiscale approach* and the idea is to use higher-dimensional models in those regions where a very detailed description is required, and lower-dimensional models in the remaining parts. An extensive review of the main multiscale methods was reported by Quarteroni A., Veneziani A., Vergara C. in [97]. In particular, 1D models are derived making simplifying assumption on the flow direction [91, 96] and they provide average quantities along that component. The reduced 0D models instead, called *lumped parameter models* [91], e. g. *Windkessel models* [134], are obtained integrating 1D models along the axial direction obtaining differential-algebraic equations (DAE) usually represented with an electrical analogy [99]: the flow rate plays

the role of the current, the pressure is the potential, the acceleration term is represented by an inductance, the viscosity term by a resistance, and the compliance term by a capacitance.

1.3.2.   State of the art of computational methods for electrome-chanics

The purpose of cardiac mathematical modelling is twofold. It aims first at achieving a better understanding of physical processes governing heart functioning, but the final goal is being able to provide a support to therapeutic planning in the clinical context. In the last decade a lot of models have already been applied [23] to both physiological and pathological scenarios.

The spatial domain of validity of a cardiac computational model, i. e. a whole heart or just one chamber, usually the LV, can be either an idealized geometry of cylindrical [6] or ellipsoidal shape [15] or a more realistic one derived from averaged real heart geometries (obtained by histological sections) [52, 64] or even an individual patient-specific heart model (obtained by means of MRI) [53, 61, 116, 117, 126].

In order to employ computational electromechanics models in clinical applications, clinical imaging techniques and modelling are increasingly linked [70], see Figure 1.16. Images are an instrument to validate a constructed model and to estimate model parameters by data assimilation finding the variables that best explain the observed data. Moreover, preliminary personalization of the model from clinical data and images information capturing patient anatomical variability is fundamental to run patient-specific simulations [61, 116].
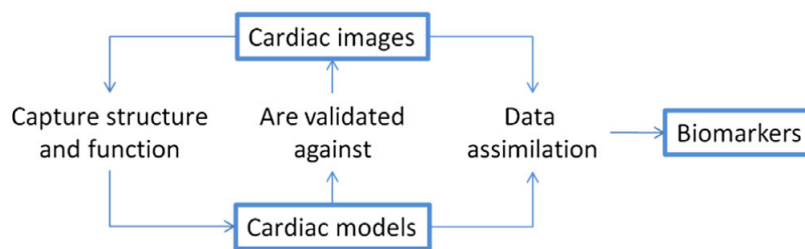

Figure 1.16: Scheme of interaction between imaging techniques and computational modelling (taken from [70])

Indeed, another level of personalization of the cardiac model, besides the use of patient-specific geometries, is the tuning of the parameters of the equations for the different compartments (electrophysiology, mechanics and hemodynamics) in order to match pa-

tient's clinical measurements, obtained for instance through MRI, CT, echocardiography, ECG or electroanatomical mapping, so that motion and electrophysiology patterns during a cardiac cycle can be reproduced with sufficient accuracy [79].

Personalized EP models estimate electrical conductivities or other quantities related to action potential duration [104] with the aim of reproducing patient's depolarization or repolarization times [61]. Mechanical models are calibrated in order to match correct values of volumes and pressures adjusting passive material stiffness [21, 137] and/or tissue contractility [21, 22], but also capacitances and resistances when they are coupled with a lumped model for circulation [21]. Once a computational model is assessed and personalized, the focus of several studies is on the simulation of pathological scenarios, i.e. arrhythmias, cadiomyopathies, myocardial infarction, heart failure.

For instance, EP models have been applied to *atrial fibrillation* (AF), *ventricular fibrillation* (VF), *ventricular tachycardia* (VT) in [82, 104, 127] respectively, using human atrial and ventricular reconstructed geometries. In [104] the patient was affected by dilated cardiomyopathy, myocardial LV scar, LBBB and consequent mechanical dyssynchrony.

An FSI framework was employed for the study of the congenital heart defect of *hypoplastic left heart syndrome* (HLHS) in reconstructed LVs [33], but also for a case of *dilated cardiomyopathy* (DCM) using an axisymmetrical half truncated prolate spheroid [24]. In this last study computational fluid dynamics (CFD) simulations were also performed with the *geometry-prescribed* technique, which imposes a wall motion as boundary datum instead of solving the solid problem.

In conclusion, we mention studies that are more of our interest, concerning application of EM methods coupled with lumped parameter models (usually Windkessel) for *myocardial infarction* (MI) in a reconstructed LV geometry [133] or biventricular geometry [3] and LBBB simulated in dog [62] or human [3] biventricular geometries.

1.3.3. Computational methods for cardiac reshynchronization therapy

Computational models for cardiac electromechanics can also be used as support to clinical therapies, such as device implantation techniques like cardiac reshynchronization therapy. As highlighted in previous paragraph, cardiac computational methods can be more or less complex and accurate when reproducing a particular scenario.

Concerning CRT simulations, studies during the last 20 years used mainly three types of mathematical models depending on the number of physical compartments described:

- Only electrophysiology (EP) model as in [105], usually with monodomain equations [56, 132] or computationally cheaper Eikonal equation [29, 73]. Commonly EP

equations are defined in a 3D framework, but in [56] also a 2D model was exploited.

- Electromechanics (EM) model, as in [63] where the LV pressure was derived just adding an input aortic impedance.

- EM model coupled to 0D lumped-parameter model for intra-cardiac fluid dynamics [30, 61] or systemic circulation [61, 62, 74, 108].

Secondly, the model setting may be either patient-specific or not, from the point of view of both anatomical and physical parameters. There are different levels of description that can be employed:

- General ventricular geometry (either ideal or realistic) and absent calibration of model parameters on the patient's data [56, 62, 63, 105].

- Patient-specific geometry, segmented from CT or MRI measures, but without physical parameters calibration [29].

- Fully patient-specific modeling [30, 61, 73, 74, 108, 132].

The segmented geometry might be either ventricular or bi-ventricular.

The complete model personalization is for sure the most accurate option in order to obtain a simulation which is the closest to the real scenario, but it is not always feasible because of lack of clinical invasive measures for the estimation of physical quantities.

The aforementioned studies represent a limited portion of the extensive research carried out in the last decade about numerical simulations of CRT for therapy planning. The main objectives being the choice of the best LV pacing site [30, 63, 105] or optimal AV/VV delays [105, 132] with evaluation of how variations of these settings affect clinical outcomes acutely [108] and perhaps chronically [74], but also investigation of the effects of myocardial scar tissue [29, 62] on LV function and comparison between epicardial versus endocardial pacing [29, 56, 73].

See Table 1.2 for a summary of the studies mentioned in this paragraph.

1.4.   Aim of the Thesis

The objective of this thesis is to provide an analysis of different cardiac resynchronization therapy virtual scenarios simulating the left ventricular electrical and mechanical behaviors using a patient-specific electromechanical computational model.

In particular, the EM simulations are performed exploiting the *Eikonal-Reaction-Mechanics* (ERM) model proposed in [115]. A *Reaction-Eikonal* (RE) model for electrophysiology computes activation times in LV myocardium and intracellular calcium ions concentra-

tion $[Ca^{2+}]_i$. The electrical problem is then coupled to the mechanics modelled with finite elasticity equations through the so called *excitation-contraction coupling process*. The active component of the stress tensor is retrieved from the physics-based active force model RDQ20-MF, proposed in [101]. Finally, the 0D hemodynamics for the circulatory system allows to retrieve the LV blood pressure p_{LV} for each phase of the cardiac cicle (Section 1.1.2), needed as boundary datum of the mechanics.

The numerical approximation of ERM model consists of a segregated method based on a loosely-coupled strategy. The time discretization of all equations exploits the *Backward Differentiation Formula* (BDF) scheme of order 1, while the spatial discretization of each subproblem is performed through Finite Element Method (FEM) of order 1 on hexahedral meshes (Q1). The numerical methods for the solution of such problem are implemented within the FEM C++ library `life`^x (https://lifex.gitlab.io/lifex).

1.4.1.   Calibration of electromechanical model

The ERM model is formulated in a fully patient-specific framework for 3 HF patients affected by LBBB who underwent CRT, whose clinical measurements and images come from Hospital of Santa Maria del Carmine in Rovereto (TN), Italy. The 3D LV computational domains were reconstructed from cineMRI images in [113], together with fibrosis distribution if present and coronary veins geometry.

The first purpose of the thesis is the calibration of electrical, mechanical and Winkdessel parameters (i. e. electrical conductivities, contractility and total peripheral resistance) in order to personalize the EM models on each patient. This can be done thanks to patients' clinical data of pressure, volumes and electrical timings and locations along epicardial veins and at the septum: a portion of data is used as input to the problem, while the remaining part has to be reproduced by the model for parameters adjustment.

This procedure is carried out with several electromechanical simulations of the heart at synus rhythm. Once the model is calibrated, the latest electrically activated segment (LEAS) is estimated from the Eikonal simulation as the point with higher activation time.

1.4.2.   Cardiac Resynchronization Therapy Simulation

The second step of the work consists in the simulation of the acute electromechanical behavior of the LV undergoing CRT. For each patient the parameters estimated during the first phase of the procedure are maintained the same, following the rationale that the LV does not remodel immediately after device implantation.

In order to reproduce a CRT scenario, input data to the Eikonal model are changed,

imposing the coordinates and the initial timings of the RV and LV leads locations on the epicardium.

The final goal of the thesis is the optimization of CRT implantation procedure in each of the three patients by comparison of several CRT virtual scenarios simulated with different device settings. First, the LV pacing site is set to be at the computed LEAS, secondly, several points distributed along the reconstructed epicardial veins are selected as possible locations for the LV lead. Conversely, the RV lead is always kept fixed. Electromechanical simulations are performed for each possible location in the case of simultaneous right and left stimulation (VV delay set to 0). Afterwards, for the configurations giving the best hemodynamics outcomes, different VV delays, positive and negative, are tested, using a similar procedure to [74]. All combinations of pacing site and VV delay are compared based on the outputs of EM simulations that allow to compute biomarkers evaluating acute hemodynamic outcomes. Finally, the best settings are selected for each patient.

Work	Goal	Patient-specific geometry	EP	Mechanics	Lumped model	Calibration
Kerckhoffs et al., 2003 [63]	Analysis of pacing site	✗	✓	✓	✗	✗
Reumann et al., 2007 [105]	Optimization of VVD and pacing site	✗	✓	✗	✗	✗
Kerckhoffs et al., 2009 [62]	BiV pacing and scar impact	✗	✓	✓	✓	✗
Sermesant et al., 2011 [108]	Predict acute hemodynamic outcomes	✓	✓	✓	✓	✓
Hyde et al., 2015 [56]	Endocardial/Epicardial pacing comparison	✗	✓	✗	✗	✗
Kayvanpour et al., 2015 [61]	Analysis of the predictive power of the model	✓	✓	✓	✓	✓
Crozier et al., 2016 [30]	Patients selection, optimization of pacing site	✓	✓	✓	✓	✓
Villongco et al., 2016 [132]	Dyssynchrony evaluation, VVD optimization	✓	✓	✗	✗	✓
Lee et al., 2017 [74]	Pacing site and VVD optimization for chronic CRT	✓	✓	✓	✓	✓
Costa et al., 2020 [29]	Analysis of endocardial pacing near scar	✓	✓	✗	✗	✗

Table 1.2: State of the art of EM methods for CRT

2 | Mathematical and Numerical Methods

In this Chapter the Eikonal-Reaction-Mechanics (ERM) model mentioned in Section 1.4 is detailed. This model was proposed in [115] with the aim of reducing the computational cost with respect to already existing cardiac EM models, thanks to an efficient off-line procedure for the solution of the Reaction equation.

In the following discussion, the mathematical formulation will be first addressed in Section 2.1, presenting the equations for each physical compartment and the subsequent global coupled EM problem. Then, in Section 2.2 the numerical approximation of the ERM problem is reported, including the Finite Element Method (FEM) for space discretization and the time discretization schemes. The Chapter is concluded in Section 2.3 giving a brief idea of the methods used to obtain geometric information needed to solve the ERM model, such as the generation of a 3D finite element hexahedral mesh, the procedure used to include the fibrosis distribution in the LV by means of a preprocessing strategy and the rule-based algorithm for cardiac fibers orientation, both implemented in the FEM `C++` library `lifeˣ` (`https://lifex.gitlab.io/lifex`).

2.1. Mathematical model

The equations for electrophysiology, mechanics and circulation are discussed in the following paragraphs. As mentioned in Section 1.3, the electromechanical coupling entails a mutual interaction between the two compartments, having on one hand the *excitation-contraction* coupling process in which calcium ions concentration is given in input to the mechanical problem. On the other hand, the *mechano-electrical feedbacks* should be considered since they take into account the heart wall deformation and allow for the solution of time-dependent EP equations in a moving domain. However, in the ERM model the simplified steady Eikonal equation is employed to model electrical propagation, preventing the inclusion of those feedbacks. The structure that we are going to explain can be visualized in Figure 2.1.
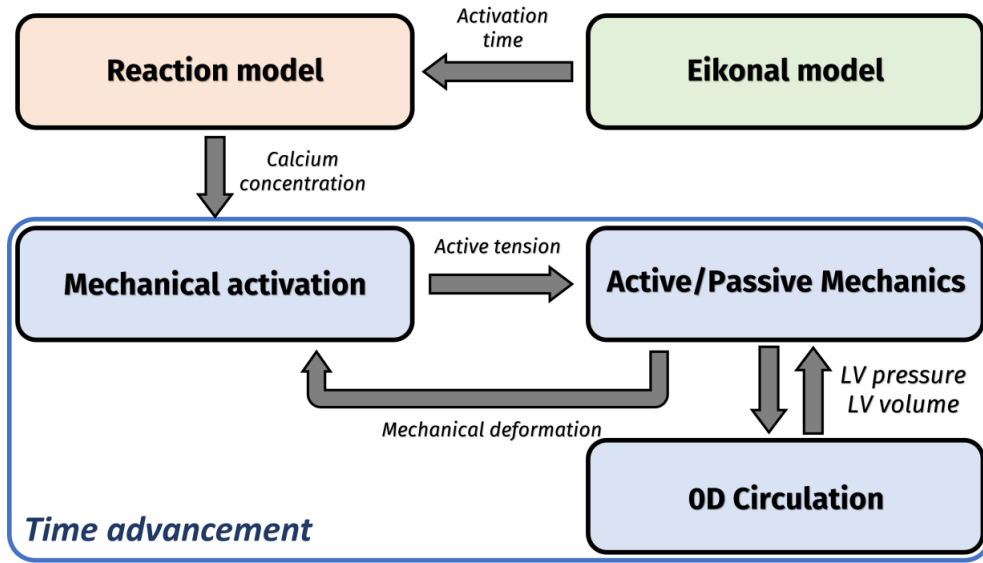
Figure 2.1: General structure of the ERM model (taken from [115])

The ERM problem is solved in a 3D LV domain denoted by $\Omega \subset \mathbb{R}^3$ (Figure 2.2), whose surfaces are Γ_{base}, Γ_{endo} and Γ_{epi}, representing the base, the endocardium and the epicardium interfaces, respectively.
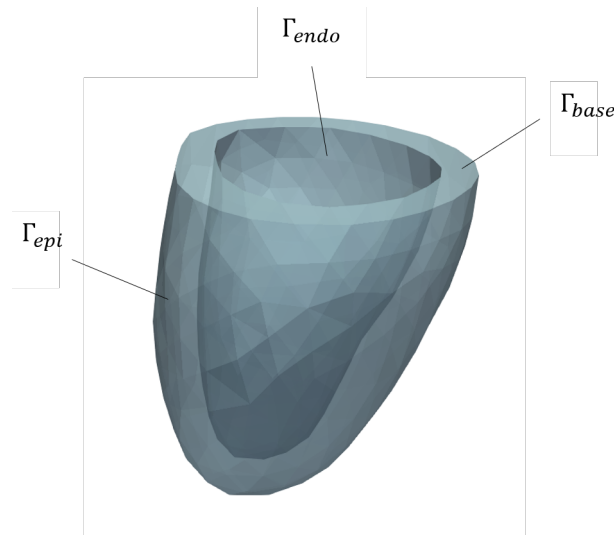

Figure 2.2: Domain Ω of a realistic LV geometry (Zygote 3D Human Heart Model [1])

2.1.1. Electrophysiology

The electrical behavior of the LV is modelled by means of the efficient *Reaction-Eikonal* (RE) equation [86], which allows a reduction of the computational cost of classic *bidomain* or *monodomain* equations.

Eikonal-Diffusion equation

The *Eikonal-diffusion* equation [28, 100] describes the evolution of depolarization times in the myocardium, without modelling the transmembrane potential. The mathematical formulation is addressed below.

Let $\psi(x) : \Omega \rightarrow \mathbb{R}^3$ be the unknown activation time, solution of the Eikonal-diffusion equation:

$$
\begin{cases}
c_0\sqrt{\nabla\psi \cdot \dfrac{1}{\chi C_m}\mathbf{D}\nabla\psi} - \varepsilon\nabla \cdot \left(\dfrac{1}{\chi C_m}\mathbf{D}\nabla\psi\right) = 1 & \text{in } \Omega, & (2.1\text{a}) \\[2mm]
\left(\dfrac{1}{\chi C_m}\mathbf{D}\nabla\psi\right) \cdot \boldsymbol{n} = 0 & \text{on } \partial\Omega \setminus S_a, & (2.1\text{b}) \\[2mm]
\psi = \psi_a & \text{on } S_a & (2.1\text{c})
\end{cases}
$$

where $\mathbf{D}$ is the conductivity tensor defined as

$$
\mathbf{D} = z\sigma_s\mathbf{1} + z(\sigma_f - \sigma_s)\boldsymbol{f} \otimes \boldsymbol{f} + z(\sigma_n - \sigma_s)\boldsymbol{n} \otimes \boldsymbol{n} \tag{2.2}
$$

with σ_f, σ_s and σ_n being the conductivities along the fibers $\boldsymbol{f}$, the sheets $\boldsymbol{s}$ and the normal $\boldsymbol{n}$ directions, respectively, and $z \in [0,1]$ is the degree of fibrosis that goes from scar tissue for $z = 0$ to healthy for $z = 1$. Then, χ is the surface to volume ratio, C_m is the transmembrane capacitance, c_0 is a surrogate of the velocity of the depolarization planar wave along the fibers direction and ε is a dimensionless parameter linked to the influence of wavefront curvature on wave velocity [63]. Concerning boundary conditions (BC) in (2.1c), the portion of the boundary S_a surrogates the Purkinje network [88, 129, 130] whose anatomy is not included in the present work. On this region Dirichlet BC are imposed and the values ψ_a are data given as input to the equation.

Problem (2.1) will be compactly written as

$$
\psi = \mathcal{E}(\psi_a). \tag{2.3}
$$

It is important to observe that, besides the LV domain Ω, other necessary geometric data (see Section 2.3) has to be included for the solution of the Eikonal problem (2.1), such as the orientation of cardiac fibers on the whole 3D volume, so that directions $\boldsymbol{f}, \boldsymbol{s}$ and $\boldsymbol{n}$ can be retrieved, and the distribution of fibrotic tissue in the myocardium to set a value for z. Such information allows to compute the conductivity tensor $\mathbf{D}$. Standard imaging techniques are not able to capture the fibers geometry, hence, fibers can not be

reconstructed from real data but a rule-based algorithm, which is briefly addressed in Section 2.3.2, is employed in the present work. On the other hand, the localization of fibrosis can be derived from bullseye plots (see Section 1.1.4) obtained by means of MRI measurements.

Reaction equation

The Eikonal-diffusion equation (2.1) is coupled to a simplified version of the monodomain model in order to retrieve the calcium ions concentration $[Ca^{2+}]_i$ that will be needed to formulate the active force generation model addressed in Section 2.1.2.

First of all, the complete *monodomain model* defined in $\Omega \times (0, T)$, with T final time, reads:

$$\begin{cases} J\chi \left[C_m \frac{\partial u}{\partial t} + I_{\text{ion}}(u, \boldsymbol{w}, \boldsymbol{z}) \right] - \nabla \cdot (J\mathbf{F}^{-1}\boldsymbol{D}\mathbf{F}^{-T}\nabla u) = JI_{\text{app}}(\boldsymbol{x}, t) & \text{in } \Omega \times (0, T), & (2.4\text{a}) \\ \frac{d\boldsymbol{w}}{dt} = \boldsymbol{h}(u, \boldsymbol{w}) & \text{in } \Omega \times (0, T), & (2.4\text{b}) \\ \frac{d\boldsymbol{z}}{dt} = \boldsymbol{g}(u, \boldsymbol{w}, \boldsymbol{z}) & \text{in } \Omega \times (0, T), & (2.4\text{c}) \\ (J\mathbf{F}^{-1}\boldsymbol{D}\mathbf{F}^{-T}\nabla u) \cdot \boldsymbol{N} = 0 & \text{on } \partial\Omega \times (0, T) & (2.4\text{d}) \end{cases}$$

With $u : \Omega \times (0, T) \to \mathbb{R}$ transmembrane potential, $I_{\text{app}}(\boldsymbol{x}, t)$ an applied external current, $\mathbf{F}$ the deformation gradient and J its Jacobian (see Section 2.1.2) and $I_{\text{ion}}(u, \boldsymbol{w}, \boldsymbol{z})$ ionic current derived from a suitable ionic model given by equations (2.4b) and (2.4c), whose specific functions are denoted by $\boldsymbol{h} \in \mathbb{R}^r$ and $\boldsymbol{g} \in \mathbb{R}^s$, $\boldsymbol{w} : \Omega \times (0, T) \to \mathbb{R}^r$ are the gating variables and $\boldsymbol{z} : \Omega \times (0, T) \to \mathbb{R}^s$ are the ionic concentrations. In particular, in the ERM model proposed in [113], the 18-variables ten Tusscher-Panfilov model [123] was chosen as ionic model to describe equations (2.4b) and (2.4c).

The model employed in this thesis uses the following simplified monodomain equation [86], in which the diffusion term is neglected:

$$\begin{cases} \chi \left[C_m \frac{\partial u}{\partial t} + I_{\text{ion}}(u, \boldsymbol{w}, \boldsymbol{z}) \right] = I_{\text{app}}(t - \psi(x)) & \text{in } \Omega \times (0, T_{HB}), \\ \frac{d\boldsymbol{w}}{dt} = \boldsymbol{h}(u, \boldsymbol{w}) & \text{in } \Omega \times (0, T_{HB}), \\ \frac{d\boldsymbol{z}}{dt} = \boldsymbol{g}(u, \boldsymbol{w}, \boldsymbol{z}) & \text{in } \Omega \times (0, T_{HB}) \end{cases} \quad (2.5)$$

The time interval $(0, T_{HB})$ is the duration of a heartbeat, hence, periodic BC are imposed in every $\boldsymbol{x} \in \Omega$: $u(\boldsymbol{x}, T_{HB}) = u(\boldsymbol{x}, 0)$, $\boldsymbol{w}(\boldsymbol{x}, T_{HB}) = \boldsymbol{w}(\boldsymbol{x}, 0)$ and $\boldsymbol{z}(\boldsymbol{x}, T_{HB}) = \boldsymbol{z}(\boldsymbol{x}, 0)$. The space-dependent function $\psi(\boldsymbol{x})$ is the solution of Eikonal problem (2.1) and the applied

current I_{app} is defined as

$$I_{\text{app}}(t) = \begin{cases} \bar{I}_{\text{app}} & \text{if } 0 \leq \text{mod}(t, T_{HB}) < \delta_{\text{stim}}, \\ 0 & \text{otherwise} \end{cases} \tag{2.6}$$

With prescribed values of $\bar{I}_{\text{app}}$ and δ_{stim} and function $\text{mod}(\cdot, \cdot)$ indicating the remainder after division. Evaluating $I_{\text{app}}(t - \psi(\boldsymbol{x}))$ means that an applied current is present in each point $\boldsymbol{x}$ of the domain in a neighbourhood of its activation time $\psi(\boldsymbol{x})$. This is an approximation of the diffusion process that would be neglected otherwise.

An efficient strategy is employed for the solution of the reaction equations, consisting in the reduction of the problem to a system of independent ODEs, one for each point of the domain. For every $\boldsymbol{x} \in \Omega$ we define the solution to the Reaction problem (2.5) as a translation of a 0D function depending on time only by a quantity equal to the activation time $\psi(\boldsymbol{x})$.

$$\begin{aligned} u(\boldsymbol{x}, t) &= u^{0D}(t - \psi((x))), \\ \boldsymbol{w}(\boldsymbol{x}, t) &= \boldsymbol{w}^{0D}(t - \psi((x))), \\ \boldsymbol{z}(\boldsymbol{x}, t) &= \boldsymbol{z}^{0D}(t - \psi((x))). \end{aligned} \tag{2.7}$$

The 0D functions are solution to the reduced problem:

$$\begin{cases} \chi \left[C_m \dfrac{du^{0D}}{dt} + I_{\text{ion}}(u^{0D}, \boldsymbol{w}^{0D}, \boldsymbol{z}^{0D}) \right] = I_{\text{app}}(t) & \text{in } (0, T), & (2.8a) \\[2mm] \dfrac{d\boldsymbol{w}^{0D}}{dt} = \boldsymbol{h}(u^{0D}, \boldsymbol{w}^{0D}) & \text{in } (0, T), & (2.8b) \\[2mm] \dfrac{d\boldsymbol{z}^{0D}}{dt} = \boldsymbol{g}(u^{0D}, \boldsymbol{w}^{0D}, \boldsymbol{z}^{0D}) & \text{in } (0, T) & (2.8c) \end{cases}$$

whose BC become $u^{0D}(T_{HB}) = u^{0D}(0)$, $\boldsymbol{w}^{0D}(T_{HB}) = \boldsymbol{w}^{0D}(0)$ and $\boldsymbol{z}^{0D}(T_{HB}) = \boldsymbol{z}^{0D}(0)$ and the 0D solutions are periodically extended outside of $[0, T_{HB}]$.

The advantage of the reduced problem (2.8) is that spatial dependence can be disregarded, and the system of ODEs can be solved off-line.

In conclusion, once the solution $(u^{0D}, \boldsymbol{w}^{0D}, \boldsymbol{z}^{0D})$ is obtained, a component of $\boldsymbol{z}^{0D}$ will be the 0D calcium concentration $[Ca^{2+}]_i^{0D}$. Accordingly:

$$[Ca^{2+}]_i(\boldsymbol{x}, t) = [Ca^{2+}]_i^{0D}(t - \psi(\boldsymbol{x})). \tag{2.9}$$

In order to indicate equations (2.7), (2.8) and (2.9) compactly, we will write

$$[Ca^{2+}]_i = \mathcal{R}(\psi). \tag{2.10}$$

2.1.2.   Mechanics

The EP problem given by (2.3) and (2.10) is coupled to the equations of finite elasticity for the mechanical description in which the passive component of *Piola-Kirkhhoff* stress tensor is obtained by means of *Guccione constitutive law*, while the active component is retrieved from the physics-based active force model *RDQ20-MF*, proposed in [101].

Mechanical Activation model

In this paragraph we detail the formulation of the *RDQ20-MF* [101] model for the active component of the stress tensor, which uses a biophysical representation of proteins in sarcomeres (the smallest functional units of striated muscle tissue). It consists of a system of ODEs taking as input datum the calcium concentration $[Ca^{2+}]_i$ given by problem (2.10). Let $s : \Omega \times (0, T) \to \mathbb{R}^{20}$ be the 20 state variables of the model describing the chemical and mechanical states of proteins that take part to sarcomere function, like *actine* and *myosin* for contraction. Such variables satisfy the following equation:

$$\begin{cases} \dfrac{ds}{dt} = K\left(s, [Ca^{2+}]_i, SL, \dfrac{dSL}{dt}\right) & \text{in } \Omega \times (0, T), \\ s(0) = s_0 & \text{in } \Omega \times \{t = 0\} \end{cases} \tag{2.11}$$

Besides calcium concentration, another input to the model is the sarcomere length SL, determined starting from the length at rest SL_0 and applying the local stretch in the fibers direction evaluated with the fourth invariant $\mathcal{I}_{4f} = \mathbf{F}f \cdot \mathbf{F}f$:

$$SL = SL_0\sqrt{\mathcal{I}_{4f}}.$$

The deformation gradient $\mathbf{F}$ is obtained from the tissue displacement d, solution of the equations of finite elasticity (2.14) addressed in the next paragraph.
Then, the active tension needed to obtain the active component of the stress is computed by means of a non-linear function G [101] depending on s and SL:

$$T_a = G(s, SL). \tag{2.12}$$

A compact form of (2.11) and (2.12) is written as

$$T_a = \mathcal{F}([Ca^{2+}]_i, d). \tag{2.13}$$

Finite Elasticity equation

In conclusion, the equations of finite elasticity [100] representing the momentum conservation provide the evolution of the tissue displacement $\boldsymbol{d} : \Omega \times (0, T) \to \mathbb{R}^3$:

$$
\begin{cases}
\rho \dfrac{\partial^2 \boldsymbol{d}}{\partial t^2} - \nabla \cdot \mathbf{P}(\boldsymbol{d}, T_a) = 0 & \text{in } \Omega \times (0, T), & \text{(2.14a)} \\[2mm]
\mathbf{P}(\boldsymbol{d}, T_a)\boldsymbol{n} + \mathbf{K}^{\text{epi}}\boldsymbol{d} + \mathbf{C}^{\text{epi}} \dfrac{\partial \boldsymbol{d}}{\partial t} = 0 & \text{on } \Gamma_{\text{epi}} \times (0, T), & \text{(2.14b)} \\[2mm]
\mathbf{P}(\boldsymbol{d}, T_a)\boldsymbol{n} = -p_{LV}(t) J \mathbf{F}^{-T} \boldsymbol{n} & \text{on } \Gamma_{\text{endo}} \times (0, T), & \text{(2.14c)} \\[2mm]
\mathbf{P}(\boldsymbol{d}, T_a)\boldsymbol{n} = p_{LV}(t) |J \mathbf{F}^{-T} \boldsymbol{n}| \boldsymbol{v}^{\text{base}}(t) & \text{on } \Gamma_{\text{base}} \times (0, T), & \text{(2.14d)} \\[2mm]
\boldsymbol{d} = \boldsymbol{d}_0 & \text{in } \Omega \times \{t = 0\}, & \text{(2.14e)} \\[2mm]
\dfrac{\partial \boldsymbol{d}}{\partial t} = \dot{\boldsymbol{d}}_0 & \text{in } \Omega \times \{t = 0\} & \text{(2.14f)}
\end{cases}
$$

The Piola-Kirkhhoff stress tensor, denoted by $\mathbf{P}$, is given by the sum of the passive and active components of the mechanics [84]:

$$
\mathbf{P}(\boldsymbol{d}, T_a) = \frac{\partial \mathcal{W}(\mathbf{F})}{\partial \mathbf{F}} + T_a \frac{\mathbf{F}\boldsymbol{f} \otimes \boldsymbol{f}}{\sqrt{\mathcal{I}_{4f}}} \tag{2.15}
$$

where $\mathbf{F} = \mathbf{I} + \nabla \boldsymbol{d}$ is the deformation gradient.

The first term in (2.15) is the passive part which is modelled with Guccione constitutive law for the strain energy function $\mathcal{W}$:

$$
\mathcal{W}(\mathbf{F}) = \frac{C}{2}(e^Q - 1)
$$

where $C = \mathbf{F}^T \mathbf{F}$ is the right Cauchy-Green deformation tensor and Q is defined in [51]. The second term in (2.15) represents the active mechanics where the quantity T_a is provided by problem (2.13) and we have assumed that contraction occurs only along the fibers [100, 101].

Focusing on BC, (2.14b) represents the interaction of the LV domain Ω with the external pericardium, where tensors $\mathbf{K}^{\text{epi}}$ and $\mathbf{C}^{\text{epi}}$ are defined as:

$$
\begin{aligned}
\mathbf{K}^{\text{epi}} &= K_{\perp}^{\text{epi}}(\boldsymbol{n} \otimes \boldsymbol{n}) + K_{\parallel}^{\text{epi}}(\mathbf{I} - \boldsymbol{n} \otimes \boldsymbol{n}), \\
\mathbf{C}^{\text{epi}} &= C_{\perp}^{\text{epi}}(\boldsymbol{n} \otimes \boldsymbol{n}) + C_{\parallel}^{\text{epi}}(\mathbf{I} - \boldsymbol{n} \otimes \boldsymbol{n}),
\end{aligned} \tag{2.16}
$$

$K_{\perp}^{\text{epi}}, K_{\parallel}^{\text{epi}}, C_{\perp}^{\text{epi}}$ and $C_{\parallel}^{\text{epi}}$ are positive values for stiffness and viscosity of the pericardium in normal and tangential directions [93].

Equation (2.14c) encloses the BC at the endocardium, describing the interaction with blood flow in the chamber, indeed $p_{LV}(t)$ is the LV pressure computed by the 0D hemodynamic model, explained in Section 2.1.3.

On the other hand, equation (2.14d) represents the BC at the base of the LV, where LV pressure is still given by the 0D model, but here the presence of the additional term

$$\boldsymbol{v}^{\text{base}}(t) = \frac{\int_{\Gamma_{\text{endo}}} J\mathbf{F}^{-T}\boldsymbol{n} \ d\Gamma}{\int_{\Gamma_{\text{base}}} \|J\mathbf{F}^{-T}\boldsymbol{n}\| \ d\Gamma} \tag{2.17}$$

introduces an energy-consistent BC [102].

In the end, the finite elasticity problem (2.14) will be indicated with

$$\boldsymbol{d} = \mathcal{M}(T_a, p_{LV}, \boldsymbol{d}), \tag{2.18}$$

where the dependence on $\boldsymbol{d}$ itself implies the presence of non-linearity in the equation.

It is important to observe that the equations (2.14) should be written in a stress-free configuration of Ω, without the action of blood pressure, which is instead present when segmenting a LV geometry from clinical images. The reason is that the Piola-Kirkhhoff tensor (2.15) has to be evaluated at the right points.

2.1.3.   Hemodynamics

The blood circulation modelling is needed for the boundary conditions at the endocardium (2.14c) and at the base (2.14d) of the mechanics problem (2.14).

The hemodynamics is modelled here with a 0D reduced-order model proposed by Regazzoni F., Dedè L., Quarteroni A. in [102], which provides the LV pressure p_{LV}^{0D} dividing the cardiac cycle in the four phases explained in Section 1.1.2.

Moreover, since the LV volume is needed, it can be computed from the solution of the 3D mechanics problem with the formula [103]:

$$V_{LV}^{3D}(t) = \int_{\Gamma_{\text{endo}}} J(t)((\boldsymbol{h} \otimes \boldsymbol{h})(\boldsymbol{x} + \boldsymbol{d}(t) - \boldsymbol{b})) \cdot \mathbf{F}^{-T}(t)\boldsymbol{n} \ d\Gamma \tag{2.19}$$

where $\boldsymbol{h}$ is a vector belonging to the plane of the LV base and $\boldsymbol{b}$ is the vector of coordinates of an arbitrary point in the LV.

1. **Isovolumetric contraction**: problem (2.14) is solved under the constraint $V_{LV}^{3D} = EDV$ where the end diastolic volume EDV is considered to be an available datum. Here p_{LV}^{0D} is calculated as the Lagrange multiplier of the constraint and it assumes an

increasing behavior until time t_{AVO} when it reaches the value of aortic valve opening pressure $\bar{p}_{\mathrm{AVO}}^{0D}$, which is a given datum.

2. **Ejection**: At time t_{AVO} the aortic valve opens letting blood exit the chamber. The pressure evolution is modelled here with a two-element Windkessel model [134]:

$$C\frac{dp_{LV}^{0D}}{dt} + \frac{1}{R}p_{LV}^{0D} = \frac{dV_{LV}^{3D}}{dt} \qquad t \in (t_{\mathrm{AVO}}, t_{\mathrm{AVC}}) \tag{2.20}$$

where R represents the total peripheral resistance and C the total arterial compliance. At time instant t_{AVC} the aortic valve closes, when $\frac{dV_{LV}^{3D}}{dt}$ changes sign. And $p_{LV}^{0D}(t_{\mathrm{AVC}}) = \bar{p}_{\mathrm{AVC}}^{0D}$.

3. **Isovolumetric relaxation**: problem (2.14) is solved under the constraint $V_{LV}^{3D} = ESV$ where the end sistolic volume $ESV = V_{LV}^{3D}(t_{\mathrm{AVC}})$. Here p_{LV}^{0D} decreases until it reaches the prescribed value of mitral valve opening $\bar{p}_{\mathrm{MVO}}^{0D}$.

4. **Filling**: At the opening of the mital valve, p_{LV}^{0D} evolves linearly increasing until the prescribed value of mitral valve closing denoted by $\bar{p}_{\mathrm{ED}}^{0D}$, representing the end diastolic pressure EDP.

Equation (2.20) imposes the flow rate continuity, while boundary conditions (2.14c) and (2.14d) of the finite elasticity problem (2.14) impose the pressure continuity.

The hemodynamic problem, including also (2.19), will be compactly denoted with

$$p_{LV} = \mathcal{C}(\boldsymbol{d}). \tag{2.21}$$

2.1.4. Coupled ERM problem

The full Eikonal-Reaction-Mechanics problem can be written in a compact form higliting the coupling between problems (2.3), (2.10), (2.13), (2.18), (2.21):

$$\begin{cases} \text{Steady Eikonal} & \psi = \mathcal{E}(\psi_a), \\ \text{Reaction} & [Ca^{2+}]_i = \mathcal{R}(\psi), \\ \text{Mechanical Activation} & T_a = \mathcal{F}([Ca^{2+}]_i, \boldsymbol{d}), \\ \text{Finite Elasticity} & \boldsymbol{d} = \mathcal{M}(T_a, p_{LV}, \boldsymbol{d}), \\ \text{0D hemodynamics} & p_{LV} = \mathcal{C}(\boldsymbol{d}). \end{cases} \tag{2.22}$$

Substituting all the chained equations of (2.22) in (2.18) we retrieve a fixed-point problem for the unknown of myocardial displacement $\boldsymbol{d}$:

$$\boldsymbol{d} = \mathcal{M}(\mathcal{F}(\mathcal{R}(\mathcal{E}(\psi_a)), \boldsymbol{d}), \mathcal{C}(\boldsymbol{d}), \boldsymbol{d}).$$

2.2.   Numerical Formulation of the ERM model

The numerical approximation of the ERM model (2.22) uses a segregated method based on a loosely-coupled strategy for the two couplings between active force generation and mechanics, and mechanics/hemodynamics. The EP problem is already segregated by construction of the mathematical model.

The equations are discretized in time with the Backward Differentiation Formula of order 1 (BDF1) and in space using the Finite Element Method (FEM) of order 1 on hexahedral meshes (Q1). The linear systems arising from the spatial discretization of each subproblem are solved with the GMRES method preconditioned with the AMG preconditioner. For the solution of non-linear problems, Newton algorithm is employed. Such numerical methods are all implemented within the high-performance `C++` library `life`^x mainly focused on cardiac applications.

2.2.1.   Discretization of the Eikonal-diffusion problem

The numerical approximation of the steady Eikonal-diffusion problem (2.1) is carried out introducing a *pseudo-time* variable τ and adding to equation (2.1a) the temporal derivative of the unknown ψ with respect to τ, so that the equation becomes of parabolic type:

$$\frac{\partial \psi}{\partial \tau} + c_0 \sqrt{\nabla \psi \cdot \frac{1}{\chi C_m} \mathbf{D} \nabla \psi} - \varepsilon \nabla \cdot \left(\frac{1}{\chi C_m} \mathbf{D} \nabla \psi \right) = 1 \qquad \text{in } \Omega \times (0, \tilde{T}] \qquad (2.23)$$

The idea is to solve equation (2.23) and look for a steady-state solution of such problem [47], that is reached at $\tau = \tilde{T}$.

Weak formulation

The weak formulation of problem (2.23) is written starting from the introduction of the Sobolev space

$$W = H^1(\Omega)$$

where we look for a weak solution of the problem (2.24). The weak formulation reads:
Find $\psi(\boldsymbol{x}) \in W$, with $\psi(\boldsymbol{x}) = \psi_a(\boldsymbol{x})$ on S_a, such that:

$$\int_\Omega \frac{\partial \psi}{\partial \tau} \phi \, d\Omega + \int_\Omega c_0 \sqrt{\nabla\psi \cdot \frac{1}{\chi C_m} \mathbf{D}\nabla\psi} \phi \, d\Omega + \int_\Omega \varepsilon \frac{1}{\chi C_m} \mathbf{D}\nabla\psi \cdot \nabla\phi \, d\Omega =$$
$$\int_\Omega \phi \, d\Omega + \int_{S_a} \psi_a \phi \, dS_a \quad (2.24)$$

for every test function $\phi \in W$.

Finite Element formulation

Going to the space discretization, a triangulation $\mathcal{T}_h$ of the LV domain Ω into hexahedra K is introduced. Each element K has diameter h_K, and the characteristic mesh size is defined as $h = max_{K \in \mathcal{T}_h} h_K$. The domain Ω is then written as the union of all the elements of the triangulation:

$$\Omega = \bigcup_{K \in \mathcal{T}_h} K.$$

We define the finite dimensional space $W_h \subset W$ and retrieve the Galerkin formulation from problem (2.24):
Find $\psi_h \in W_h$ such that

$$\int_\Omega \frac{\partial \psi_h}{\partial \tau} \phi_h \, d\Omega + \int_\Omega c_0 \sqrt{\nabla\psi_h \cdot \frac{1}{\chi C_m} \mathbf{D}\nabla\psi_h} \phi_h \, d\Omega + \int_\Omega \varepsilon \frac{1}{\chi C_m} \mathbf{D}\nabla\psi_h \cdot \nabla\phi_h =$$
$$\int_\Omega \phi_h \, d\Omega + \int_{S_a} \psi_a \phi_h \, dS_a \quad (2.25)$$

for every test function $\phi_h \in W_h$.
For the particular case of FEM of order 1 on a hexahedral mesh, the finite dimensional space W_h is taken as the space of globally continuous function in $\bar{\Omega}$ that are polinomials of order 1 on each hexahedron K:

$$X_h^1 = \{f_h \in C^0(\bar{\Omega}) : f_h|_K \in \mathbb{Q}^1, \forall K \in \mathcal{T}_h\}.$$

In order to write the Finite Element formulation, denote by $N_\psi = \dim(X_h^1)$ the dimension of the FE space and let $\{\varphi_i\}_{i=1}^{N_\psi}$ be a basis of X_h^1. Hence, the Galerkin solution can be written as a linear combination of this basis:

$$\psi_h(\boldsymbol{x}, \tau) = \sum_{i=1}^{N_\psi} \psi_i(\tau)\varphi_i(\boldsymbol{x}) + \sum_{j=N_\psi+1}^{N_\psi+N_\psi^a} \psi_{a,j}(\tau)\varphi_j(\boldsymbol{x}) \quad (2.26)$$

where N_ψ^a is the number of degrees of freedom of the Dirichlet boundary $S_a \subset \partial\Omega$ in which BC (2.1c) is imposed. Then, the test function in the Galerkin problem (2.25) is set to be $\phi_h = \varphi_i$. Substituting also expression (2.26) in (2.25), the following ODE is obtained:

$$
\begin{cases}
M\dfrac{d\boldsymbol{\psi}_h}{d\tau} + A\boldsymbol{\psi}_h + \boldsymbol{m}(\psi_h) = \boldsymbol{f}(\tau) & \tau \in (0, \tilde{T}), \\
\boldsymbol{\psi}_h(0) = \boldsymbol{\psi}_0
\end{cases}
\tag{2.27}
$$

whose solution is the vector of coefficients of the linear combination of basis functions (2.26):

$$
\boldsymbol{\psi}_h = [\psi_1, ..., \psi_{N_\psi}].
$$

The matrices and vectors appearing in (2.27) have the following expressions:

$$
(M)_{ij} = \int_\Omega \varphi_j \varphi_i \, d\Omega,
\tag{2.28}
$$

$$
(A)_{ij} = \varepsilon \int_\Omega \mathbf{D}\nabla\varphi_j \cdot \nabla\varphi_i \, d\Omega,
\tag{2.29}
$$

$$
(\boldsymbol{m}(\psi_h))_j = c_0 \int_\Omega \sqrt{\nabla\psi_h \cdot \frac{1}{\chi C_m}\mathbf{D}\nabla\psi_h}\,\varphi_j \, d\Omega,
\tag{2.30}
$$

$$
(\boldsymbol{f}(\tau))_j = \int_\Omega \varphi_j \, d\Omega + \int_{S_a} \psi_a \varphi_j \, dS_a.
\tag{2.31}
$$

Time Discretization

Finally, the system of ODEs (2.27) is discretized in time. A partition of N subintervals of length $\Delta\tau$ of the fictitious time interval $(0, \tilde{T})$ is introduced: (τ^n, τ^{n+1}) with $n = 0, ..., N-1$, so that $\tau^{n+1} = (n+1)\Delta\tau$. We approximate the Galerkin solution at pseudo-time step τ^{n+1} as $\boldsymbol{\psi}_h(\tau^{n+1}) \approx \boldsymbol{\psi}_h^{n+1}$ and set $\boldsymbol{\psi}_h^0 = \boldsymbol{\psi}_0$.

A fully implicit backward Euler scheme (BDF1) is employed for time discretization of (2.27) leading to the following non-linear algebraic system:

$$
M\frac{\boldsymbol{\psi}_h^{n+1} - \boldsymbol{\psi}_h^n}{\Delta\tau} + A\boldsymbol{\psi}_h^{n+1} + \boldsymbol{m}(\psi_h^{n+1}) = \boldsymbol{f}^{n+1}
\tag{2.32}
$$

with $\boldsymbol{f}^{n+1} = \boldsymbol{f}(\tau^{n+1})$.

The Newton method is employed for the solution of (2.32). The approximated solution of the steady-state Eikonal problem (2.1) corresponds to the solution of (2.32) at time

instant $\tilde{T}$. The stopping criterion used to retrieve such asymptotic solution is

$$||\boldsymbol{\psi}_h^{n+1} - \boldsymbol{\psi}_h^n||_{L^2(\Omega)} < \text{tol}$$

with tol$= 10^{-10}$.

The numerical counterpart of problem (2.3) has the following form:

$$\psi_h = \mathcal{E}_h(\psi_a).$$

2.2.2. Discretization of the Reaction problem

Problem (2.8) holds in every point $\boldsymbol{x}$ of the domain Ω and it needs only a discretization in time since the spatial points are all decoupled from each other.

Time Discretization

The numerical method employed for the time discretization of problem (2.8a) is the BDF of order 1. On the other hand, equations (2.8b) and (2.8c) are discretized using the first order implicit-explicit scheme (IMEX) where the gating variables $\boldsymbol{w}^{0D}$ are treated implicitly, while the ionic concentrations $\boldsymbol{z}^{0D}$ explicitly. The reason of this choice is that, being equation (2.8b) linear, an implicit treatment of the unknown gating variables does not imply the solution of a non-linear problem, differently to the non-linear equation (2.8c), in which the ionic concentrations are indeed treated explicitly. Moreover, the bound on Δt required by this choice to preserve stability is mild with respect to the accuracy purposes. Therefore, problem (2.8) has the following discretized form:

$$\begin{cases} u_{0D}^{n+1} = u_{0D}^n - \dfrac{\Delta t}{C_m}\left(I_{\text{ion}}(u_{0D}^n, \boldsymbol{w}_{0D}^n, \boldsymbol{z}_{0D}^n) - \dfrac{I_{\text{app}}^n}{\chi}\right), & (2.33\text{a}) \\[2mm] \boldsymbol{w}_{0D}^{n+1} = \boldsymbol{w}_{0D}^n + \Delta t\boldsymbol{h}(u_{0D}^n, \boldsymbol{w}_{0D}^{n+1}), & (2.33\text{b}) \\[2mm] \boldsymbol{z}_{0D}^{n+1} = \boldsymbol{z}_{0D}^n + \Delta t\boldsymbol{g}(u_{0D}^n, \boldsymbol{w}_{0D}^n, \boldsymbol{z}_{0D}^n), & (2.33\text{c}) \end{cases}$$

Solving problem (2.33) only once, off-line with a pre-imposed heartbeat duration, allows to retrieve the 0D calcium concentration $[Ca^{2+}]_{0D,i}^{n+1}$ and to obtain $[Ca^{2+}]_i^{n+1}$ in each point $\boldsymbol{x}$ of the domain Ω, exploiting the relations (2.7) and (2.9). Then, the computed calcium concentration is interpolated in time depending on the time discretization of the mechanical activation problem (2.11) for every mesh point.

The resulting compact form of the discretized version of problem (2.10) is:

$$[Ca^{2+}]_{i,h} = \mathcal{R}_h(\psi_h).$$

2.2.3.   Discretization of the Mechanical Activation problem

Regarding the Active Tension problem (2.11), the discretization is carried out in time and space. The hexahedral mesh of the domain in which the space discretized problem is solved is coarser with respect to the one needed for the Eikonal-diffusion problem (2.1), see Section 2.3.1. But the procedure for the numerical approximation is equal to the one followed in Section 2.2.1.

Weak Formulation

Let the trial space be defined as
$$\boldsymbol{Y} = [L^2(\Omega)]^{20}.$$

The weak formulation of equation (2.11) reads:
Find $\boldsymbol{s}(\boldsymbol{x}) \in \boldsymbol{Y}$ such that

$$\begin{cases} \displaystyle\int_\Omega \frac{d\boldsymbol{s}}{dt} \cdot \boldsymbol{\phi} \, d\Omega = \int_\Omega \boldsymbol{K}\left(\boldsymbol{s}, [Ca^{2+}]_i, SL, \frac{dSL}{dt}\right) \cdot \boldsymbol{\phi} \, d\Omega & \forall \boldsymbol{\phi} \in \boldsymbol{Y}, \ t \in (0,T) \\ \boldsymbol{s}(\boldsymbol{x},0) = \boldsymbol{s}_0(\boldsymbol{x}) & \text{in } \Omega \end{cases} \quad (2.34)$$

Finite Element Formulation

From the weak formulation (2.34) of problem (2.11) it is possible to derive the Galerkin formulation. A triangulation $\mathcal{T}_h$ of characteristic size h made of hexahedra K is introduced, such that
$$\Omega = \bigcup_{K \in \mathcal{T}_h} K.$$

Then, the finite dimensional space $\boldsymbol{Y}_h \subset \boldsymbol{Y}$ is defined introducing the Finite Element (FE) space
$$X_h^1 = \{f_h \in C^0(\bar{\Omega}) : f_h|_K \in \mathbb{Q}^1, \forall K \in \mathcal{T}_h\}$$

and setting $\boldsymbol{Y}_h = [X_h^1]^{20}$. The Galerkin formulation of problem (2.11), written together with the approximated form of equation (2.12) for the active tension T_a, reads:
Find $\boldsymbol{s}_h \in \boldsymbol{Y}_h, \forall t \in (0,T)$, such that

$$\begin{cases} \displaystyle\int_\Omega \frac{d\boldsymbol{s_h}}{dt} \cdot \boldsymbol{\phi}_h \, d\Omega = \int_\Omega \boldsymbol{K}\left(\boldsymbol{s}_h, [Ca^{2+}]_{i,h}, SL_h, \frac{dSL_h}{dt}\right) \cdot \boldsymbol{\phi}_h \, d\Omega & \forall \boldsymbol{\phi}_h \in \boldsymbol{Y}_h \\ T_{a,h} = G(\boldsymbol{s}_h, SL_h) \\ \boldsymbol{s}_h(0) = \boldsymbol{s}_{h,0} \end{cases} \quad (2.35)$$

with $\boldsymbol{s}_{h,0}$ suitable approximation of the initial condition $\boldsymbol{s}_0$.

We introduce $\{\boldsymbol{\varphi}_i\}_{i=1}^{N_s}$ as vector basis of $\boldsymbol{Y}_h$ where $N_s = \dim(\boldsymbol{Y}_h)$, so that the Galerkin solution of (2.35) is written as

$$\boldsymbol{s}_h(\boldsymbol{x}, t) = \sum_{i=1}^{N_s} s_i(t)\boldsymbol{\varphi}_i(\boldsymbol{x}) \qquad \forall t \in (0, T). \tag{2.36}$$

Therefore, set $\boldsymbol{\phi}_h = \boldsymbol{\varphi}_i$ and substitute in the Galerkin formulation (2.35) together with the expression for its solution (2.36) and define the vector of unknowns

$$\mathbf{S}_h = [s_1, ..., s_{N_s}]^T.$$

The Galerkin problem (2.35) becomes:

Find $\mathbf{S}_h = \mathbf{S}_h(t)$ and $T_{a,h} = T_{a,h}(t)$ for every $t \in (0, T)$ such that:

$$\begin{cases} M\dfrac{d\mathbf{S}_h}{dt} = \widetilde{\boldsymbol{K}}\left(\mathbf{S}_h, [Ca^{2+}]_{i,h}, SL_h, \dfrac{dSL_h}{dt}\right) & \text{(2.37a)} \\[2mm] T_{a,h} = G(\mathbf{S}_h, SL_h) & \text{(2.37b)} \\[2mm] \mathbf{S}_h(0) = \mathbf{S}_{h,0} & \text{(2.37c)} \end{cases}$$

where M is the mass matrix given by

$$(M)_{ij} = \int_\Omega \boldsymbol{\varphi}_j \cdot \boldsymbol{\varphi}_i \, d\Omega$$

and $\widetilde{\boldsymbol{K}}$ is a vector defined as

$$(\widetilde{\boldsymbol{K}}(\mathbf{S}_h))_i = \int_\Omega \boldsymbol{K}\left(\boldsymbol{s}_h, [Ca^{2+}]_{i,h}, SL_h, \dfrac{dSL_h}{dt}\right) \cdot \boldsymbol{\varphi}_i \, d\Omega$$

Time Discretization

The semi-discrete problem (2.37) is finally discretized in time dividing the time interval $(0, T)$ in N subintervals (t^n, t^{n+1}) of length Δt so that $t^{n+1} = (n + 1)\Delta t$. The discrete solutions are $\mathbf{S}_h^{n+1} \approx \mathbf{S}_h(t^{n+1})$ and $T_{a,h}^{n+1} \approx T_{a,h}(t^{n+1})$. The time discretization is carried out using a forward Euler method:

$$\begin{cases} M\mathbf{S}_h^{n+1} = M\mathbf{S}_h^n + \Delta t \widetilde{\boldsymbol{K}}\left(\boldsymbol{s}_h^n, [Ca^{2+}]_{i,h}^n, SL_h^n, \frac{dSL_h^n}{dt}\right) & \text{(2.38a)} \\[2mm] T_{a,h}^{n+1} = G(\boldsymbol{s}_h^{n+1}, SL_h^n) & \text{(2.38b)} \\[2mm] \mathbf{S}_h^0 = \mathbf{S}_{h,0} & \text{(2.38c)} \end{cases}$$

The required time step Δt is smaller with respect to the one needed by the mechanics model addressed in Section 2.2.4, for reasons of numerical stability.

The final compact form of problem (2.38) is

$$T_{a,h}^{n+1} = \mathcal{F}_h^{n+1}([Ca^{2+}]_{i,h}^n, \boldsymbol{d}_h^n).$$

2.2.4.   Discretization of the Active and Passive Mechanics

The numerical approximation of the finite elasticity problem (2.14) is carried out with the same strategy seen in previous Section 2.2.3 for the mechanical activation problem. We will state first the weak formulation so that the space discretization via FEM can be obtained, after that, the time discretization is derived. The hexahedral mesh used for this problem is the same used for problem (2.38), so it is coarser than the Eikonal mesh.

Weak Formulation

We define the trial space
$$\boldsymbol{V} = [H^1(\Omega)]^3.$$

The weak formulation of problem (2.14) is:

Find $\boldsymbol{d}(t) \in \boldsymbol{V}$, $\forall t \in (0,T)$ such that

$$\int_\Omega \rho \frac{\partial^2 \boldsymbol{d}}{\partial t^2} \cdot \boldsymbol{\phi} \, d\Omega + \int_\Omega \mathbf{P}(\boldsymbol{d}, T_a) : \nabla \boldsymbol{\phi} \, d\Omega + \int_{\Gamma_{\text{epi}}} \mathbf{K}^{\text{epi}} \boldsymbol{d} \cdot \boldsymbol{\phi} + \mathbf{C}^{\text{epi}} \frac{\partial \boldsymbol{d}}{\partial t} \cdot \boldsymbol{\phi} \, d\Gamma$$
$$= p_{LV}(t) \int_{\Gamma_{\text{base}}} |J\mathbf{F}^{-T}\boldsymbol{n}|\boldsymbol{v}^{\text{base}}(t) \cdot \boldsymbol{\phi} \, d\Gamma - p_{LV}(t) \int_{\Gamma_{\text{endo}}} J\mathbf{F}^{-T}\boldsymbol{n} \cdot \boldsymbol{\phi} \, d\Gamma \qquad \text{(2.39)}$$

for every $\boldsymbol{\phi} \in \boldsymbol{V}$, with initial conditions

$$\begin{cases} \boldsymbol{d}(0) = \boldsymbol{d}_0 & \text{in } \Omega, & \text{(2.40a)} \\[2mm] \dfrac{\partial \boldsymbol{d}}{\partial t}(0) = \dot{\boldsymbol{d}}_0 & \text{in } \Omega & \text{(2.40b)} \end{cases}$$

Tensors $\mathbf{K}^{\text{epi}}$ and $\mathbf{C}^{\text{epi}}$ are defined in (2.16) and $\boldsymbol{v}^{\text{base}}(t)$ as in (2.17).

Finite Element Formulation

From the weak formulation (2.39) we retrieve the Galerkin formulation, using the triangulation $\mathcal{T}_h$ defined in Section 2.2.3 for the mechanical activation problem. The finite dimensional space $\boldsymbol{V}_h \subset \boldsymbol{V}$ is introduced to state the Galerkin formulation:

Find $\boldsymbol{d}_h(t) \in \boldsymbol{V}_h$, $\forall t \in (0, T)$, such that

$$\int_\Omega \rho \frac{\partial^2 \boldsymbol{d}_h}{\partial t^2} \cdot \boldsymbol{\phi}_h d\Omega + \int_\Omega \mathbf{P}(\boldsymbol{d}_h, T_{a,h}) : \nabla \boldsymbol{\phi}_h d\Omega + \int_{\Gamma_{\text{epi}}} \mathbf{K}^{\text{epi}} \boldsymbol{d}_h \cdot \boldsymbol{\phi}_h + \mathbf{C}^{\text{epi}} \frac{\partial \boldsymbol{d}_h}{\partial t} \cdot \boldsymbol{\phi}_h \, d\Gamma$$
$$= p_{LV}(t) \int_{\Gamma_{\text{base}}} |J_h \mathbf{F}_h^{-T} \boldsymbol{n}| \boldsymbol{v}_h^{\text{base}}(t) \cdot \boldsymbol{\phi}_h d\Gamma - p_{LV}(t) \int_{\Gamma_{\text{endo}}} J_h \mathbf{F}_h^{-T} \boldsymbol{n} \cdot \boldsymbol{\phi}_h d\Gamma$$

(2.41)

for every $\boldsymbol{\phi}_h \in \boldsymbol{V}_h$, with initial conditions

$$\begin{cases} \boldsymbol{d}_h(0) = \boldsymbol{d}_{h,0}, & \text{(2.42a)} \\ \dfrac{\partial \boldsymbol{d}_h}{\partial t}(0) = \dot{\boldsymbol{d}}_{h,0} & \text{(2.42b)} \end{cases}$$

where $\boldsymbol{d}_{h,0}$ and $\dot{\boldsymbol{d}}_{h,0}$ are approximations of the initial conditions $\boldsymbol{d}_0$ and $\dot{\boldsymbol{d}}_0$ and

$$\boldsymbol{v}_h^{\text{base}}(t) = \frac{\int_{\Gamma_{\text{endo}}} J_h \mathbf{F}_h^{-T} \boldsymbol{n} \, d\Gamma}{\int_{\Gamma_{\text{base}}} |J_h \mathbf{F}_h^{-T} \boldsymbol{n}| \, d\Gamma}.$$

In order to write the semi-discrete problem, we introduce the same Finite Element space of scalar functions as in Section 2.2.3:

$$X_h^1 = \{f_h \in C^0(\bar{\Omega}) : f_h|_K \in \mathbb{Q}^1, \forall K \in \mathcal{T}_h\}$$

such that $\boldsymbol{V}_h = [X_h^1]^3$ and set $N_d = \dim(\boldsymbol{V}_h)$. Then a vector basis of $\boldsymbol{V}_h$ is defined $\{\boldsymbol{\varphi}_i\}_{i=1}^{N_d}$. The solution $\boldsymbol{d}_h$ of the Galerkin problem (2.41) can be written as the usual linear combination of the elements of the basis:

$$\boldsymbol{d}_h(\boldsymbol{x}, t) = \sum_{i=1}^{N_d} d_i(t) \boldsymbol{\varphi}_i(\boldsymbol{x}) \qquad \forall t \in (0, T).$$

(2.43)

and the vector of unknowns can be defined as

$$\mathbf{D}_h = [d_1, ..., d_{N_d}]^T.$$

Then, setting the test function $\phi_h = \varphi_i$ and substituting (2.43) in (2.41):

$$
\begin{cases}
\rho M \dfrac{d^2 \mathbf{D}_h}{dt^2} + C \dfrac{d\mathbf{D}_h}{dt} + K \mathbf{D}_h + \boldsymbol{P}(\mathbf{D}_h, T_{a,h}) = p_{LV}\boldsymbol{p}(\mathbf{D}_h) & \text{(2.44a)} \\[2mm]
\mathbf{D}_h(0) = \mathbf{D}_{h,0} & \text{(2.44b)} \\[2mm]
\dfrac{d\mathbf{D}_h}{dt}(0) = \dot{\mathbf{D}}_{h,0} & \text{(2.44c)}
\end{cases}
$$

where the FE matrices and vectors read:

$$
(M)_{ij} = \int_\Omega \varphi_j \cdot \varphi_i \, d\Omega, \tag{2.45}
$$

$$
(C)_{ij} = \int_\Omega \mathbf{C}^{\text{epi}} \varphi_j \cdot \varphi_i \, d\Gamma, \tag{2.46}
$$

$$
(K)_{ij} = \int_\Omega \mathbf{K}^{\text{epi}} \varphi_j \cdot \varphi_i \, d\Gamma, \tag{2.47}
$$

$$
(\boldsymbol{P}(\mathbf{D}_h, T_{a,h}))_j = \int_\Omega P(\boldsymbol{d}_h, T_{a,h}) : \nabla \varphi_j \, d\Omega, \tag{2.48}
$$

$$
(\boldsymbol{p}(\mathbf{D}_h))_j = \int_{\Gamma^{\text{base}}} |J_h \mathbf{F}_h^{-T} \boldsymbol{n}| \boldsymbol{v}_h^{\text{base}}(t) \cdot \varphi_j \, d\Gamma - \int_{\Gamma^{\text{endo}}} J_h \mathbf{F}_h^{-T} \boldsymbol{n} \cdot \varphi_j \, d\Gamma. \tag{2.49}
$$

Time Discretization

Concluding with the time discretization of the non-linear system of ODEs (2.44), it is obtained with BDF1 scheme, dividing the time interval $(0, T)$ as in Section 2.2.3 in N subintervals (t^n, t^{n+1}) of length Δt. The discrete solution is $\mathbf{D}_h^{n+1} \approx \mathbf{D}_h(t^{n+1})$ and it satisfies the following problem:

Find $\mathbf{D}_h^{n+1}$ such that

$$
\begin{aligned}
\left(\rho \frac{1}{\Delta t^2} M + \frac{1}{\Delta t} C + K\right) \mathbf{D}_h^{n+1} + P(\mathbf{D}_h^{n+1}, T_{a,h}^{n+1}) = \\
\rho \frac{2}{\Delta t^2} M \mathbf{D}_h^n - \rho \frac{1}{\Delta t^2} M \mathbf{D}_h^{n-1} + \frac{1}{\Delta t} C \mathbf{D}_h^n + p_{LV}^{n+1} \boldsymbol{p}(\mathbf{D}_h^{n+1})
\end{aligned} \tag{2.50}
$$

with initial conditions

$$
\begin{cases}
\mathbf{D}_h(0) = \mathbf{D}_{h,0}, \\
\dfrac{\partial \mathbf{D}_h}{\partial t}(0) = \dot{\mathbf{D}}_{h,0}.
\end{cases}
$$

The compact form of problem (2.50) reads:

$$\boldsymbol{d}_h^{n+1} = \widetilde{\mathcal{M}}_h^{n+1}(T_{a,h}^{n+1}, p_{LV}^{n+1}, \boldsymbol{d}_h^{n+1}). \tag{2.51}$$

2.2.5. Discretization of the Mechanics and 0D Hemodynamics coupled problem

In this section we present the algorithm employed in [113, 115] for the solution of the coupling between the mechanics and the 0D circulation model, needed to compute the LV pressure $p_{LV} = p_{LV}^{0D}$ appearing in the boundary conditions (2.14d) and (2.14c) of problem (2.14).

The 0D circulation model is solved at each time step t^{n+1} and the pressure $p_{LV}^{0D,n+1}$ is computed in a different way depending on the current phase of the cardiac cycle. The updated solution of the 0D model is used to determine the solution $\boldsymbol{d}_h^{n+1}$ of the numerically approximated finite elasticity problem (2.51).

When it is needed, the 3D LV volume at time step t^{n+1} is computed explicitly from the displacement at time t^n:

$$V_{LV}^{3D,n+1} = \int_{\Gamma_{\text{endo}}} J_h^n((\boldsymbol{h} \otimes \boldsymbol{h})(\boldsymbol{x} + \boldsymbol{d}_h^n - \boldsymbol{b})) \cdot \mathbf{F}_h^{-T,n} \boldsymbol{n} \, d\Gamma \tag{2.52}$$

The discretized mechanics/hemodynamics coupled problem during each phase of the cardiac cycle is reported below.

1. **Isovolumetric contraction**:
   Find $(\boldsymbol{d}_h^{n+1}, p_{LV}^{0D,n+1})$, given $(\boldsymbol{d}_h^0, p_{LV}^{0D,0}) = (\boldsymbol{d}_{0,h}, \bar{p}_{\text{ED}}^{0D})$ and $V_{LV}^{0D,0} = EDV$, such that:

$$\begin{cases} V_{LV}^{3D,n+1} = V_{LV}^{3D,n} & \text{(2.53a)} \\ \boldsymbol{d}_h^{n+1} = \widetilde{\mathcal{M}}_h^{n+1}(T_{a,h}^{n+1}, p_{LV}^{0D,n+1}, \boldsymbol{d}_h^{n+1}) & \text{(2.53b)} \end{cases}$$

   until $p_{LV}^{0D,n+1} = \bar{p}_{\text{AVO}}^{0D}$ at time instant $t^{n+1} = t_{\text{AVO}}$.

2. **Ejection**:

   a. Find $p_{LV}^{0D,n+1}$ such that

$$p_{LV}^{0D,n+1} = \frac{RC}{RC + \Delta t} p_{LV}^{0D,n} + \frac{R}{RC + \Delta t}(V_{LV}^{3D,n+1} - V_{LV}^{3D,n}). \tag{2.54}$$

   until $V_{LV}^{3D,n+1} - V_{LV}^{3D,n}$ changes sign at time instant $t^{n+1} = t_{\text{AVC}}$. Set $p_{LV}^{0D}(t_{\text{AVC}}) =$

$\bar{p}_{\text{AVC}}^{0D}$.

   b. Find $\boldsymbol{d}_h^{n+1}$ such that

$$\boldsymbol{d}_h^{n+1} = \widetilde{\mathcal{M}}_h^{n+1}(T_{a,h}^{n+1}, p_{LV}^{0D,n+1}, \boldsymbol{d}_h^{n+1}).$$

3. **Isovolumetric relaxation**:
   Find $(\boldsymbol{d}_h^{n+1}, p_{LV}^{0D,n+1})$, given $\boldsymbol{d}_h(t_{\text{AVC}})$, $p_{LV}^{0D}(t_{\text{AVC}}) = \bar{p}_{\text{AVC}}^{0D}$ and $V_{LV}^{0D}(t_{\text{AVC}}) = ESV$ from previous phase, such that:

$$\begin{cases} V_{LV}^{3D,n+1} = V_{LV}^{3D,n} & (2.55a) \\ \boldsymbol{d}_h^{n+1} = \widetilde{\mathcal{M}}_h^{n+1}(T_{a,h}^{n+1}, p_{LV}^{0D,n+1}, \boldsymbol{d}_h^{n+1}) & (2.55b) \end{cases}$$

  until $p_{LV}^{0D,n+1} = \bar{p}_{\text{MVO}}^{0D}$ at time instant $t^{n+1} = t_{\text{MVO}}$.

4. **Filling**:

   a. Linearly increase $p_{LV}^{0D,n+1}$ until $p_{LV}^{0D,n+1} = \bar{p}_{\text{ED}}^{0D}$ and update $V_{LV}^{3D,n+1}$.

   b. Find $\boldsymbol{d}_h^{n+1}$ such that

$$\boldsymbol{d}_h^{n+1} = \widetilde{\mathcal{M}}_h^{n+1}(T_{a,h}^{n+1}, p_{LV}^{0D,n+1}, \boldsymbol{d}_h^{n+1}).$$

Phases 1 and 3 give rise to two saddle point problems (2.53) and (2.55), because of the constraint imposing volume to remain constant and equal to EDV and ESV, respectively. These probelms are solved by means of a Schur complement reduction [102]. Phase 2 solves the discretized Windkessel model (2.54) by means of BDF1 scheme. The nonlinear active/passive mechanics problem (2.51) is solved at each phase of the cardiac cycle applying Newton algorithm.

The discretized 0D model for circulation solved at every phase is compactly addressed by

$$p_{LV}^{0D,n+1} = \widetilde{\mathcal{C}}(\boldsymbol{d}_h^n).$$

2.2.6. Algorithm for the numerical solution of ERM model

In this Section we sum up the numerical method for the solution of the Eikonal-Reaction-Mechanics problem. We schematically represent it through the following algorithm reported in [113, 115] which is implemented in the `life`$^{\texttt{x}}$ library. Indicate by $N = \frac{T}{\Delta t}$, with T final time and Δt time step required for the mechanics/0D hemodynamics problem.

Algorithm 2.1 Numerical solution of ERM problem

1: Solve the Eikonal-diffusion problem (2.32) $\psi_h = \mathcal{E}_h(\psi_a)$ given the datum ψ_a;
2: Solve the Reaction problem (2.33) to retrieve $[Ca^{2+}]_{i,h} = \mathcal{R}_h(\psi_h)$;
3: **for** $0 \leq n \leq N$ **do**
4:     Interpolate $[Ca^{2+}]_{i,h}$ in time to get $[Ca^{2+}]_{i,h}^n$;
5:     Solve $T_{a,h}^{n+1} = \mathcal{F}_h^{n+1}([Ca^{2+}]_{i,h}^n, \boldsymbol{d}_h^n)$ with a finer time step as mentioned in Section 2.2.3;
6:     **if** *isovolumetric contraction* **then**
7:         Find $(\boldsymbol{d}_h^{n+1}, p_{LV}^{0D,n+1})$ such that

$$\begin{cases} V_{LV}^{3D,n+1} = EDV, \\ \boldsymbol{d}_h^{n+1} = \widetilde{\mathcal{M}}_h^{n+1}(T_{a,h}^{n+1}, p_{LV}^{0D,n+1}, \boldsymbol{d}_h^{n+1}), \end{cases}$$

8:         until $p_{LV}^{0D,n+1} = \bar{p}_{AVO}^{0D}$;
9:     **else if** *ejection* **then**
10:        Solve the Windkessel model

$$p_{LV}^{0D,n+1} = \frac{RC}{RC + \Delta t} p_{LV}^{0D,n} + \frac{R}{RC + \Delta t}(V_{LV}^{3D,n+1} - V_{LV}^{3D,n})$$

        until $V_{LV}^{3D,n+1} - V_{LV}^{3D,n}$ changes sign;
11:        Solve $\boldsymbol{d}_h^{n+1} = \widetilde{\mathcal{M}}_h^{n+1}(T_{a,h}^{n+1}, p_{LV}^{0D,n+1}, \boldsymbol{d}_h^{n+1})$;
12:     **else if** *isovolumetric relaxation* **then**
13:         Find $(\boldsymbol{d}_h^{n+1}, p_{LV}^{0D,n+1})$ such that

$$\begin{cases} V_{LV}^{3D,n+1} = ESV, \\ \boldsymbol{d}_h^{n+1} = \widetilde{\mathcal{M}}_h^{n+1}(T_{a,h}^{n+1}, p_{LV}^{0D,n+1}, \boldsymbol{d}_h^{n+1}), \end{cases}$$

14:         until $p_{LV}^{0D,n+1} = \bar{p}_{MVO}^{0D}$;
15:     **else if** *filling* **then**
16:        Linearly increase $p_{LV}^{0D,n+1}$ until $p_{LV}^{0D,n+1} = \bar{p}_{ED}^{0D}$;
17:        Update $V_{LV}^{3D,n+1}$ with (2.52);
18:        Solve $\boldsymbol{d}_h^{n+1} = \widetilde{\mathcal{M}}_h^{n+1}(T_{a,h}^{n+1}, p_{LV}^{0D,n+1}, \boldsymbol{d}_h^{n+1})$.
19:     **end if**
20: **end for**

2.3. Geometric Data for ERM numerical solution

In order to use Algorithm 2.1 to simulate the ERM model, some geometric information must be included, regarding the LV domain Ω, the myocardial fibers orientation, the Purkinje fibers, and the location of fibrotic tissue, if it is present.

2.3.1. Mesh Generation

The segmentation procedure to obtain a LV computational domain starting from clinical data will be addressed in Chapter 3, at Section 3.1.1, when we will introduce our patient-specific cases.

Once a LV closed surface is availabe, the procedure of mesh generation is performed using meshing tools developed in the `vmtk` software (`www.vmtk.org`) [44]:

1. A triangular surface mesh is generated for the LV closed surface choosing a desired characteristic size.

2. A tetrahedral solid mesh is constructed starting from the triangulation of LV surface.

3. The tetrahedra of the solid mesh are tranformed into hexahedra to obtain the desired 3D LV mesh for the current computational framework.

As mentioned in Section 2.2.3, the Eikonal and the Mechanics problem need two different mesh refinements that guarantee convergence and stability of the numerical method. In particular, the Eikonal mesh size is around $h \simeq 1\ mm$ (Figure 2.3a), while the characteristic size for the mechanics is $h \simeq 3 - 4\ mm$ (Figure 2.3b).

(a) Eikonal fine mesh   (b) Mechanics coarse mesh
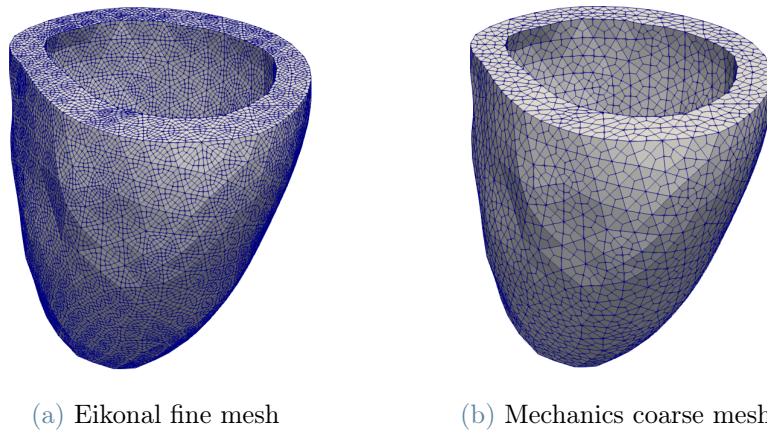
Figure 2.3: Different mesh refinements for electrical and mechanics problems (geometry from Zygote 3D Human Heart Model [1])

In Figure 2.3 we give an example of the fine and coarse meshes generated for the LV geometry of Zygote 3D Human Heart Model [1].

2.3.2. Myocardial Fibers Reconstruction

The orientation of myocardial fibers is a fundamental information for the solution of the ERM problem, in particular for the Eikonal-diffusion problem (2.1) where the fibers $\boldsymbol{f}$, sheets $\boldsymbol{s}$ and normal $\boldsymbol{n}$ directions are needed to compute the conductivity tensor $\mathbf{D}$ (2.2) in order to account for the higher electrical propagation velocity along fibers with respect to crossfiber directions.

However, as we mentioned in Section 2.1.1, standard imaging techniques, like MRI, are not able to provide the geometry distribution of myocardial fibers since their dimension is usually smaller than the spatial resolution of such techniques. For this reason, rule-based algorithms are employed to reproduce fibers orientation.

In the present work, as it was done in [113], we rely on a Laplace-Dirichlet rule-based algorithm, the *Bayer-Blake-Plank-Trayanova* (BT) algorithm, proposed in [10], which is implemented in `life`^x. In particular, a linear rule [95] is used with boundary values equal to $\alpha_{\text{epi}} = -60°$ for fibers at the epicardium, $\alpha_{\text{endo}} = 60°$ for fibers at the endocardium, $\beta_{\text{epi}} = 20°$ for sheets at the epicardium and $\beta_{\text{endo}} = -20°$ for sheets at the endocardium. An example of the output of this algorithm applied to LV geometry of Zygote 3D Human Heart Model [1] is reported in Figure 2.4.

(a) Directions $\boldsymbol{f}$, $\boldsymbol{s}$ and $\boldsymbol{n}$ in a point of the epicardium.

(b) Fibers distribution in the myocardium.
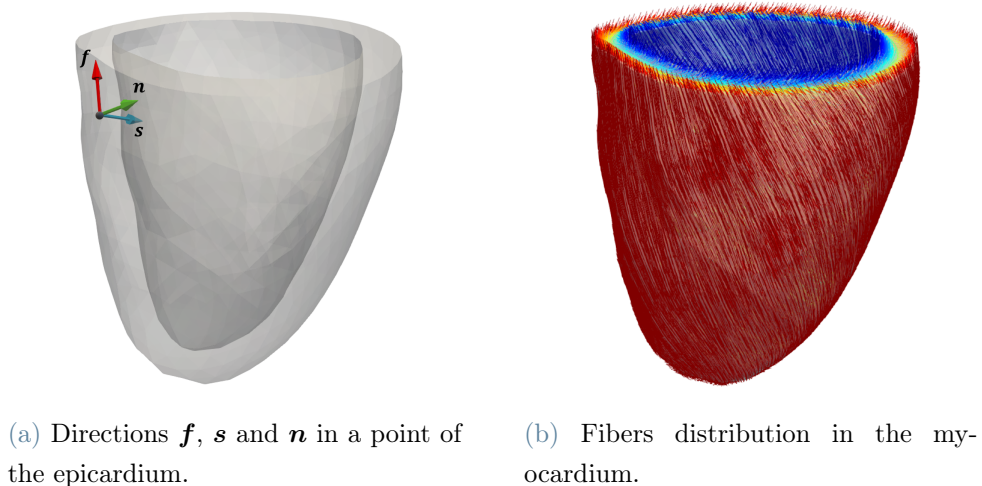
Figure 2.4: Reconstructed fibers geometry using the Bayer-Blake-Plank-Trayanova rule-based algorithm on Zygote LV [1].

2.3.3.   Purkinje Fibers Surrogate

In the present mathematical model, the Purkinje network, which is fundamental for electrical propagation in the ventricles, is not included. Its functioning is surrogated imposing stimuli at the interventricular septum [129], represented by the input datum ψ_a given to the Eikonal-Diffusion problem (2.3) as Dirichlet boundary condition (see Section 2.1.1). In this thesis, we will impose for all Eikonal simulations spherical stimulation sites, whose radius will be set equal to 0.7 mm. Moreover, the value of each imposed activation time, when reproducing synus rhythm scenarios, will be of the order of 10^{-5} s with delays between each other so that a the characteristic conduction velocity in the Purkinje network of about 500 cm s^{-1} can be reproduced [63, 130].

2.3.4.   Inclusion of fibrotic tissue

The final goal of a mathematical model for cardiac function is to be able to virtually reproduce also pathological scenarios. This is indeed the objective of the thesis and it is achieved exploiting the ERM model.

In particular, another element that may be included in the electrophysiology framework is the distribution of scar tissue in the LV myocardium. Such information is retrieved from clinical images when dealing with patient-specific simulations.

The ERM mathematical model accounts for the presence of fibrosis with the Eikonal equation (2.1), by means of the parameter z appearing in the conductivity tensor **D** (2.2). When $z < 1$ the electrical conductivities are reduced in all directions by the same factor causing a slowdown of the wave propagation. The value of z can vary in space to distinguish between healthy and fibrotic regions of the LV volume.

In the present work, this spatial variation is included by projecting clinical bullseye plots on the 3D left ventricle (see Chapter 3 at Section 3.1.2). The result is a 3D LV geometry that is subdivided in 17 regions labelled with a value between 0 and 1, representing the aforementioned parameter z. Then, the 3D fibrosis distribution is interpolated on the LV fine mesh for the Eikonal problem by means of a preprocessing procedure implemented in `lifeˣ`, whose output mesh will have every point assigned with a value of z and it will be given in input to the EP simulation.

3 | Calibration Procedure

In this Chapter we will show the first results of the thesis, concerning the calibration of the Eikonal-Reaction-Mechanics (ERM) model with patient-specific clinical data provided by the Hospital of S. Maria del Carmine in Rovereto (TN), Italy. In particular, we will work on three different patients affected by LBBB who underwent cardiac resynchronization therapy implantation. In two of them presence of fibrosis was detected.

In first Section 3.1 we will briefly explain the clinical techniques used to acquire geometric and electrical data for each patient and the subsequent procedures for the reconstruction of 3D left ventricle geometry, fibrosis distribution and epicardial veins geometry needed as input data for the computational model. In Section 3.2 we will address the calibration procedure of the Eikonal model (2.1) for each patient, using clinically measured activation times (ATs) at the septum and at the epicardial veins. In the end, Section 3.3 shows the results of the calibration of the active/passive mechanics (2.14) coupled with the 0D circulation model (2.21). Electro-mechanical simulations are run for the patients in the pre-CRT scenario, simulating the LBBB pathology and the consequent LV dyssynchronous contraction.

3.1. Acquisition and Processing of Patient-specific Data

The medical data and images acquisition carried out by the Hospital of S. Maria del Carmine in order to retrieve geometric/anatomical and electrical information relied on the Magnetic Resonance Imaging technique and on the Electro-Anatomical Mapping System, respectively:

- Cardiac *Magnetic Resonance Imaging* (MRI) is a non-invasive and safe procedure for the patients. It provides three sequences of black and white images of the heart, one for each axis of acquisition x, y and z. This technique exploits the physical phenomenon of nuclear magnetic resonance, generating a strong magnetic field around the patient's heart which perturbs atomic nuclei of the hydrogen protium isotope ^1H. The rate at which excited atoms return to the equilibrium state produces the contrast between different tissues and the subsequent grayscale images. When

such images need to be clearer *contrast-enhanced MRI* is employed, giving contrast agents to the patient. On the other hand, when the interest is on ventricles motion, *cineMRI* is used since it allows to acquire images at multiple time instants of the cardiac cycle.

- The *Electro-Anatomical Mapping System* (EAMS) is a quite invasive and time-consuming procedure that allows the measurement of locations and timings of the electrical signal propagation using multiple electrode catheters on the endocardial or epicardial surfaces of the heart that are able to record intracardiac ECGs over several heartbeats. In particular, this electrograms provide the local activation time, which is defined as the time at which the transmembrane potential reached the mean value between the resting potential and the action potential. A particular technique that guarantees space and time accuracy in the acquisition of electrical data is the contact *EnSite Precision^{TM}* cardiac mapping system [43].

In the next sections we will address the medical strategies employed by cardiologists of the Hospital of S. Maria del Carmine and the processing techniques applied to the resulting clinical measures and images in order to make them compatible with the ERM computational framework. These procedures of geometric and electrical reconstruction were carried out in [113] on twelve patients. In this work we will analyze three of them, indicated as P2, P5 and P8.

3.1.1. Segmentation of Left Ventricle Geometries

The 3D left ventricular geometries of the three patients were reconstructed from MRI images following a semi-automatic segmentation procedure described in [113] that allows to identify and separate in each digital image the main cardiac structures and compartments. First, LV endocardial and epicardial surfaces were manually segmented using an appropriate software (Medical Imaging Interaction Toolkit - MITK), obtaining two closed surfaces for the epicardium and the endocardium (see Figure 3.1 for an example of the endocardium). Then, using the already mentioned `vmtk` software [44], endocardium and epicardium are obtained by capping the closed surfaces and subsequently, they are merged together constructing a surface for the LV base. So that the LV closed surface is obtained. The resulting LV volumes for patients P2, P5 and P8 are showed in Figure 3.2. These are the computational domains for the ERM simulations that will be performed in the present work.
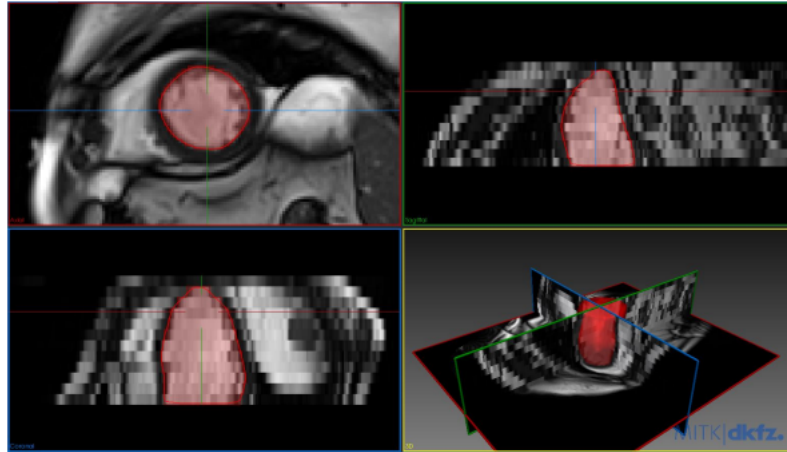
Figure 3.1: Example of segmented endocardial closed surface in two different MRI slices (taken from [115]). Top left is the axial view, top right is the sagittal view, bottom left is the coronal view and bottom right is the 3D view.

(a) Patient P2   (b) Patient P5   (c) Patient P8
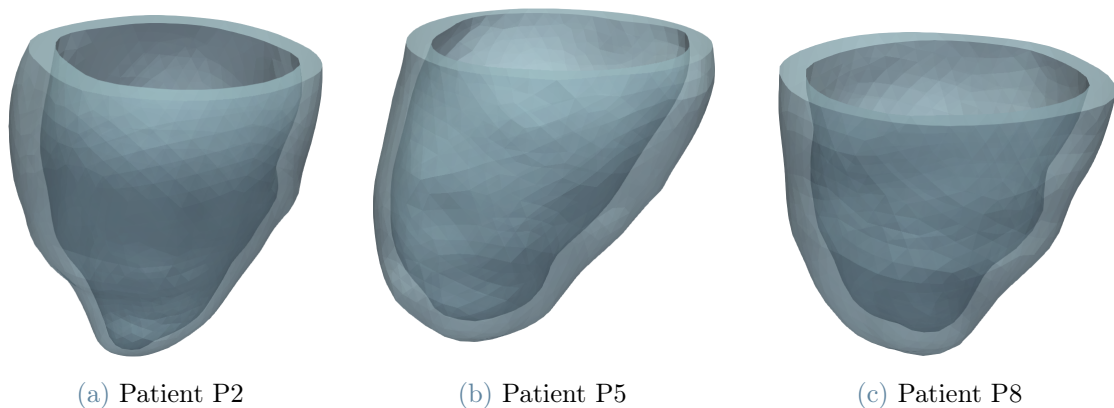
Figure 3.2: Reconstructed LV geometries of patients P2, P5 and P8, from [113]

The last step that is required in order to employ such geometries in our computational framework, is the mesh generation, whose procedure was explained in previous Chapter, in Section 2.3.1. For each patient we constructed a coarse mesh for the resolution of the mechanic problem using `vmtk` software, imposing a desired mesh size (see Figures 3.3a, 3.3b and 3.3c). When dealing with Eikonal model simulations, these meshes are refined within the `life`^{x} library itself imposing the right number of refinements. Being the characteristic mesh size for the mechanics about 4 times the one required for electrophysiology, we impose 2 refinements of the coarse mesh, which entails the subdivision of a single mesh element in 16 smaller hexahedra (see Figures 3.3d, 3.3e and 3.3f). We report in Figure 3.3 the patient-specific coarse and fine meshes, together with their average mesh size, that

were used in this thesis for electro-mechanical simulations.

(a) P2: $\bar{h} = 3.7\ mm$ (b) P5: $\bar{h} = 3.6\ mm$ (c) P8: $\bar{h} = 3.5\ mm$

(d) P2: $\bar{h} = 0.94\ mm$ (e) P5: $\bar{h} = 0.91\ mm$ (f) P8: $\bar{h} = 0.89\ mm$
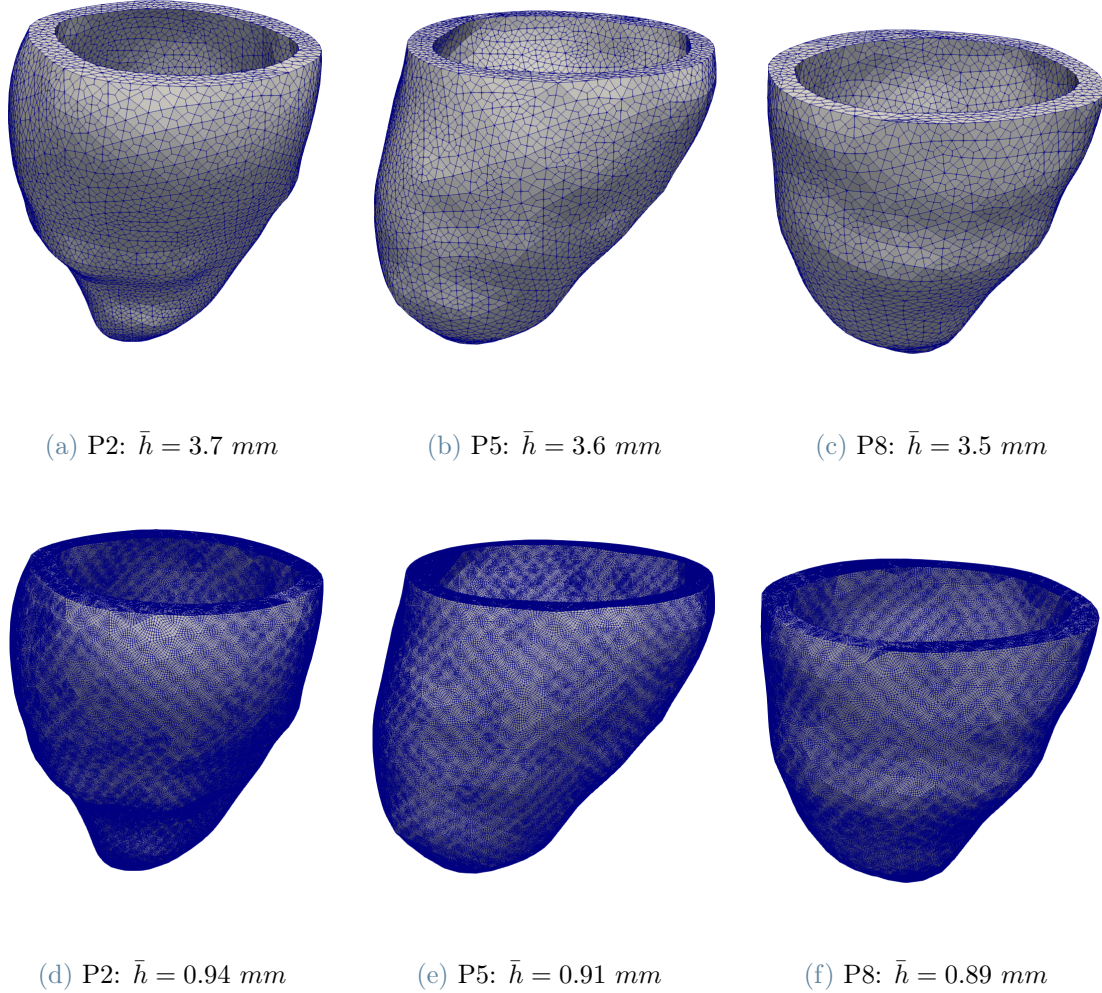
Figure 3.3: Coarse mesh (on the top) for mechanics and fine mesh (on the bottom) for electrophysiology generated for patients P2, P5 and P8.

3.1.2. Fibrosis Distribution Reconstruction

Among the three patients analyzed in this thesis, patients P5 and P8 were diagnosed with fibrosis. The possible techniques adopted by clinicians for the diagnosis and the identification of its distribution are mentioned in Section 1.1.4. In particular, radiologists in Rovereto obtained bullseye plots of these patients by means of two particular MRI sequences, *phase sensitive inversion recovery* (PSIR) and post-contrast *cine balanced steady state free precession* (cineSSFP). A procedure was developed in [113] to subdivide the 3D LV geometry in the 17 regions corresponding to the bullseye plot segments. First, the position of the septum was identified segmenting also the RV surface in order to orient the

bullseye plot with respect to the LV surface. Using the Paraview software Python shell, the LV geometry was manually subdivided in 17 volumes and each of them was assigned with a tag value between 0 and 1 representing the presence and the degree of fibrosis. Then the 17 elements were re-assembled to generate the 3D fibrosis distribution in the LV volume.

The tag value assigned to each subvolume is what we denoted by z in the Eikonal model (2.1) and it is one of the parameters that are adjusted in order to perform the electrical calibration (see Section 3.2). The indication of clinicians for patients P5 and P8 was a degree of fibrosis above 50%. The 3D fibrosis distributions for these patients, obtained in [113] with the procedure described above, is reported in Figure 3.4 together with the bullseye plots provided by clinicians.
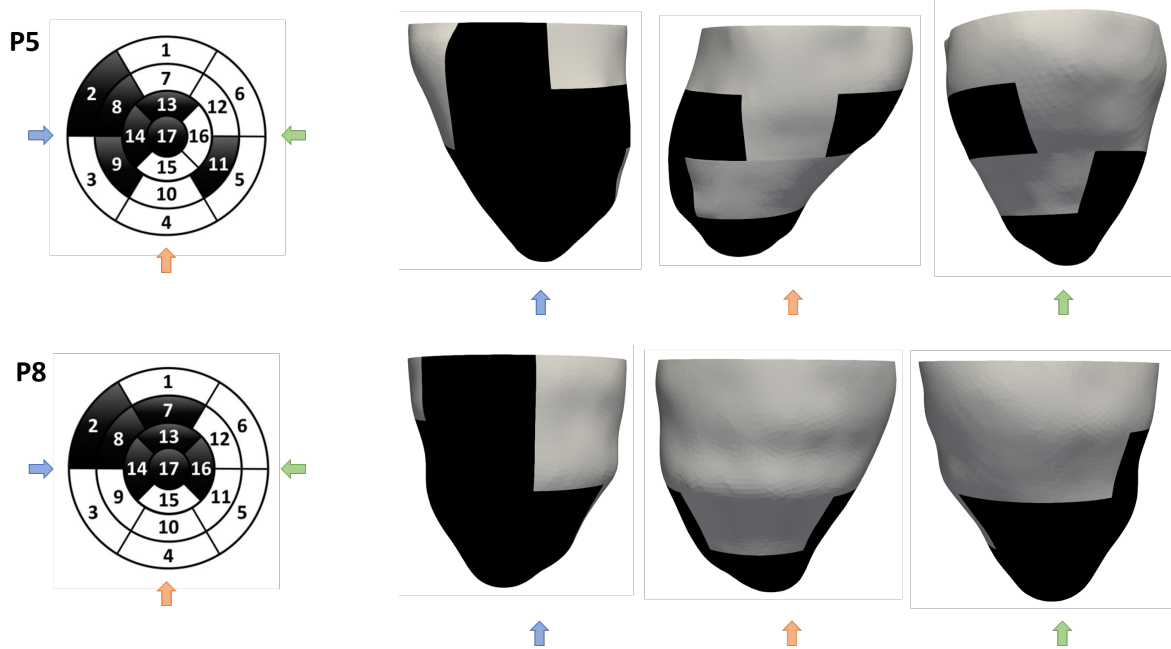
Figure 3.4: Bullseye plot subdivisions and reconstructed 3D fibrosis distributions for patients P5 (top) and P8 (bottom). Fibrotic regions are in black (tag value $z > 0.5$ to be estimated) and healthy regions are in white (tag value $z = 1$).

3.1.3. Processing of Electrical Data

The measurement of electrical data was performed at the Hospital of S. Maria del Carmine with the EnSite Precision™ electro-anatomical mapping system, inserting electrode catheters in the coronary sinus branches and in the endocardial RV septum. This procedure was carried out during the Cardiac Resynchronization Therapy (CRT) implantation pro-

cedure [35], so that at the end of the data acquisition phase in which local activation maps are recorded, CRT leads were positioned in the RA, RV and at the latest electrically activated site (LEAS) for the LV lead. EAMS measures of electrical activity were provided for P2, P5 and P8 in the easily readable *.csv* format, consisting of point coordinates and corresponding activation time for each recorded location. In particular, for P2 and P5 local activation times were acquired both at the epicardial veins and at the septum, while only LV epicardial measurements were available for P8.

(a) Patient P2   (b) Patient P5   (c) Patient P8
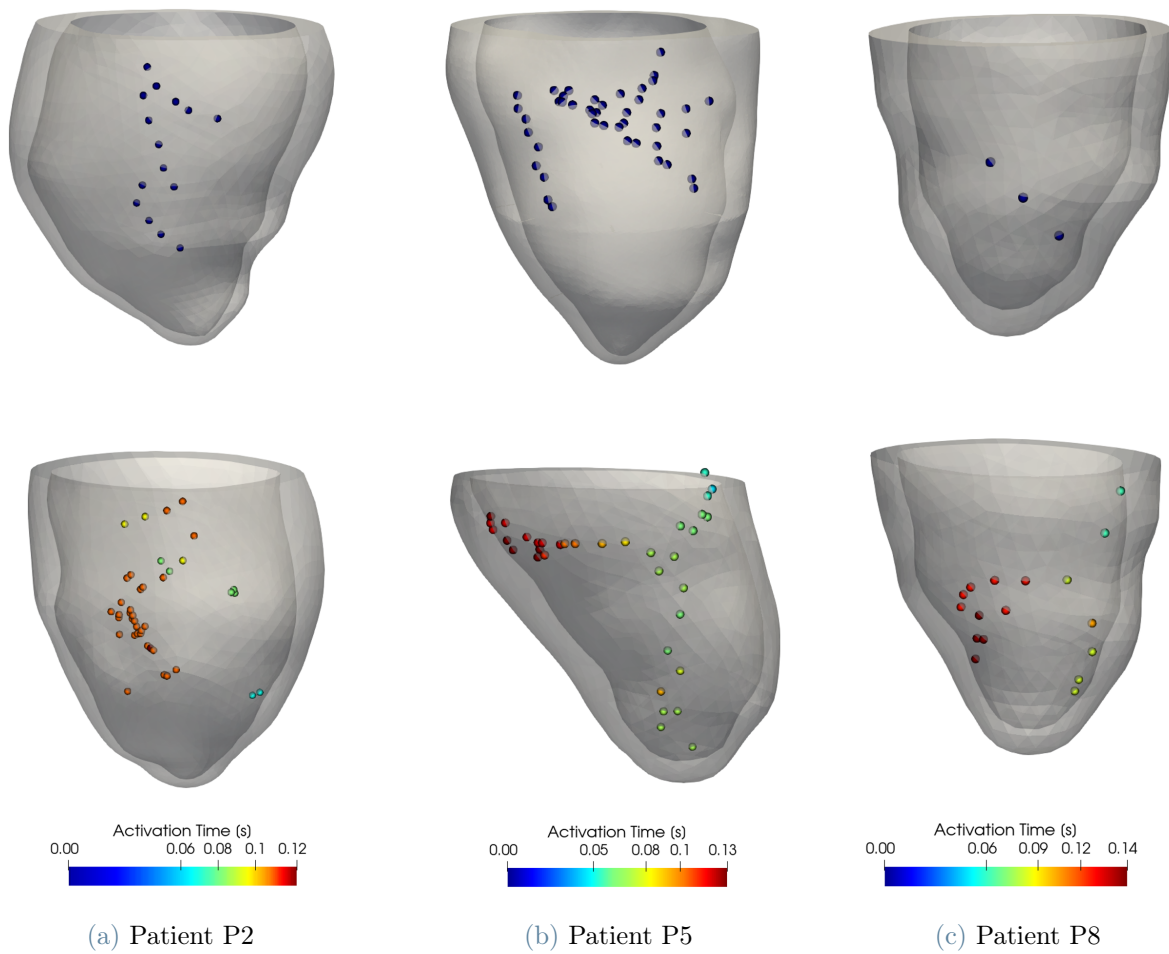
Figure 3.5: Cloud of points with measured ATs at the septum (top) and at the epicardial veins (bottom), projected on the reconstructed LV external surface [114]. Septal points for P8 are imposed by us beacuse of lack of clinical measures.

Once these measures were acquired, they had to be merged with the reconstructed LV geometry in order to make them compatible with the computational framework. This was done in [113] following the alignment procedure explained in [114] that was carried out

using MATLAB and Paraview software. For each patient reference points were selected both on the reconstructed LV epicardial surface and among the electrical data. The latter were rotated and translated in space to match the points selected on the ventricular geometry. In conclusion an Euclidean *nearest neighbor search projection* (NNS) was applied to select for each electrical point of the cloud the closest point on the LV epicardium in terms of Euclidean distance, so that the cloud of points could entirely lay on the external LV surface. The results of the application of this method on patients P2, P5 and P8 are reported in Figure 3.5. We highlight that for patient P8 septal electrical data were not available, indeed, as one can see in Figure 3.5c, three selected points at the septum were used to surrogate the LBBB-like electrical propagation and given as input data to the Eikonal model (see Section 3.2).

3.1.4. Epicardial Veins Reconstruction

Another relevant geometric element for the purpose of the thesis is the anatomy of the coronary sinus (CS) together with its main branches. However, MRI images have a resolution which is not fine enough to be able to detect coronary veins. Hence, the method employed in [113] proposes to reconstruct an approximated geometry of these vessels exploiting the locations of the electrical data acquired at the epicardium by means of EAMS. Specifically, the anatomy of epicardial veins is retrieved through the use of splines, which is a mathematical tool for interpolation (see Figure 3.6).

<div align="center">(a) Patient P2　　　　(b) Patient P5　　　　(c) Patient P8</div>
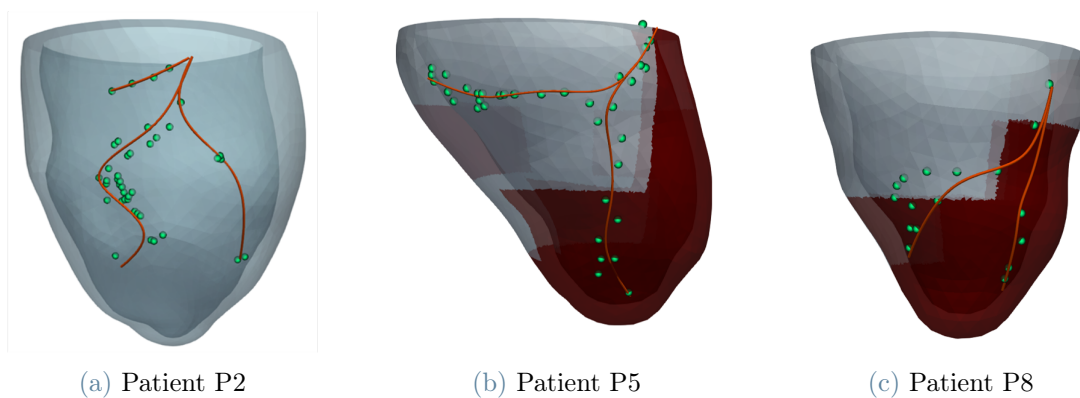
Figure 3.6: Reconstructed geometries of the coronary veins obtained with splines of the epicardial activation maps [113]. For patients P5 and P8 the fibrosis distribution is included.

The Paraview software was used in [113] to identify for each patient the number of vessels to be reconstructed. After that, first and last control points were selected as the most

proximal and distal activation points, respectively. Finally, a variable number of control points in the middle is chosen to determine a curvature of the spline that can lead to a geometry which is the closest possible to the distribution of recorded electrical data and consequently to the real veins anatomy.

An available anatomy of coronary veins turns out to be useful when approaching the simulation of virtual CRT scenarios (in Chapter 4), in order to determine the position of the computational LEAS and to select other possible LV lead locations, since we know from clinicians that the CRT left ventricular catheter is placed inside CS tributaries.

3.2.   Electrical Calibration

Given the electrical and geometric data adapted to the ERM computational framework as reported in previous Section 3.1, relying on the techniques proposed in [113, 114, 131], we proceed with our calibration of the Eikonal model for patients P2, P5 and P8.

In general, calibration of a computational model concerns the estimation of its parameters (all or just a portion of them) by comparison of the resulting numerical simulations with measured patient-specific data that were previously adapted to the particular computational context. The final values of the model parameters are determined minimizing the discrepancy between simulated and clinical measures, defining suitable relative errors. The minimization of the error can be carried out using either numerical optimization methods or not, i. e. direct search methods [114, 131].

In the present thesis, having a small number of patients and being the eikonal simulations fast, we did not rely on any numerical method.

The compact form of the Eikonal model (2.3), $\psi = \mathcal{E}(\psi_a)$, highlights the necessity of providing the input datum ψ_a. In this work we represent it using locations and timings of electrical data recorded at the septum for patients P2 and P5 (see Figures 3.5a and 3.5b), while three selected points at the septum are chosen for P8 to make up for the lack of clinical measures (Figure 3.5c). In all three cases, such input data are imposed as spherical stimuli with radius of 0.7 mm as explained in Section 2.3.3.

The other available electrical data acquired at the CS and at its branches, reported in Figure 3.5, are used to evaluate the discrepancy with respect to the simulated activation maps and the accuracy of the calibration.

In order to estimate the Eikonal parameters for our patients, we start from initial values for Zygote LV [1], that were estimated and tested in [115].

3.2.1. Default Eikonal model parameters

When setting an Eikonal simulation, seven quantities need to be fixed, besides the input datum ψ_a. Moreover, when fibrosis is included, an eighth parameter arises to take into account the slow conduction regions, as we will see in next Section 3.2.2 for patients P5 and P8.

Firstly, referring to the mathematical formulation of Eikonal model (2.1), for all simulations we will set $\chi = 10^5 \ m^{-1}$ and $C_m = 0.01 \ Fm^{-2}$ taken from [47]. Secondly, we will refer to a normalized version of electrical conductivities in the three directions $\boldsymbol{f}$, $\boldsymbol{s}$ and $\boldsymbol{n}$ given by $\hat{\sigma}_i = \frac{\sigma_i}{\chi C_m}$ with $i = \{f, s, n\}$.

The values for $\hat{\sigma}_f$, $\hat{\sigma}_s$ and $\hat{\sigma}_n$ and for the other two parameters c_0 and ε are not fixed, but will be estimated for each patient. As well as the value of z defining the degree of fibrosis. The initial values of these quantities, calibrated on the LV of Zygote Solid 3D heart [1], are reported below in Table 3.1.

Parameter	Value
$\hat{\boldsymbol{\sigma}}_f \ \ [m^2 s^{-1}]$	$0.7643 \cdot 10^{-4}$
$\hat{\boldsymbol{\sigma}}_s \ \ [m^2 s^{-1}]$	$0.3494 \cdot 10^{-4}$
$\hat{\boldsymbol{\sigma}}_n \ \ [m^2 s^{-1}]$	$0.1125 \cdot 10^{-4}$
$\mathbf{c_0} \ \ [s^{-1/2}]$	73.3627646
ε	14.9502645

Table 3.1: Reference parameters of the Eikonal model for Zygote LV, taken from [115].

Concerning myocardial fibers distribution to determine directions $\boldsymbol{f}$, $\boldsymbol{s}$ and $\boldsymbol{n}$, we have already pointed out in Section 2.3.2 that their reconstruction is not patient-specific but it is obtained with the Bayer-Blake-Plank-Trayanova (BT) rule based algorithm [10], whose boundary values of fibers and sheets orientations are also parameters that are set in the Eikonal code and that we will keep fixed to the reference values of [115].

We will use as pseudo-time step for the Eikonal numerical solution $\Delta\tau = 0.01 \ s$, a final time $\tilde{T} = 10 \ s$ and set the steady-state tolerance to tol $= 10^{-10}$. We remark that the unit measure of τ has no physical meaning.

3.2.2. Patient-specific Eikonal simulations

Eikonal simulations are performed using the code implemented in the high-performance C++ library life$^\text{x}$ (https://lifex.gitlab.io/lifex), on LV patient-specific meshes

(see Figures 3.3d for P2, 3.3e for P5 and 3.3f for P8).

The estimation of the Eikonal parameters for each patient starts from the values reported in Table 3.1, that are used to run a preliminary simulation which produces, besides the activation map in all the LV domain, also the solution of BT algorithm for fibers geometry. We report the reconstructed fibers obtained for patients P2, P5 and P8 in Figure 3.7.

(a) Patient P2   (b) Patient P5   (c) Patient P8
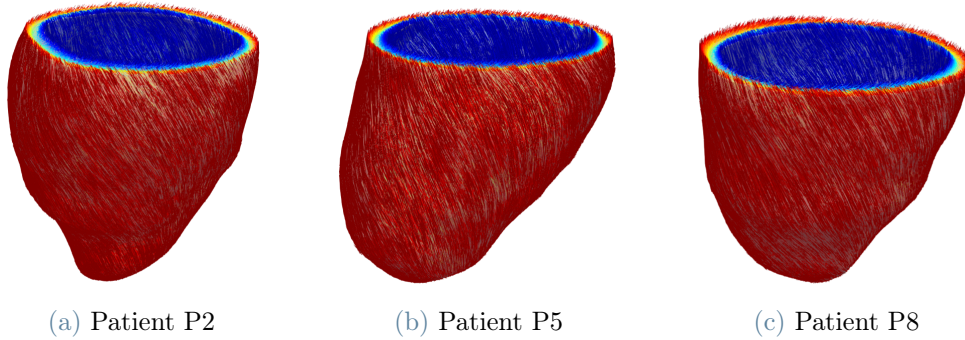
Figure 3.7: Reconstructed fibers obtained with rule-based BT algorithm, with boundary values $\alpha_{\mathrm{epi}} = -60°$, $\alpha_{\mathrm{endo}} = 60°$, $\beta_{\mathrm{epi}} = 20°$, $\beta_{\mathrm{endo}} = -20°$ as in [115].

Concerning instead the preliminary solution of the Eikonal equation (2.1), the range of the resulting activation times is compared with the timings of the electrical data acquired at the epicardial veins, so that the values of conductivities can be adjusted to diminish the discrepancy. In particular, they varied by the same factor in the three directions and, whenever needed, also the velocity of depolarization c_0 and the dimensionless parameter ε can be touched.

In general, increasing the conductivities results in smaller activation times, hence leading to a faster electrical propagation in the LV. The same effect is obtained when c_0 is increased and/or ε is lowered. In the fibrotic cases, also the degree of fibrosis z plays a role and its value is set during the preprocessing procedure mentioned in Section 2.3.4. A higher value of z entails higher conductivities in the scar tissue, leading again to a faster conduction in those regions. Although radiologists from Hospital of S. Maria del Carmine were able to detect a degree of fibrosis greater than 50% for patients P5 and P8, a more precise value had to be estimated during the calibration procedure, together with the other five parameters.

Concerning our patients, the range of activation times to be matched simulating the Eikonal model are reported in Table 3.2 and graphically represented in Figure 3.5.

	$N_{\mathbf{AT}}$	$\mathbf{minAT}\ [s]$	$\mathbf{maxAT}\ [s]$
P2	41	0.068	0.122
P5	36	0.045	0.127
P8	15	0.062	0.142

Table 3.2: Range of ATs for P2, P5 and P8, taken from [113]. N_{AT} represents the number of recorded ATs for each patient.

We define, as in [114], the relative error between computational and measured activation times, denoted by τ_j^h and τ_j^{clin}, respectively:

$$e = \frac{1}{N_{\mathrm{AT}}} \sum_{j=1}^{N_{\mathrm{AT}}} \frac{\tau_j^{\mathrm{clin}} - \tau_j^h}{\max_{i \in \{1,\ldots,N_{\mathrm{AT}}\}} \tau_i^{\mathrm{clin}}}. \tag{3.1}$$

Results of the calibration

The final values of Eikonal model parameters adjusted to match the activation times in Table 3.2, are reported below in Table 3.3, together with the computed relative errors (3.1) for each patient.

	$\hat{\sigma}_f$ $[m^2 s^{-1}]$	$\hat{\sigma}_s$ $[m^2 s^{-1}]$	$\hat{\sigma}_n$ $[m^2 s^{-1}]$	$\mathbf{c_0}$ $[s^{-\frac{1}{2}}]$	ε	z	e $[\%]$
P2	$0.2293 \cdot 10^{-3}$	$0.1048 \cdot 10^{-3}$	$0.3375 \cdot 10^{-4}$	84.367179	11.960212	1.0	3.99
P5	$0.8025 \cdot 10^{-4}$	$0.3669 \cdot 10^{-4}$	$0.1181 \cdot 10^{-4}$	86.568062	8.947733	0.6	4.51
P8	$0.1911 \cdot 10^{-3}$	$0.8735 \cdot 10^{-4}$	$0.2813 \cdot 10^{-4}$	80.699041	14.9502645	0.7	9.89

Table 3.3: Calibrated parameters of the Eikonal model and relative errors for patients P2, P5 and P8.

We notice immediately that the relative errors for P2 and P5 are much smaller than the error obtained for P8. However, an error below 10% is considered acceptable for our purposes, since we are not focusing only on the modelling of electrophysiology. Indeed, approaching the electromechanical simulations with ERM model in Section 3.3, the accuracy of the electrical calibration will not affect much the mechanic outcomes.

The calibrated activation maps are reported in Figure 3.8, obtained post-processing the solutions with the Paraview software.

(a) Patient P2　　(b) Patient P5　　(c) Patient P8
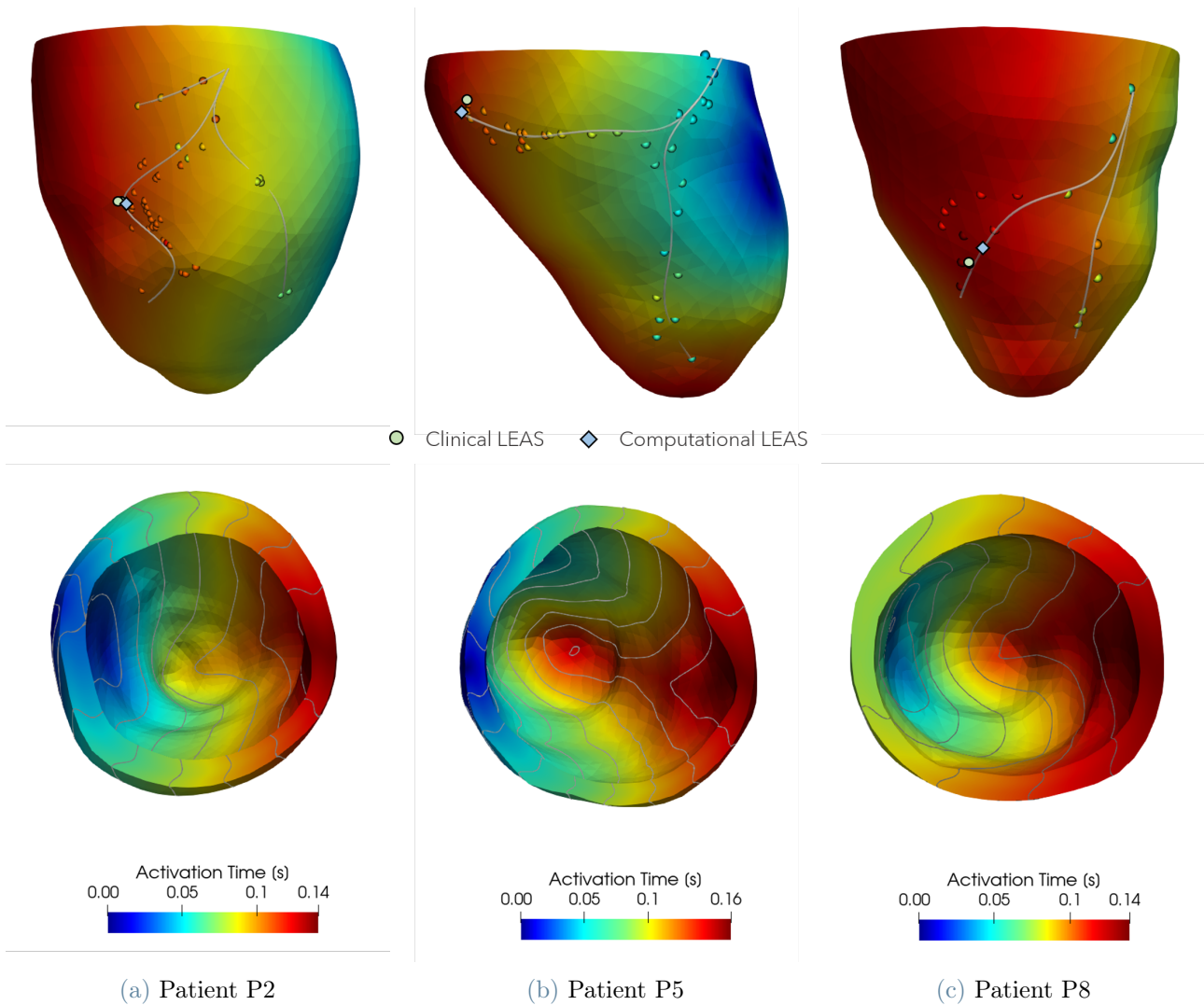
Figure 3.8: *Top figures:* calibrated Eikonal solution compared against clinical electrical data represented as bullets. Clinically measured and computational LEAS are identified along the reconstructed epicardial veins. *Bottom figures:* base point of view of the activation maps with contour lines resulting from the calibration.

We observe an accordance between the qualitative behavior of the Eikonal numerical solutions and the relative errors in Table 3.3. Indeed, for patient P2 the computational ATs are the closest to the clinical ones. Patient P5 is also pretty qualitatively accurate, besides the most apical points, while the electrical data of P8 are the most difficult to be reproduced. A possible reason of the mismatch between simulations and clinical measurements may be the presence of fibrotic regions where some of the data are recorded, both for apical points of P5 and almost half of the points of P8 (see Figures 3.6b and 3.6c). Considering the same degree of fibrosis in the whole reconstructed fibrotic regions

might be a limitation, because there could be some areas where the electrical conduction is slowed down more than in others, for instance in the apical region of P5.

These simulations describe a pre-CRT scenario, reproducing the LBBB behavior of the patients. In view of CRT simulations (treated in Chapter 4), the location of computational LEAS is a useful information that can be retrieved from the solution of the calibrated Eikonal model, as it was done in [113, 131]. In Figure 3.8 we show also the position of the clinically measured LEAS, chosen as the electrical datum with highest activation time, together with the computational LEAS, identified as the mesh point with highest simulated AT with respect to all the points lying on the reconstructed coronary veins.

3.2.3. Final remarks

In the present work, we used all the available electrical data for calibration and prediction of the computational LEAS. This choice was made relying on the fact that a cross-validation test had been already carried out for our patients' datasets in [114] for the monodomain and in [131] for the Eikonal model. In particular, the epicardial veins data were divided in two datasets based on the activation time. More proximal points (with lower ATs) were used to calibrate the model, while more distal data (with higher ATs) served as validation dataset to assess the accuracy of the calibration method. This investigation showed that using only proximal data at the CS led to errors that were comparable to those obtained when using all available clinical data. This kind of discovery may be useful in the future for cardiologists to shorten the acquisition procedure and make it less invasive for the patients, since a smaller number of measurements would be required, maybe facilitating also the CRT implantation procedure.

Concerning CRT simulations that will be addressed in Chapter 4, the acute results of electrical propagation in a LV which is paced by a CRT device will be reproduced with the Eikonal model that was calibrated in this Chapter, modifying only the input datum ψ_a. Indeed, the electrical properties of the myocardial tissue are assumed to remain the same immediately after CRT implant.

To conclude, we mention some technical details about the computational environment used to run Eikonal simulations. The numerical simulations were carried out using the HPC resource at MOX Laboratory, Politecnico di Milano. They were run on 20 Intel Xeon E5-2640 v4 CPUs (cluster Gigat) for the non-fibrotic patient P2, and either on 32 Intel Xeon E5-4610 (cluster Gigatlong, small) or 32 Intel Xeon Gold 6238 v2 CPUs (cluster Gigatlong, big) for patients P5 and P8 with fibrosis. Each Eikonal simulation took $\sim$ 5 minutes, including the preliminary mesh creation and fibers generation steps.

For every patient, up to 10 simulations were needed to obtained the final calibrated scenario. Patients P5 and P8 required more efforts due to the additional value of degree of fibrosis to be adjusted. The pre-processing strategy for the interpolation of the 3D fibrosis distribution on the fine mesh was run on 32 Intel Xeon E5-4610 CPUs (cluster Gigatlong, small) and took ~ 7 minutes for each simulated degree of fibrosis.

3.3.   Mechanics and 0D Hemodynamics Calibration

Once the Eikonal model is properly calibrated, the same logic used for the electrical calibration is applied to the active/passive mechanics coupled to the 0D model for blood circulation, in order to obtain a global patient-specific electromechanics simulation.

We recall that the coupled ERM problem includes the solution of the Reaction problem (2.5) after the Eikonal model is solved, in order to retrieve the calcium ions concentration $[Ca^{2+}]_i$ needed for the active force generation. The 0D formulation (2.8) of this intermediate problem was solved off-line in [115] once and for all, its solution took $\sim 400\ s$ on a single core and it was not personalized on the patient. Indeed, the same 0D calcium concentration $[Ca^{2+}]_{0D,i}$, solution of (2.33), is given as input to the ERM code for each patient-specific simulation. It is then evaluated on each mesh point and interpolated in time to adapt to the time discretization of the mechanical activation problem (2.11).

Concerning the calibration of the coupled mechanics/hemodynamics problem, we use patient-specific data of LV volumes, coming from MRI measurements, and pressure recordings. In particular we have the following available quantities:

- *Diastolic pressure*, P_{AVO}, corresponding to the value of pressure reached in correspondance of the aortic valve opening (see Section 1.1.2). This quantity is used as *input datum* for the model.

- *Systolic pressure*, P_{AVC}, corresponding to the value of pressure reached when the aortic valve closes (see Section 1.1.2). It has to be matched by the calibrated ERM model.

- *End Diastolic Volume*, EDV, which is the constant value of volume maintained by the LV during the phase of isovolumetric contraction. It has a twofold function, because it is used to estimate the initial value of a model parameter, which is then adjusted to match the measured EDV itself. This will become more clear in Section 3.3.2.

- *End Systolic Volume*, ESV, which is the value of LV volume characterizing the isovolumetric relaxation phase. Like the systolic pressure, this quantity is matched

during calibration.

Before going to the patient-specific electromechanics, we describe the ERM parameters that will be kept fixed and those that will be modified during the calibration procedure. This is done addressing the ERM model settings for Zygote LV [1] retrieved from [115].

3.3.1. Default Mechanics and Hemodynamics parameters

The mechanics/hemodynamics coupled problem is characterized by a greater number of parameters with respect to the electrophysiology model. We can distinguish between two sets of physical quantities, one for the active force generation model *RDQ20-MF* (2.11) and another one for the finite elasticity equation describing the active/passive mechanics problem (2.14) coupled to the 0D circulation model for boundary conditions (BCs) at the LV base and endocardium.

From ERM simulations on Zygote Solid 3D heart [1], performed in [115], we retrieve the initial setting to run our patient-specific simulations. Regarding mechanical activation, the values were retrieved from [101] and are reported in Table 3.4:

Mechanical activation	$a_{\mathbf{XB}}$ $[MPa]$	SL_0 $[\mu m]$	$\bar{k}_d$ $[\mu M]$	α_{k_d} $[\mu M\ \mu m^{-1}]$	γ
	$1.6 \cdot 10^2$	2.2	0.4	-0.2083	30
	$k_{\mathbf{off}}$ $[s^{-1}]$	$k_{\mathbf{basic}}$ $[s^{-1}]$	$\mu^0_{f_{\mathcal{P}}}$ $[s^{-1}]$	$\mu^1_{f_{\mathcal{P}}}$ $[s^{-1}]$	
	40	8	32.255	0.768	

Table 3.4: Reference parameters of the active force generation model RDQ20-MF for Zygote LV, taken from [101, 115].

All of the listed parameters will be kept unchanged in our simulations, except for the *cross-bridge stiffness* a_{XB} which is physically interpreted as a quantification of the myocardial tissue contractility.

Concerning the active/passive mechanics, besides the parameters of Guccione constitutive law [51] for the passive part of Piola-Kirkhhoff stress tensor (2.15), the main physical quantities are reported in Table 3.5 for the BCs at pericardium (2.14b), where values for (2.16) are derived from [93], and for the BCs at base (2.14d) and endocardium (2.14c) where parameters of the 0D circulation need to be set, i. e. those of the Windkessel lumped parameter model [134].

Pericardium	$K_\perp^{\textbf{epi}}$	$K_\parallel^{\textbf{epi}}$	$C_\perp^{\textbf{epi}}$	$C_\parallel^{\textbf{epi}}$		
	$[Pa\ m^{-1}]$	$[Pa\ m^{-1}]$	$[Pa\ s\ m^{-1}]$	$[Pa\ s\ m^{-1}]$		
	$2\cdot10^5$	$2\cdot10^4$	$2\cdot10^4$	$2\cdot10^3$		
Windkessel	$\bar{p}_{\textbf{AVO}}^{\textbf{0D}}$	$\bar{p}_{\textbf{MVO}}^{\textbf{0D}}$	$\bar{p}_{\textbf{ED}}^{\textbf{0D}}$	C	R	EDV_{init}
	$[mmHg]$	$[mmHg]$	$[mmHg]$	$[Pa^{-1}\ m^3]$	$[Pa\ s\ m^{-3}]$	$[mL]$
	83	5	10	$4.5\cdot10^{-9}$	$5\cdot10^7$	120

Table 3.5: Reference parameters of the active/passive mechanics for pericardium BC and 0D Windkessel model employed in [115] for Zygote LV.

In this second set of parameters, the values of $\bar{p}_{\text{AVO}}^{0D}$, *total peripheral resistance* R and EDV_{init} will be modified to match clinical data.

Another parameter that could be set using the patient's cardiac frequency is the heartbeat period. However, in our work it will be fixed at $0.8\ s$ for all three patients, due to the lack of such clinical datum.

In order to reach convergence of the ERM solution to a limit cycle, at least two heartbeats need to be simulated, as it was shown with tests carried out by [115] (see Figure 3.9).
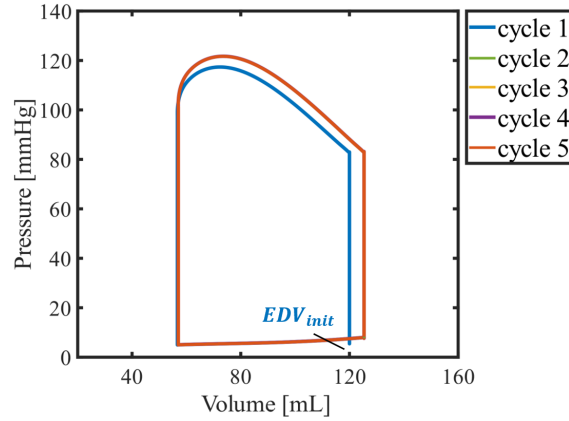
Figure 3.9: Reference PV-loop resulting from Zygote ERM simulation of 5 cardiac cycles (taken from [115]).

In conclusion, regarding time discretization, we will stick with the time-steps used to test the ERM model on Zygote in [115], $\Delta t = 10^{-4}\ s$ for the global problem and a finer $\Delta t = 2.5\cdot10^{-5}\ s$ for the advancement of the activation problem (2.38) at each global time-step (see Section 2.2.3).

3.3.2.   Patient-specific Eikonal-Reaction-Mechanics simulations

Starting from the reference mechanical parameters reported in Tables 3.4 and 3.5, we can calibrate the ERM model in order to describe the pre-operative LBBB-like dyssynchronous electromechanical behavior of patients P2, P5 and P8. The idea is to estimate some of the model parameters so that the clinically measured volumes and pressures can be reproduced. In particular, ERM simulations will be run for each patient varying the following physical quantities:

- Crossbridge stiffness a_{XB} mainly to match the clinical ESV.

- End diastolic volume of the first simulated cardiac cycle EDV_{init} which is assigned with an inital guess near the clinical EDV. Then, it is adjusted so that the measured EDV itself is reproduced at the second simulated heartbeat when the limit cycle is reached (see Figure 3.9).

- The aortic valve opening pressure $\bar{p}_{AVO}^{0D}$ of the 0D Windkessel model that is set once and for all to be equal to the value of clinical diastolic pressure P_{AVO}.

- Total peripheral resistance R is adjusted principally to match the clinical aortic valve closing (systolic) pressure P_{AVC}.
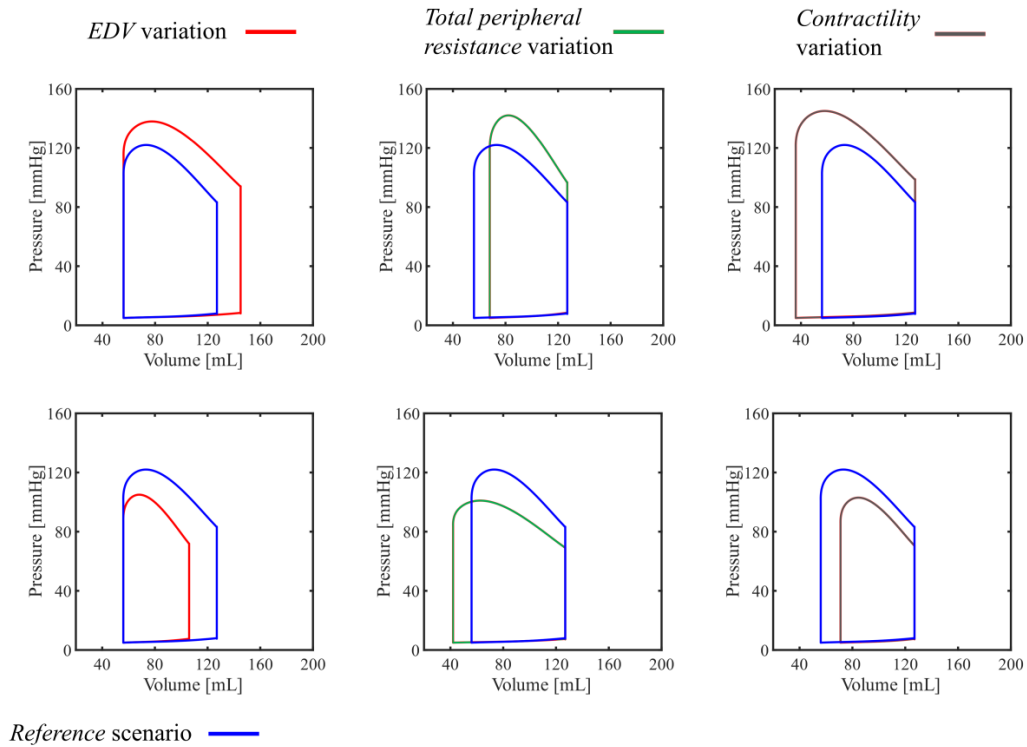
Figure 3.10: PV-loops variations increasing (top) or decreasing (bottom) the reference parameters EDV_{init}, R or a_{XB} (image taken from [115]).

In Figure 3.10 we report the result of a sensitivity analysis carried out in [115], evaluating the effects of varying the aforementioned parameters in ERM simulations for Zygote LV, in particular on PV-loops, where the blue plot represents the reference scenario with quantities given in Section 3.3.1. When the value of EDV_{init} is increased, the consequence is an increase of the maximum pressure reached during a cardiac cycle, together with higher ejection fraction (EF) and stroke volume (SV). An increment of the resistance R also results in higher maximum pressure needed to eject blood from the LV, but it also increases ESV, determining lower SV and EF. Concerning the contractility a_{XB}, if its value is increased the chamber will be able to collect more blood and to eject a larger amount of it. Hence, SV and EF will assume higher values, while ESV will become smaller.

The clinically measured mechanical data for patients P2, P5 and P8 provided by the Hospital of S. Maria del Carmine in Rovereto (TN), Italy, are reported in Table 3.6:

	ESV	**EDV**	**SV**	**EF**	$P_{\mathbf{AVO}}$	$P_{\mathbf{AVC}}$
	$[mL]$	$[mL]$	$[mL]$	$[\%]$	$[mmHg]$	$[mmHg]$
P2	425	501	76	15.2	60	110
P5	215	294	80	27.0	*Not available*	*Not available*
P8	143	214	71	33.3	70	130

Table 3.6: Clinical mechanical data of volumes and pressures for patients P2, P5 and P8, obtained from Hospital of S. Maria del Carmine in Rovereto (TN), Italy.

We notice that pressure measurements for P5 are lacking. Hence, for patient P5 we will only focus on reproducing the correct values of ESV and EDV.

A preliminary mechanical calibration for patients P5 and P8 was made in [113], but their fibrosis distributions were not taken into account, as well as pressure data of P8. Therefore, in the present work we propose the first complete ERM calibration for all three patients.

For patients P2 and P8, the input datum of P_{AVO} from Table 3.6 is assinged to the model parameter $\bar{p}_{\mathrm{AVO}}^{0D}$, while for P5 we use the default value reported in Table 3.5. Then, several ERM simulations are performed with the code implemented in the life$^{\mathsf{x}}$ library, using as computational domains for the mechanics the coarse meshes of Figure 3.3 and modifying the three mechanical parameters based on the analysis of their variations represented in Figure 3.10, until the exact values of volumes and P_{AVC} (not for P5) are reached. Concerning the electrical component included in the ERM code, the calibrated

parameters for the Eikonal model reported in Table 3.3 are employed.

Results of the mechanical calibration

The final mechanical parameters to be set in the ERM code in order to obtain calibrated electromechanical simulations for the three patients are reported in Table 3.7.

	$\bar{p}_{\text{AVO}}^{0D}$ $[mmHg]$	EDV_{init} $[mL]$	R $[Pa\ s\ m^{-3}]$	a_{XB} $[MPa]$
P2	60	464	$3.5 \cdot 10^7$	$5.2 \cdot 10^2$
P5	83*	284	$8 \cdot 10^7$	$7.6 \cdot 10^2$
P8	70	215	$6.3 \cdot 10^7$	$3.2 \cdot 10^2$

Table 3.7: Calibrated mechanical parameters of the ERM model for patients P2, P5 and P8. The * symbol indicates that $\bar{p}_{\text{AVO}}^{0D}$ remains equal to the reference parameter of Table 3.5.

The resulting PV-loops are plotted with MATLAB and they are represented in Figure 3.11, in which we report the values of EDV, ESV, SV, EF and $P_{\max}$ retrieved from the ERM numerical solution. Moreover, also $dP/dt|_{\max}$ is computed since it will turn out to be useful when dealing with CRT simulations in Chapter 4.

(a) Patient P2   (b) Patient P5   (c) Patient P8
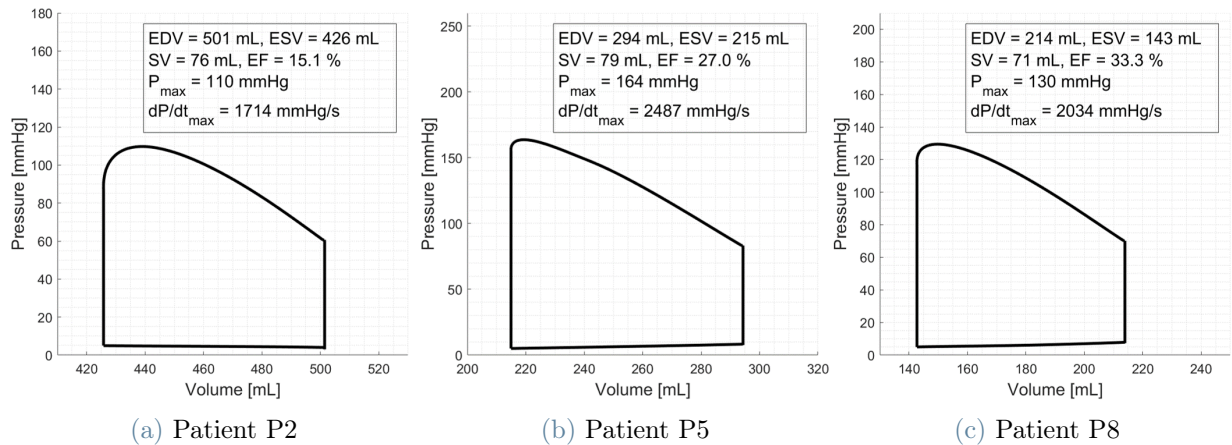
Figure 3.11: PV-loops obtained after calibration of the ERM model for patients P2, P5 and P8, corresponding to the second simulated heartbeat in which the limit cycle is reached.

We can observe that for all three patients the clinically measured quantities are perfectly matched by the ERM simulations, as we sum up in Table 3.8:

	Data	ESV [mL]	EDV [mL]	SV [mL]	EF [%]	$P_{\text{AVO}}/\bar{p}_{\text{AVO}}^{0D}$ [mmHg]	$P_{\text{AVC}}/P_{\text{max}}$ [mmHg]
P2	*Clinical*	425	501	76	15.2	60	110
	Simulated	426	501	76	15.1	60	110
P5	*Clinical*	215	294	80	27.0	–	–
	Simulated	215	294	79	27.0	83	164
P8	*Clinical*	143	214	71	33.3	70	130
	Simulated	143	214	71	33.3	70	130

Table 3.8: Comparison between clinical and computational mechanical data of volumes and pressures for patients P2, P5 and P8.

We approximated the systolic pressure P_{AVC} with the computational value of maximum pressure P_{max} during a cardiac cycle. The lack of pressure data for P5 leads to very high non-physiological values of the simulated $P_{\text{max}} = 164\ mmHg$, as one can see in Table 3.8. This behavior could be adjusted going on in the model parameters calibration so that pressure values can be rearranged to physiological ranges.

Concerning the maximum rate of LV pressure change $dP/dt|_{\text{max}}$ reported in Figure 3.11, it is a surrogate for contractility as mentioned in Section 1.2.3 of Chapter 1. Its computational value is higher for P5, influenced by the extremely large P_{max}, and lower for P2 and it may be reflected in the mechanical behavior addressed below (Figure 3.12): whenever $dP/dt|_{\text{max}}$ is higher, then also the displacement has larger peaks.

The computed displacement $\boldsymbol{d}$, solution of the Finite Elasticity equation (2.14) is reported in Figure 3.12 for patients P2, P5 and P8. In particular, its temporal evolution in the LV myocardium during a cardiac cycle, from time $t = 0\ s$ to $t = 0.8\ s$, is showed by frames taken at different time instants, using the Paraview software for the visualization of the ERM simulation outputs. Concerning P5 in Figure 3.12b, we report the time instant $t = 0.3\ s$ to better highlight the ventricular dyssynchrony (VD), which is more evident compared to P2 (Figure 3.12a) when looking to the respective values of maximum displacement. This may be due to the presence of fibrotic tissue in P5, indeed, the highest non-homogeneous displacements (coloured in yellow and red in Figure 3.12b) occur in regions of the LV that were targeted with fibrosis. The same happens for P8 in Figure 3.12c.

(a) Patient P2

(b) Patient P5

(c) Patient P8
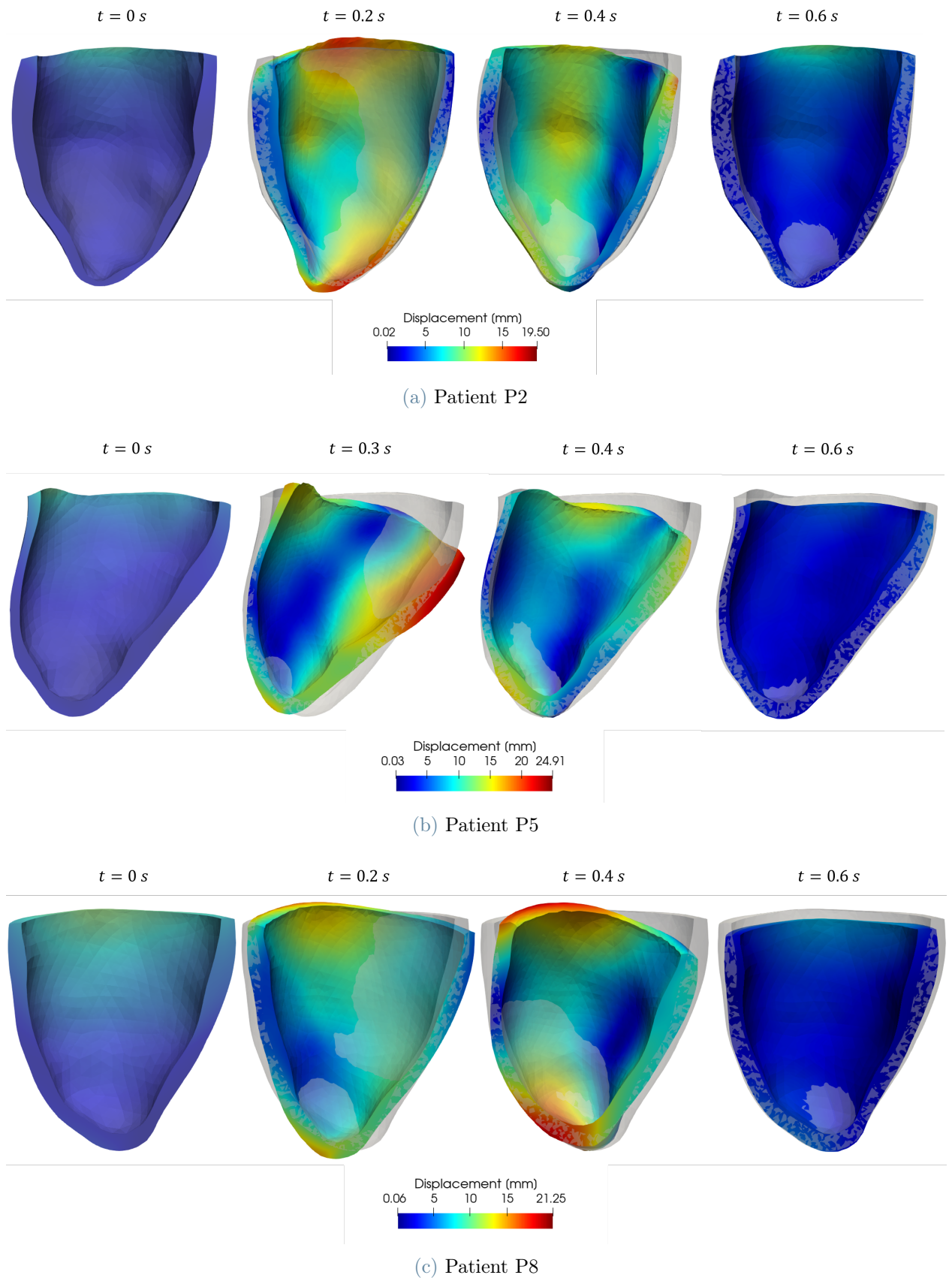
Figure 3.12: Pre-CRT dyssynchronous behavior of the myocardial displacement **d**, solution of the calibrated mechanics problem, in the truncated LVs anterior portions during a cardiac cycle.

3.3.3. Final Remarks

All ERM simulations are performed using a time discretization step $\Delta t = 10^{-4}$ s, setting a final time for the temporal loop $T = 1.6$ s, in order to simulate two cardiac cycles with duration of 0.8 s. The results reported in Section 3.3.2 above refer to the second heartbeat, in which the limit cycle is attained.

The numerical simulations are obtained with the ERM code implemented in the `life`^{x} library (`https://lifex.gitlab.io/lifex`) and they were run using the HPC resource at MOX Laboratory, Politecnico di Milano, either on 32 Intel Xeon E5-4610 (cluster Gigatlong, small) or 32 Intel Xeon Gold 6238 v2 CPUs (cluster Gigatlong, big). Each ERM simulation took $\sim 7-8$ hours. For patient P2, 15 simulations were needed to obtain calibration of the ERM model, while 10 and 6 were enough for P5 and P8, respectively.

In Figure 3.13 we collect all clinical data that were provided from the Hospital of S. Maria del Carmine in Rovereto (TN), Italy, and all the parameters of electrophysiology, mechanical activation and Windkessel model that we adjusted to obtain calibration.

Figure 3.13: Summary of the modified parameters of each compartment of the ERM model to match the corresponding clinical measured data.

The patient-specific ERM models obtained in this Chapter represent the so-called *pre-operative* scenario, because they exploit electrical and mechanical data acquired just before the execution of CRT procedure, thus reproducing the LV function of patients that have not undergone implantation yet. The numerical results are able to describe the venctricular dyssynchrony of the patients' LVs caused by the LBBB condition and the fibrosis distributions that slow down the conduction velocity in the myocardium. Moreover, the reduced values of EF are also reproduced.

The pathologies of these patients make them candidates for Cardiac Resynchronization Therapy. In next Chapter 4 we will treat the numerical simulations of this procedure, first reproducing the clinical CRT carried out by cardiologists in Rovereto and, subsequently, simulating virtual scenarios imposing different CRT settings. Since we focus on acute outcomes of the procedure, based on clinical evidence it is reasonable to assume that the pre-operative calibrated ERM parameters will remain the same also post-CRT, because electrical and contractile properties and resistances do not change immediately after implantation.

4 | Simulation of Cardiac Resynchronization Therapy

In this Chapter we will show the application to the clinical context of Cardiac Resynchronization Therapy (CRT) of the calibrated Eikonal-Reaction-Mechanics (ERM) models obtained in Chapter 3 for patients P2, P5 and P8. This calibrated model allows to characterize the electromechanics of each patient's left ventricle (LV) in both physiological and pathological conditions. In particular, it has been able to reproduce the *pre-operative* LBBB scenario in Chapter 3 and it is used in the current Chapter to characterize the restored electrical and mechanical synchronized LV behavior of acute post-CRT *virtual* scenarios. Each scenario is evaluated by suitable biomarkers retrieved from the numerical solution of the ERM problem (2.22).

In Section 4.1 we describe the general procedure followed in this thesis to simulate different CRT settings and compare their effects on LV function. Then, in Section 4.1.1 we show the results of the application of the procedure to our patients in order to optimize the acute CRT outcomes with respect to the clinical implantation at the latest electrically activated segment (LEAS). Finally, we will discuss in Section 4.5 the different effects of the therapy depending on the considered patient and draw some conclusions.

4.1. General workflow for simulations of CRT virtual scenarios

The reproduction of a particular Cardiac Resynchronization Therapy scenario uses the same calibration of the ERM model obtained in Chapter 3, which described the pathologic LBBB dyssynchronous activity of the patient's LV before CRT procedure is applied, indicated as *pre-operative* scenario.

The main assumption of the thesis is that the estimated *pre-operative* parameters are considered to remain the same acutely, meaning that the electrical and mechanical properties of the heart muscle and the blood resistances do not change immediately after implantation, since the LV needs over 6 months to reverse remodel [118].

In order to adapt the *pre-operative* model to the CRT context, we need to change the input datum of the Eikonal problem (2.1) that we denoted as ψ_a prescribed on the Dirichlet boundary S_a. Indeed, instead of imposing a septal stimulation using clinically recorded electrical data as in Section 3.2, we identify two points on the epicardium to surrogate the right and left electrodes of the CRT implant (see Section 1.2.1) stimulating the left ventricle:

- The right lead, which is located in the RV apical endocardium in clinical practice, will be positioned on the LV epicardium below the interventricular septum and close to the apex [35].

- The left lead position is set in a point along the reconstructed epicardial veins (see Section 3.1.4).

The timings of initiation of the electrical propagation are given by a chosen inter-ventricular delay, technically named *ventriculo-ventricular delay* (VVD):

$$\text{If VVD} \begin{cases} = 0 & \text{Both stimuli start at } t = 0; \\ > 0 & \text{Right stimulus starts at } t = 0, \text{ left stimulus at } t = \text{VVD}; \\ < 0 & \text{Left stimulus starts at } t = 0, \text{ right stimulus at } t = |\text{VVD}|. \end{cases}$$

The need of simulating patients' LVs undergoing CRT lies on the fact that there is a 30% of non-responders to the procedure as it was explained in the first introductory Chapter at Section 1.2.2.

The idea is to virtually vary the location of left lead along the CS tributaries and the timing settings for VVD in order to identify among different *virtual* scenarios the one corresponding to the best configuration, similarly to [74]. Indeed, several studies in the last two decades demonstrated that LV lead position and VVD programming are key factors for CRT benefits and patients' response [13, 17, 34, 37, 110], (see Section 1.2.4).

More precisely, we are investigating the best CRT settings in terms of acute effects on the patient, meaning that we are simulating and analyzing the post-CRT behavior of the ventricle immediately after the procedure (after few hours or days).

The *optiaml* CRT scenario is determined in this work by computing the most important biomarker used in clinical practice to evaluate acute outcomes of the therapy [108, 141], which is the maximum time derivative of pressure in a cardiac cycle $dP/dt|_{\max}$ [124] occuring during systole: a higher value of pressure change is index of improved contractility and reshynchronization as explained in Section 1.2.3.

Other two parameters that are computed after every CRT simulation are the stroke volume SV and the ejection fraction EF, even if they are indicators of chronic reverse

remodeling after CRT [2, 112, 118] rather than measures of acute outcomes.

For each patient the steps listed below are followed:

1. A first CRT simulation is performed positioning the left lead at the latest electrically activated segment (LEAS), with the aim of reproducing the procedure carried out by cardiologists in Rovereto. The inter-ventricular delay is first set to VVD = 0, denoting the *LEAS-based* CRT scenario.

2. Two additional simulations are run for the *LEAS-based* case setting VVD = 15 *ms* and VVD = 30 *ms*, knowing that in clinical practice VVD is chosen in a similar range of values.

3. Different points (7 − 8 per patient) on the reconstructed epicardial veins are identified as potential left lead locations, that will lead to all the so called CRT *virtual* scenarios.

4. Every selected point is used to run a CRT simulation with VVD = 0.

5. All the simulated *virtual* scenarios are compared and those corresponding to the best values of $dP/dt|_{\max}$ and/or EF are identified.

6. Those points leading to higher values of the biomarkers are further analyzed selecting a range of VVDs going from a minimum of −30 *ms* to a maximum of 60 *ms*, with a step of 10 − 15 *ms*.

7. For every chosen location, CRT simulations are performed varying the VVD in the respective range.

8. The *optimal* scenarios, arising from the best combination of left lead position and VVD setting, are identified.

4.1.1. Patient-specific simulations of CRT

The procedure described above is employed for patient-specific simulations of cardiac resynchronization therapy, on patients P2, P5 and P8, that underwent clinical CRT implantation at the Hospital of S. Maria del Carmine in Rovereto. In particular, the clinical procedure indicates the latest electrically activated segment (LEAS) as position for the left ventricular lead as it is suggested by several trials [75, 138, 140]. However, there are no proofs that guarantee LEAS to be always the optimal choice.

The purpose of our work is to perform a personalized analysis for every patient [38, 41, 67] in order to identify the best pacing site (*optimial* CRT scenario) among *virtual* scenarios obtained generating randomly distributed locations along the patient's epicardial veins,

including also the computational LEAS (leading to the *LEAS-based* scenario), determined with our pre-operative calibrated Eikonal simulation addressed in Section 3.2.2 (Figure 3.8).

4.2.   CRT simulations for Patient P2

Patient P2 is characterized by extremely large values of *EDV* and *ESV* measured by means of MRI, indices of a dilated cardiomyopathy, that entails a highly reduced ejection fraction *EF*. Contrarily to P5 and P8, it is not diagnosed with myocardial fibrosis. Starting from the electromechanical calibration of Chapter 3, we can perform CRT simulations.

4.2.1.   CRT simulation at the Latest Electrically Activated Segment

As reported in the pipeline of Section 4.1, we start performing a CRT simulation of the *LEAS-based* clinical scenario performed by cardiologists. The right ventricular lead is positioned in the apical region of the interventricular septum, while the left lead is located at the LEAS with an inital VVD = 0. Setting such input data in the calibrated Eikonal model produces the solution reported in Figure 4.1:
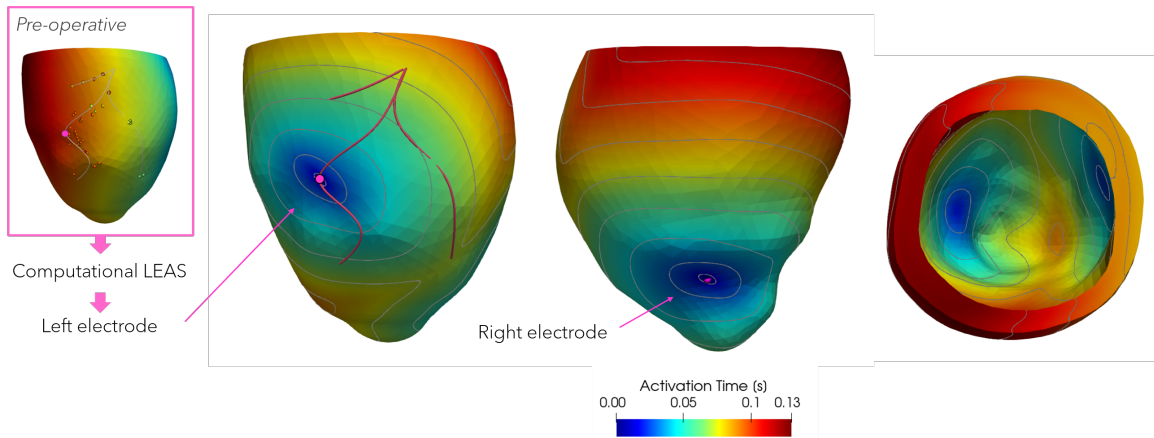
Figure 4.1: Simulated activation map of *LEAS-based* CRT for patient P2. The right electrode stimulus is showed on the left, while the LEAS stimulation is in the central picture. On the right the Eikonal solution is showed from a base point of view.

Then, we run other two simulations with VVD = 15 *ms* and VVD = 30 *ms*, for which the qualitative electrical behavior remains the same.

In Figure 4.2 we present the PV-loops resulting from the three ERM simulations of *LEAS-*

based CRT, compared with the *pre-operative* case and we add also the computational values of $dP/dt|_{\max}$ and EF. We observe that the former increases with higher VVDs, while the latter is increased of $\sim 2\%$ post-CRT but stays almost the same when varying the delay, resulting in *LEAS-based* PV-loops that are practically overlapping.

Figure 4.2: PV-loops comparison for patient P2 among *pre-operative* and *LEAS-based* scenarios with VVDs $= 0, 15, 30 \ ms$. Together with corresponding $dP/dt|_{\max}$ and EF.

4.2.2. Optimization of CRT varying left lead location and delay

After simulating the *LEAS-based* CRT, we choose eight points along the reconstructed epicardial veins, depicted in Figure 4.3.
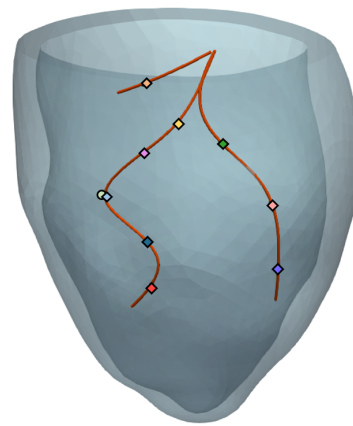
Figure 4.3: Locations of the LV lead for *virtual* CRT scenarios on patient P2. Also the clinical and computational LEAS positions are reported.

Every selected point is used as LV pacing site to run a simulation of a *virtual* CRT scenario, first imposing for every location VVD = 0.

We show the results of each Eikonal simulation in Figure 4.4:
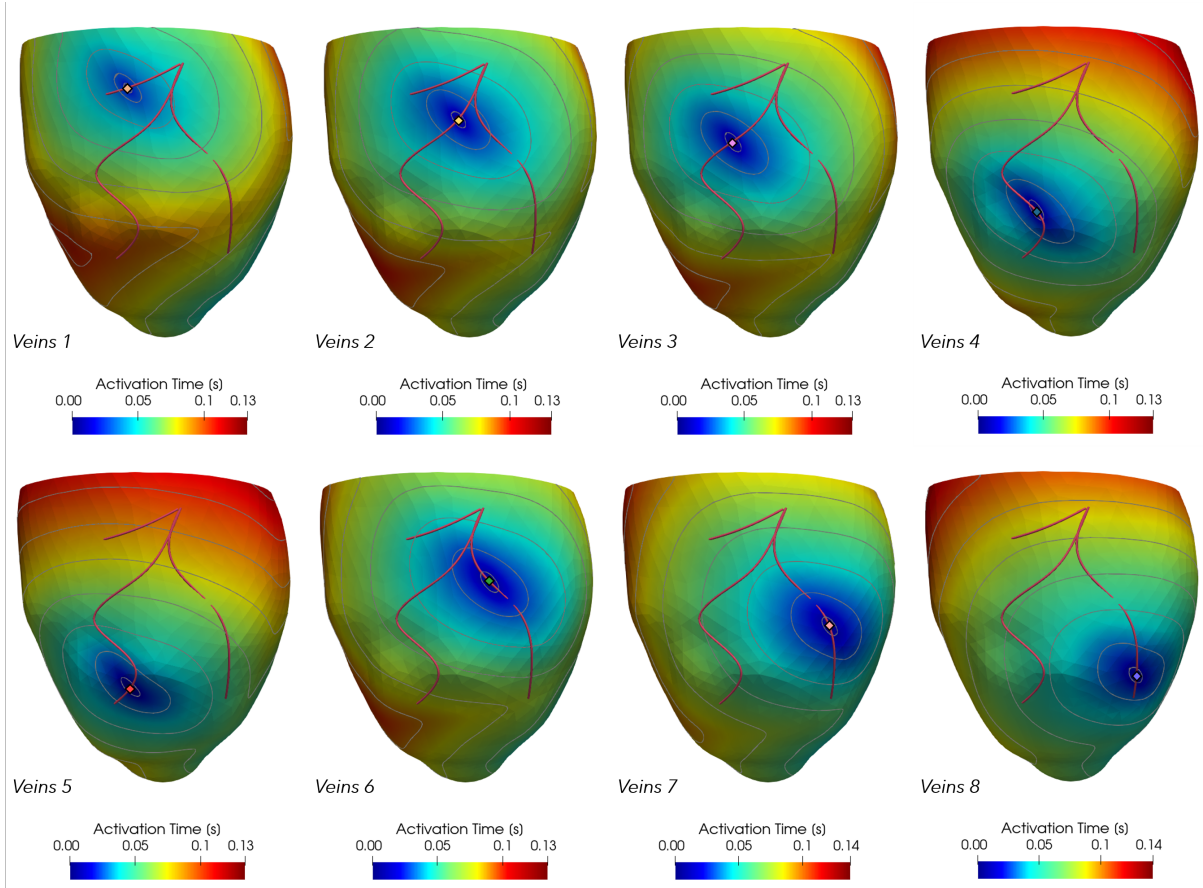
Figure 4.4: Activation maps of patient P2 resulting from Eikonal simulations of *virtual* CRT scenarios with VVD = 0.

Moreover, the plots of the respective PV loops obtained simulating the mechanics are in Figure 4.5, where we report also the corresponding values of $dP/dt|_{\max}$ computed from the numerical pressure solutions.

Comparing the different pressure-volume behaviors, we immediately notice that all *virtual* CRT scenarios lead to higher values of both EF, inferred from wider PV loops, and $dP/dt|_{\max}$, with respect to the *pre-operative* case. Additionally, the maximum rate of pressure change is improved also with respect to the *LEAS-based* scenario in all the *Veins* points.
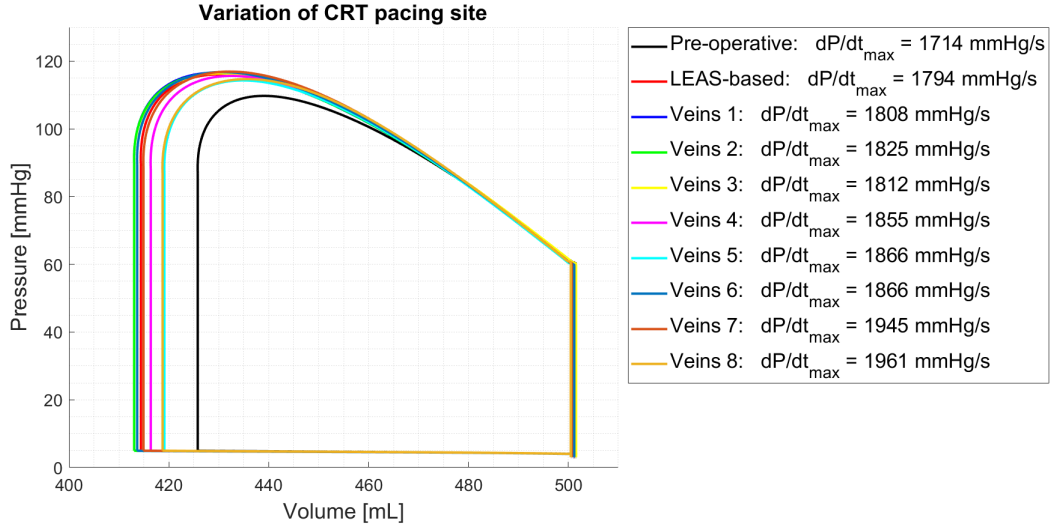
Figure 4.5: PV loops of *virtual* CRT scenarios for patient P2 obtained varying the LV pacing site, keeping VVD = 0. On the right the values of $dP/dt|_{\max}$ are reported.

To go further and analyze VVD variations, we select three among the eight *Veins* locations that correspond to the best improvement of the biomarkers:

- *Veins 2* is the location with highest $dP/dt|_{\max}$ among those with largest EF;

- *Veins 6* entails a further improvement of $dP/dt|_{\max}$ at the expense of a slightly smaller EF;

- *Veins 7* corresponds to the maximal increase of $dP/dt|_{\max}$, keeping an increment of EF around 2%.

We do not go ahead with *Veins 8*, even if it leads to the absolute largest $dP/dt|_{\max}$, because it is located closer to the apex and to the right lead location, position that was discouraged by two large clinical trials [109, 125]. Moreover, the increase in EF is much worse even compared to the *LEAS-based* case. For the three aforementioned locations, we first simulate positive VVDs ranging from 0 to 30 ms, with a step of 10 ms. Then, we analyze also the effect of VVD < 0 for *Veins 6* and *Veins 7*, setting VVD = −10, −20 ms.

The corresponding biomarkers computed after every ERM simulation of all *virtual* CRT scenarios are collected in Table 4.1, where we can identify the optimal configurations of *location-delay* ensuring best acute hemodynamics outcomes in terms of $dP/dt|_{\max}$ and EF, indicated as the *optimal* scenarios:

- *Veins 2* with VVD = 20 ms,

- *Veins 6* with VVD = 20 ms,

- *Veins 7* with VVD $= 10$ *ms*.

Scenario	Delay [ms]	$dP/dt\|_{\max}$ [$mmHg\ s^{-1}$]	$\Delta(dP/dt\|_{\max})$ [$mmHg\ s^{-1}$]	[%]	SV [mL]	Δ(SV) [mL]	[%]	EF [%]	Δ(EF) [%]
Pre-CRT	−	1715	−	−	76.0	−	−	15.2	−
LEAS	0	1794	+79	+4.6	87.0	+11.0	+14.5	17.3	+2.1
	15	1823	+108	+6.3	86.0	+10.0	+13.2	17.3	+2.1
	30	1852	+137	+8.0	85.0	+9.0	+11.8	17.0	+1.8
Veins 1	0	1808	+93	+5.4	88.0	+12.0	+15.8	17.6	+2.4
Veins 2	0	1825	+110	+6.4	88.0	+12.0	+15.8	17.6	+2.4
	10	1869	+154	+9.0	88.0	+12.0	+15.8	17.6	+2.4
	20	1897	+182	+10.6	88.0	+12.0	+15.8	17.5	+2.3
	30	1901	+186	+10.8	87.0	+11.0	+14.5	17.3	+2.1
Veins 3	0	1812	+97	+5.7	88.0	+12.0	+15.8	17.6	+2.4
Veins 4	0	1855	+140	+8.2	85.0	+9.0	+11.8	16.9	+1.7
Veins 5	0	1866	+151	+8.8	82.0	+6.0	+7.9	16.3	+1.1
Veins 6	−20	1759	+44	+2.6	85.0	+9.0	+11.8	16.9	+1.7
	−10	1808	+93	+5.4	86.0	+10.0	+13.2	17.2	+2.0
	0	1866	+151	+8.8	88.0	+12.0	+15.8	17.5	+2.3
	10	1916	+201	+11.7	88.0	+12.0	+15.8	17.5	+2.3
	20	1937	+222	+12.9	87.0	+11.0	+14.5	17.4	+2.2
	30	1934	+219	+12.8	86.0	+10.0	+13.2	17.2	+2.0
Veins 7	−20	1830	+115	+6.7	84.0	+8.0	+10.5	16.8	+1.6
	−10	1891	+176	+10.3	85.0	+9.0	+11.8	17.0	+1.8
	0	1945	+230	+13.4	86.0	+10.0	+13.2	17.2	+2.0
	10	1967	+252	+14.7	86.0	+10.0	+13.2	17.1	+1.9
	20	1961	+246	+14.3	85.0	+9.0	+11.8	16.9	+1.7
	30	1939	+224	+13.1	82.0	+6.0	+7.9	16.3	+1.1
Veins 8	0	1961	+246	+14.3	82.0	+6.0	+7.9	16.3	+1.1

Table 4.1: Biomarkers corresponding to *virtual* CRT configurations for patient P2.

The PV loops of the *optimal* scenarios are reported in Figure 4.6: we observe that maximal

$dP/dt|_{\max}$ is at location *Veins 7* with VVD $= 10\ ms$, even if the respective PV loop is a little narrower, yielding to lower EF, with respect to *Veins 2* and *Veins 6*.
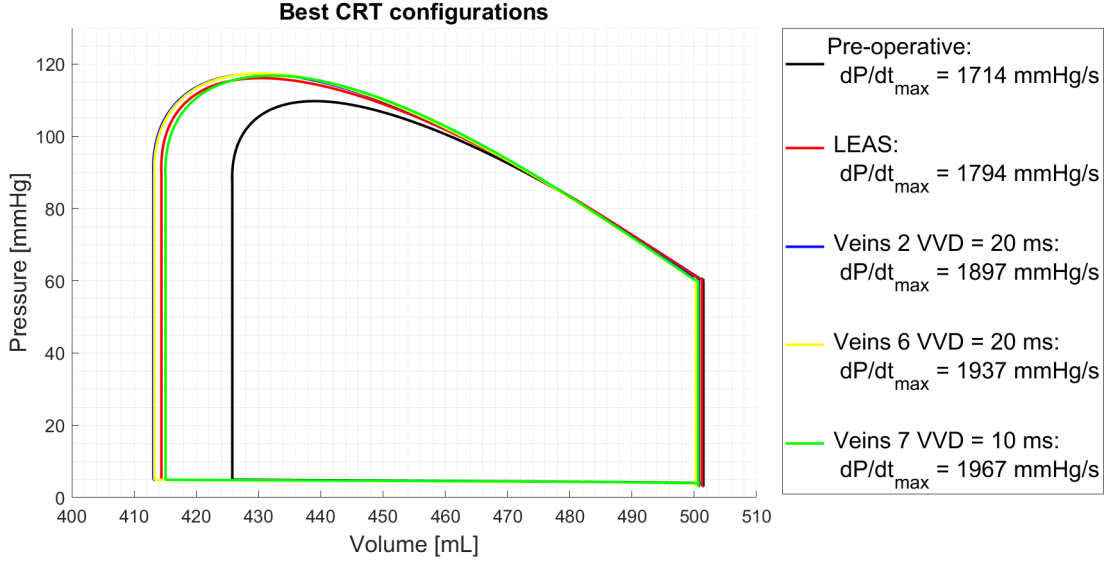

Figure 4.6: PV loops of the *optimal* CRT scenarios for patient P2, obtained varying both the LV pacing site and the VVD. On the right the values of $dP/dt|_{\max}$ are reported.

Commenting on the results of the biomarkers reported in Table 4.1, we can immediately notice that every *virtual* CRT scenario leads to improved values of maximum rate of pressure change $dP/dt|_{\max}$, stroke volume SV and ejection fraction EF, even if we have previously claimed that the last two indices are not suitable to predict acute effects of the procedure. Indeed, although their value slightly improves between pre and post-CRT, it does not encounter great variations between different CRT configurations, hence it does not help identifying the best scenario. Moreover, in this patient-specific case it is better to look at the increment of SV rather than EF, since the latter remains really small ($\Delta EF \sim +2\%$) due to the abnormally large volumes.

Focusing instead on VVD variations, increasing the delay yields to a further improvement of $dP/dt|_{\max}$, until a certain threshold: at *Veins 6* and *7* from VVD $\geq 20\ ms$ the biomarker starts to decrease, while SV and EF follow an opposite trend. Concerning simulations of negative delays, the rate of pressure change immediately decays.

In conclusion, we choose as *optimal* CRT scenario the combination of LV pacing site at *Veins 7* with VVD $= 10\ ms$, for which $\Delta(dP/dt|_{\max}) = +14.7\%$.

Comparison of the qualitative mechanical behaviors

The resulting mechanical behavior of the wall displacement $\boldsymbol{d}$ during a cardiac cycle for *LEAS-based* and *Veins 7* CRT is reported in Figure 4.7 for three intermediate time-steps and it is compared with the *pre-operative* behavior.
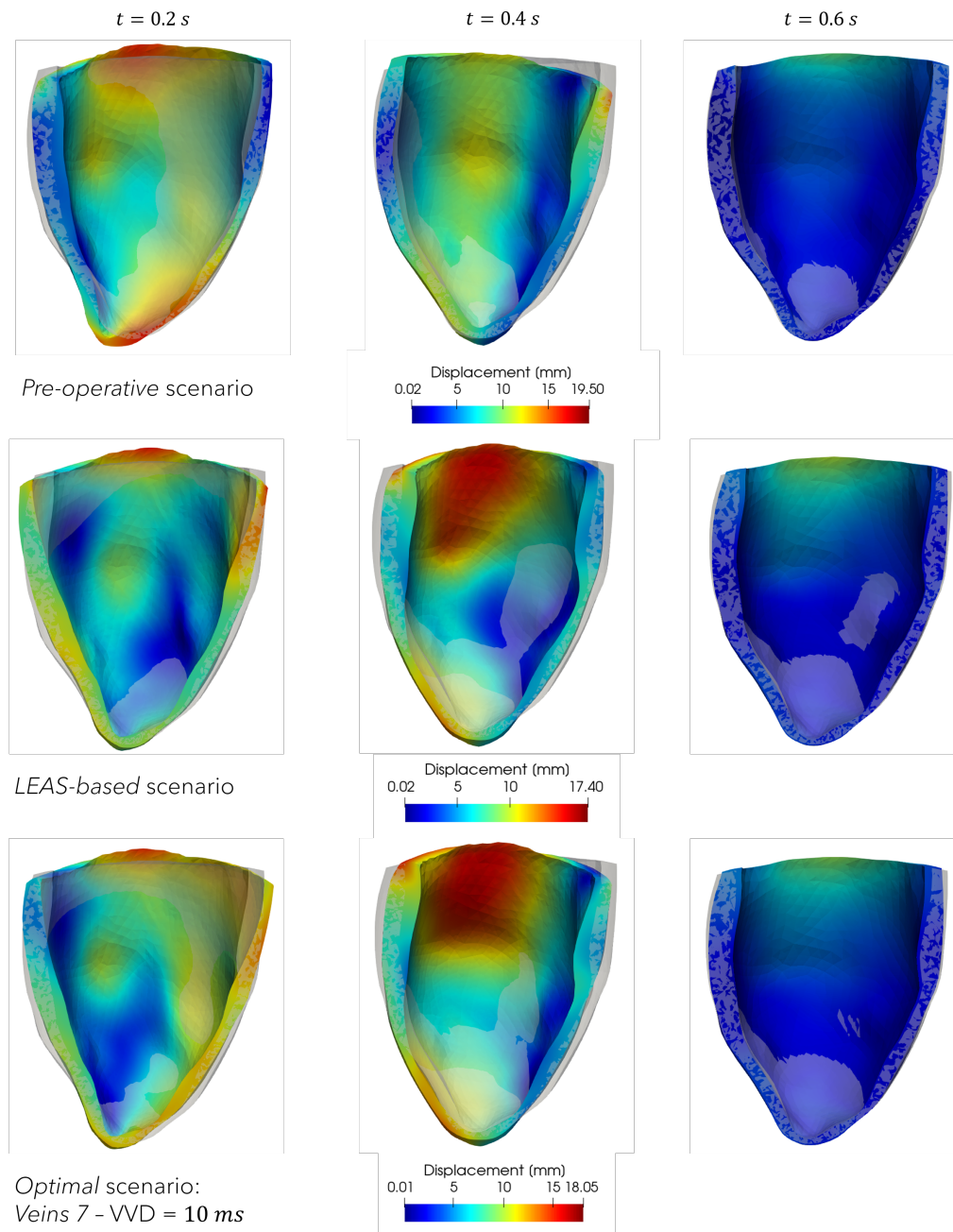
Figure 4.7: Qualitative comparison of displacements $\boldsymbol{d}$ among *pre-operative* (top), *LEAS-based* (middle) and *optimal* (bottom) scenarios, in the anterior portion of the truncated LV of patient P2 during a cardiac cycle.

The two post-CRT mechanical behaviors are qualitatively similar, but for mildly larger displacements in the anterior basal and mid portions of the ventricle for *Veins 7* at time instants $t = 0.2\ s$ and $t = 0.4\ s$. The difference with the *pre-operative* dyssynchronous behavior is evident in both cases, highlighting the ability of the simulated CRT procedure to restore a more coordinated contraction of the LV, especially in the basal area.

4.3. CRT simulations for Patient P5

We can now address the optimization of CRT for patient P5, which is still characterized by an ejection fraction below 30%, even if not as small as P2. Moreover, this patient is also affected by fibrosis, whose distribution along the ventricle is reported in Figure 3.4.

4.3.1. CRT simulation at the Latest Electrically Activated Segment

We first report the results of the simulated *LEAS-based* clinical CRT, setting VVD $= 0$ at the beginning and then VVD $= 15\ ms$ and VVD $= 30\ ms$, to study the influence of delay variations.

In Figure 4.8 we represent the Eikonal numerical solution, where we highlighted also the position of the right electrode.
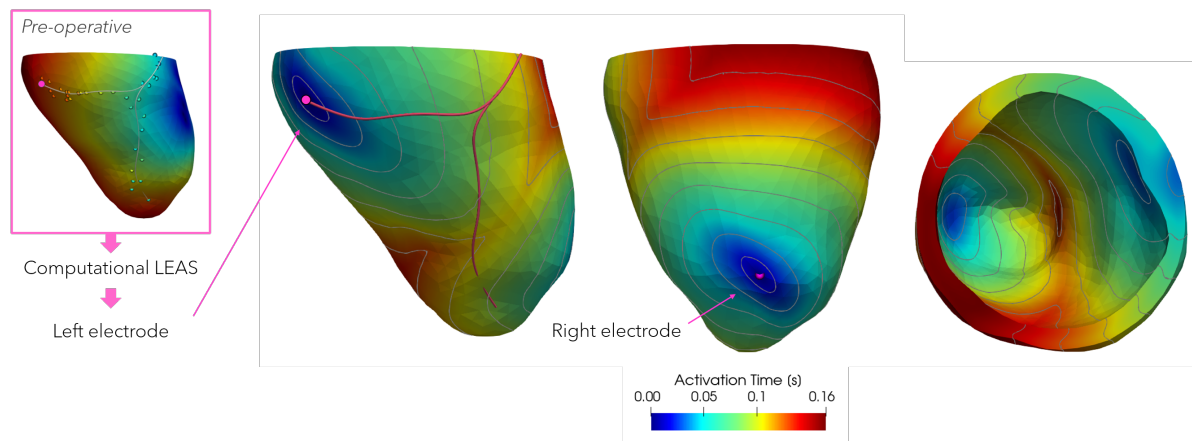
Figure 4.8: Simulated activation map of *LEAS-based* CRT for patient P5. The right electrode stimulus is showed on the left, while the LEAS stimulation is in the central picture. On the right the Eikonal solution is showed from a base point of view.

Additionally, the different pressure-volume behaviors obtained varying VVD are showed with PV loops in Figure 4.9, compared also with the *pre-operative* case, adding the computational values of $dP/dt|_{\max}$ and EF.
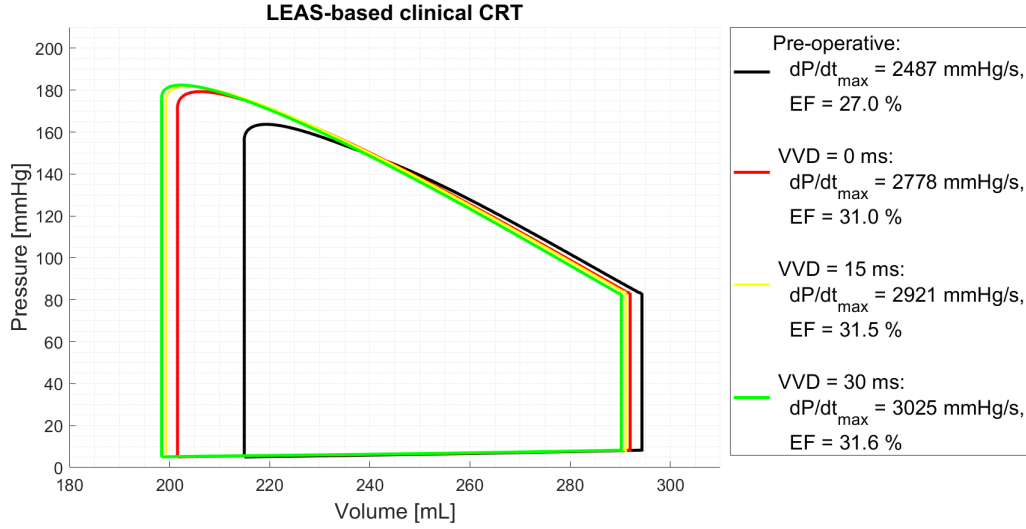
Figure 4.9: PV-loops comparison for patient P5 among *pre-operative* and *LEAS-based* scenarios with VVDs $= 0, 15, 30\ ms$. Together with corresponding $dP/dt|_{\mathrm{max}}$ and EF.

We immediately notice improved $EF > 30\%$, though its value does not change much among the three delay settings, similarly to the P2 case. Most importantly, a substantial increase is observed for $dP/dt|_{\mathrm{max}}$, that is even higher when VVD is higher. Going from $\Delta(dP/dt|_{\mathrm{max}}) = +11.7\%$ at VVD$= 0$, to $\Delta(dP/dt|_{\mathrm{max}}) = +21.6\%$ at VVD$= 30\ ms$ (see Table 4.2).

4.3.2. Optimization of CRT varying left lead location and delay

For patient P5 we choose seven additional points distributed along the reconstructed epicardial veins to simulate different *virtual* CRT scenarios varying the LV pacing site. Their locations are represented in Figure 4.10, together with the *clinical* and *computational* LEAS. We denoted locations *Veins 5** and *Veins 6**, to indicate that these two points are inside the fibrotic region. The effect of pacing inside scar tissue on CRT outcomes is still uncertain, as we briefly mentioned in Section 1.2.4.

From the maps of activation times (ATs) resulting from Eikonal simulations, reported in Figure 4.11, we observe that pacing at *Veins 5* and *6* entails a larger maximum AT, being index of a slower electrical propagation. Although, also *Veins 3* and *Veins 4* produce higher ATs, with respect to the other remaining locations. Hence, a possible cause of slower conduction may be the proximity to the septal region and to the right pacing site, rather than laying in a fibrotic region.
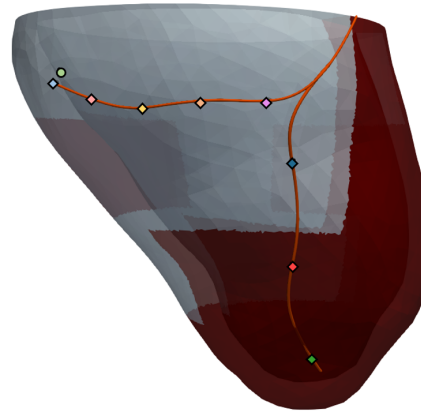
Figure 4.10: Locations of the LV lead for *virtual* CRT scenarios on patient P5. Also the clinical and computational LEAS positions are reported.
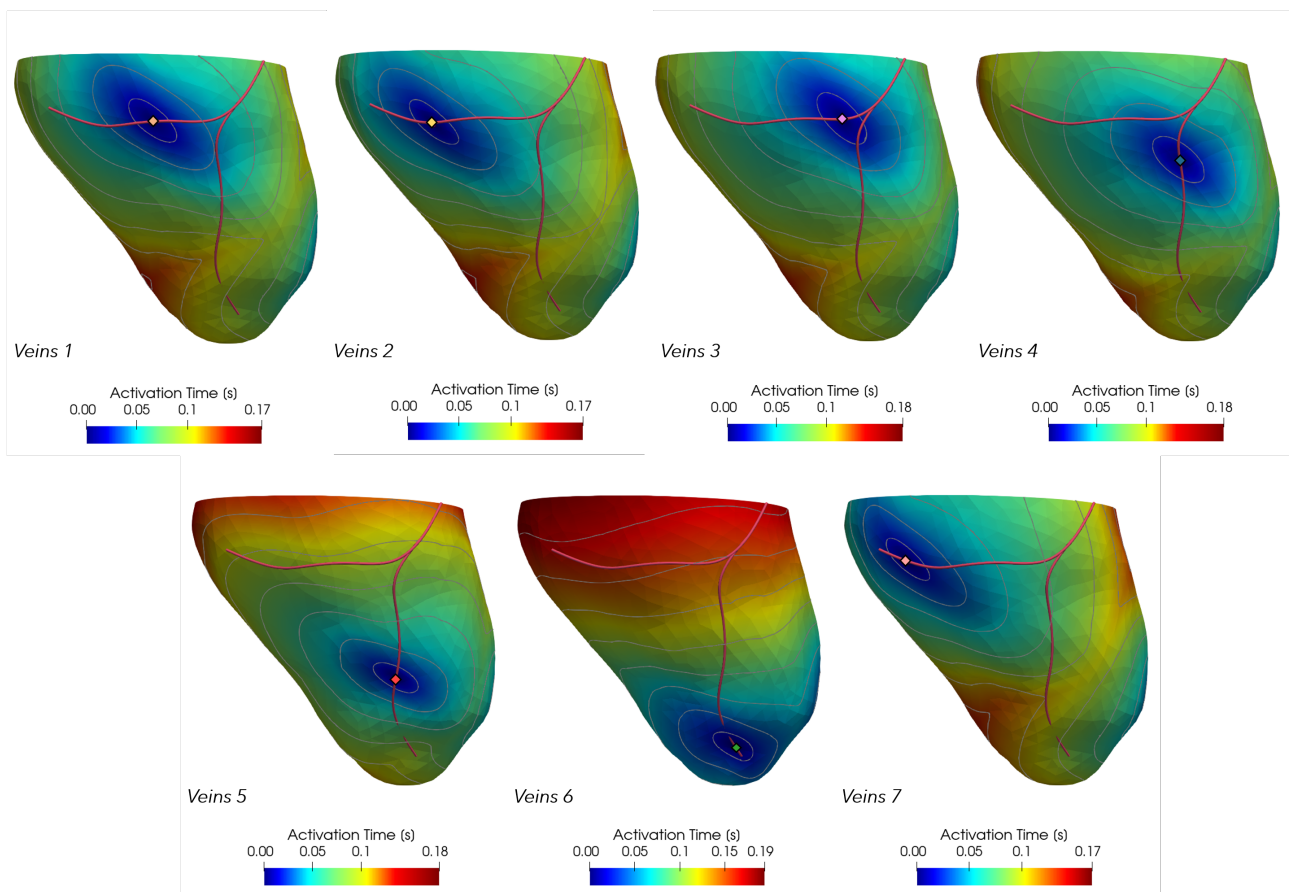
Figure 4.11: Activation maps of patient P5 resulting from Eikonal simulations of *virtual* CRT scenarios with VVD = 0.

The different PV-loops are compared in Figure 4.12, where the computed $dP/dt|_{\max}$ are

associated to each pacing configuration. The maximum rate of pressure change improves in all *virtual* scenarios with respect to the *pre-operative* case. We immediately exclude *Veins 3* and *Veins 4* from the possible optimal locations, because the corresponding $dP/dt|_{\max}$ are worse than the *LEAS-based* case, even if their EF are the highest among all these preliminary simulations. Concerning *Veins 6* location, it corresponds to the largest $dP/dt|_{\max}$ but also to the worst SV and EF, that are descreased also with respect to the *pre-operative* scenario. This location, besides being inside the fibrotic region, which may be a problem, is also really close to the apex.
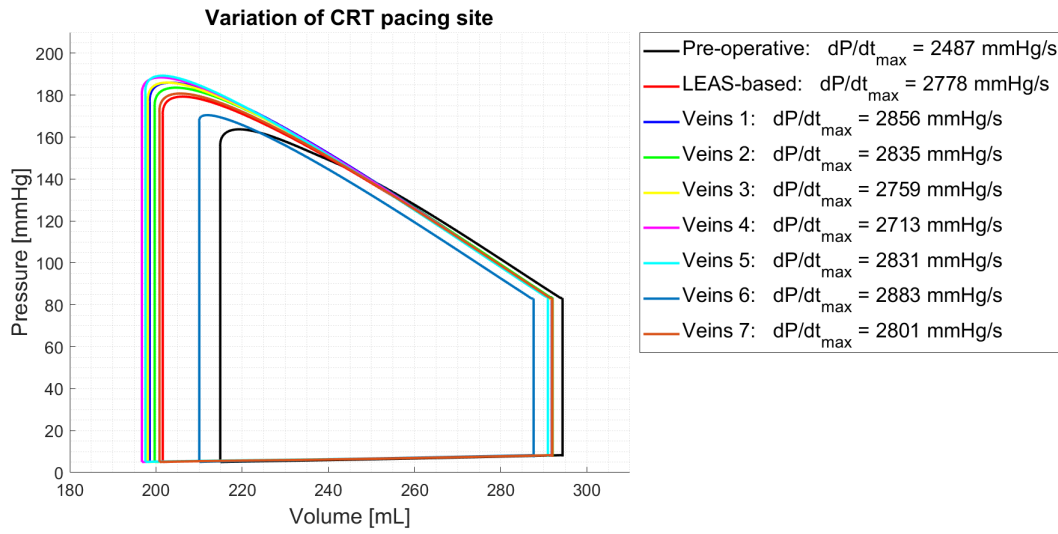
Figure 4.12: PV loops of *virtual* CRT scenarios for patient P5 obtained varying the LV pacing site, keeping VVD = 0. On the right the values of $dP/dt|_{\max}$ are reported.

We remark that all these first simulations reproduce simultaneous right and left stimuli, i. e. VVD = 0 for all locations.

Regarding the VVDs variation analysis, we decide to go on with:

- *Veins 1* that entails the second highest $dP/dt|_{\max}$, ensuring also a good increase in ejection fraction ($\Delta EF = 5.0\%$).

- *Veins 2* for an analogous reasoning.

We decide to disregard *Veins 5* to avoid pacing in scar regions and *Veins 7* because, apart from the lower value of maximum pressure change, it is closer to LEAS, hence the CRT outcomes might be similar.

For *Veins 1* and *Veins 2* we vary the delay, setting the same used for the *LEAS-based* case: VVD = 15 ms and VVD = 30 ms. Since $dP/dt|_{\max}$ keeps increasing for both locations, we go on with even higher delays, until VVD = 60 ms, with a step of 10 ms.

We choose to stop at 60 ms since it is the maximum value usually imposed by clinicians. Moreover, we analyse also the effect of VVD $= -15\ ms, -30\ ms$ for *Veins 1* location. A summary of computational biomarkers resulting from every *virtual* CRT configuration is in Table 4.2.

Scenario	Delay	$dP/dt\|_{\max}$	$\Delta(dP/dt\|_{\max})$		SV	Δ(SV)		EF	Δ(EF)
	$[ms]$	$[mmHg\ s^{-1}]$	$[mmHg\ s^{-1}]$	$[\%]$	$[mL]$	$[mL]$	$[\%]$	$[\%]$	$[\%]$
Pre-CRT	−	2487	−	−	79.0	−	−	27.0	−
LEAS	0	2778	+291	+11.7	90.0	+11.0	+13.9	31.0	+4.0
	15	2921	+434	+17.5	92.0	+13.0	+16.5	31.5	+4.5
	30	3025	+538	+21.6	92.0	+13.0	+16.5	31.6	+4.6
Veins 1	−30	2566	+79	+3.2	83.0	+4.0	+5.1	28.7	+1.7
	−15	2686	+199	+8.0	88.0	+9.0	+11.4	30.2	+3.2
	0	2856	+369	+14.8	93.0	+14.0	+17.7	32.0	+5.0
	15	3024	+537	+21.6	96.0	+17.0	+21.5	32.8	+5.8
	30	3163	+676	+27.2	96.0	+17.0	+21.5	33.1	+6.1
	40	3249	+762	+30.6	96.0	+17.0	+21.5	33.0	+6.0
	50	3355	+868	+34.9	94.0	+15.0	+19.0	32.5	+5.5
	60	3424	+937	+37.7	93.0	+14.0	+17.7	32.2	+5.2
Veins 2	0	2835	+348	+14.0	92.0	+13.0	+16.5	31.6	+4.6
	15	3004	+517	+20.8	95.0	+16.0	+20.3	32.5	+5.5
	30	3161	+674	+27.1	96.0	+17.0	+21.5	33.0	+6.0
	40	3267	+780	+31.4	96.0	+17.0	+21.5	33.0	+6.0
	50	3359	+872	+35.1	95.0	+16.0	+20.3	32.7	+5.7
	60	3424	+937	+37.7	93.0	+14.0	+17.7	32.2	+5.2
Veins 3	0	2759	+272	+10.9	94.0	+15.0	+19.0	32.1	+5.1
Veins 4	0	2713	+226	+9.1	95.0	+16.0	+20.3	32.6	+5.6
*Veins 5**	0	2831	+344	+13.8	93.0	+14.0	+17.7	32.1	+5.1
*Veins 6**	0	2883	+396	+15.9	78.0	−1.0	−1.3	27.0	+0.0
Veins 7	0	2801	+314	+12.6	91.0	+12.0	+15.2	31.2	+4.2

Table 4.2: Biomarkers corresponding to *virtual* CRT configurations for patient P5. (*Locations** are points laying in the fibrotic region).

We select as best *location-delay* configurations, i. e. the *optimal* CRT scenarios:

- *Veins 1* with VVD $= 60\ ms$ corresponding to the best value of $dP/dt|_{\max}$,

- *Veins 2* with VVD $= 40\ ms$ which represents the best compromise between pressure change and EF.

The PV-loops of these two scenarios are in Figure 4.13.
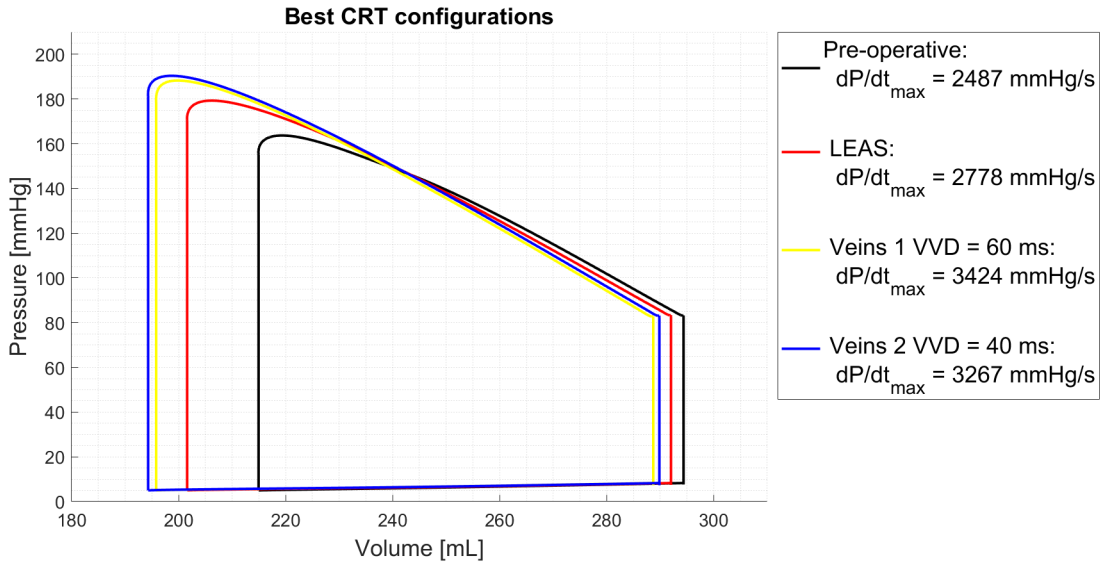
Figure 4.13: PV loops of the *optimal* CRT scenarios for patient P5, obtained varying both the LV pacing site and the VVD. On the right the values of $dP/dt|_{\max}$ are reported.

Giving a general analysis of the results presented in Table 4.2, we notice that negative VVDs produce a deterioration of both $dP/dt|_{\max}$ and EF, as it happened with patient P2. However, continuously increasing VVD > 0 does not lead to a limit value of $dP/dt|_{\max}$, which keeps improving, differently from EF that starts decreasing for VVD $> 40\ ms$.

In general, all *virtual* CRT scenarios produce promising results for this patient, with an improvement in EF that is kept around $4 - 5\%$ and, most importantly, $\Delta(dP/dt|_{\max}) > 10\%$ for almost all *virtual* CRT, exceeding 20% when VVD > 0 is imposed. The extremely high values of pressure change with respect to P2, are also a consequence of the lack of pressure calibration for Patient P5 (see Section 3.3.2), causing even more non-physiological $P_{\max}$ in a post-CRT context.

To conclude, we identify as *optimal* CRT scenario *Veins 1* with VVD $= 60\ ms$ corresponding to the maximum $\Delta(dP/dt|_{\max}) = 37.7\%$. The same values of biomarkers are obtained also for *Veins 2*, but we prefer *Veins 1* being closer to the coronary sinus (CS) and consequently more accessible in clinical practice.

Comparison of the qualitative mechanical behaviors

We report in Figure 4.14 the comparison of mechanical behaviors arising from the numerical solutions of the displacement $\boldsymbol{d}$ for *pre-operative*, *LEAS-based* CRT and *optimal* CRT scenarios, at three intermediate instants of the cardiac cycle.
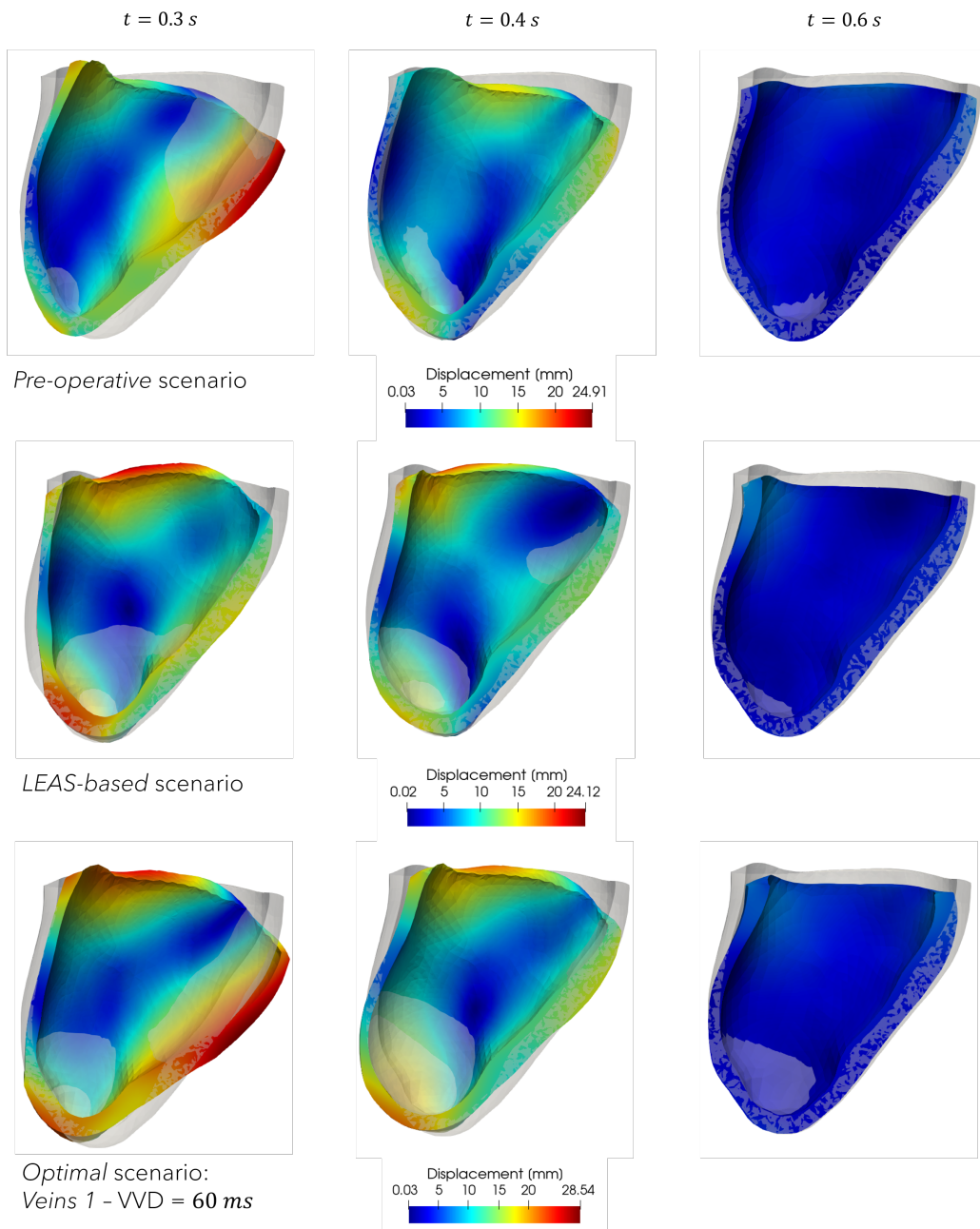
Figure 4.14: Qualitative comparison of displacements $\boldsymbol{d}$ among *pre-operative* (top), *LEAS-based* (middle) and *optimal* (bottom) scenarios, in the anterior portion of the truncated LV of patient P5 during a cardiac cycle.

We observe that the *LEAS-based* CRT appears qualitatively better with respect to the *pre-operative* case and the *optimal* CRT. In particular, when focusing on time $t = 0.3\ s$, the behavior arising from the *LEAS-based* case appears to be qualitatively the most synchronized. This result is in contradiction with the logic of guiding CRT left lead positioning according to the best $dP/dt|_{\max}$. A possible explanation relies again on the fact that the computational values of the biomarker determined for this patient are surely greater than the real values. If a further calibration is carried out for P5, so that physiological pressures can be restored, the maximum rate of pressure change may vary and its best improvement may correspond to a different *location-delay* configuration.

4.4. CRT simulations for Patient P8

We conclude the analysis of CRT simulations with Patient P8, who is characterized by a less dilated LV volume compared to P2 and P5, leading to an *EF* that is slightly above 30%. Moreover, P8 is affected by fibrosis, as reported in Figure 3.4.

4.4.1. CRT simulation at the Latest Electrically Activated Segment

We start from the reproduction of the *LEAS-based* clinical CRT scenario, whose solution of the Eikonal simulation is represented in Figure 4.15 for the particular case of VVD = 0, but the qualitative behavior remains the same also when varying the delay, setting VVD = 15 ms and VVD = 30 ms.
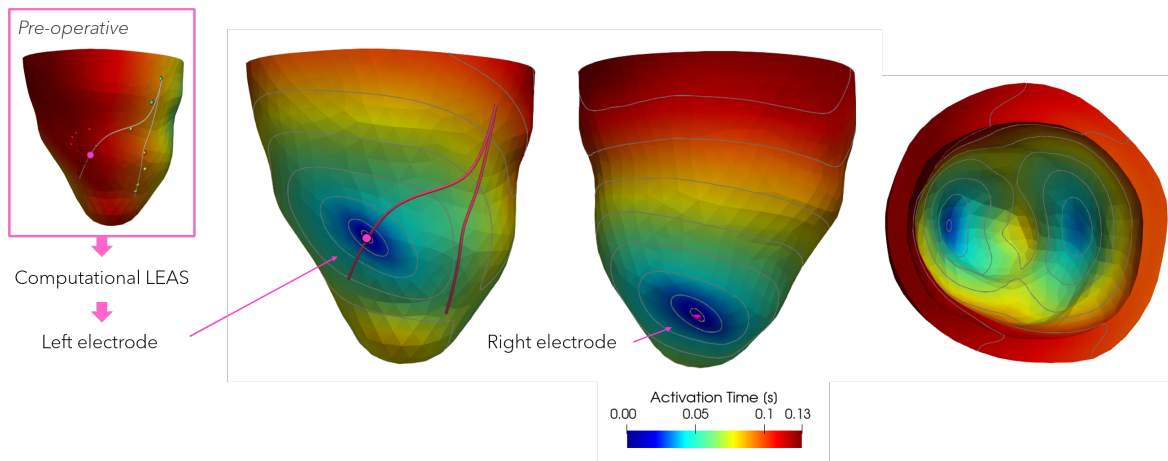
Figure 4.15: Simulated activation map of *LEAS-based* CRT for patient P8. The right electrode stimulus is showed on the left, while the LEAS stimulation is in the central picture. On the right the Eikonal solution is showed from a base point of view.

The plots of the PV-loops obtained with ERM simulations of the *LEAS-based* scenario for the three different delays, compared to the *pre-operative* case, are showed in Figure 4.16, where we add also the values of $dP/dt|_{\max}$ and EF. Looking at these diagrams, the CRT procedure appears to be much less effective on this patient than it was for P2 and P5. Indeed, the *LEAS-based* CRT PV-loops are almost overlapping with the *pre-operative* simulation, indicating that EF is practically unchanged. But, most importantly, the value of $dP/dt|_{\max}$ does not encounter any improvement: for the case VVD $= 0$ it even decreases, while for positive VVDs it has a mild increase of 1.4% and 2.7% for VVD $= 15$ ms and VVD $= 30$ ms, respectively.
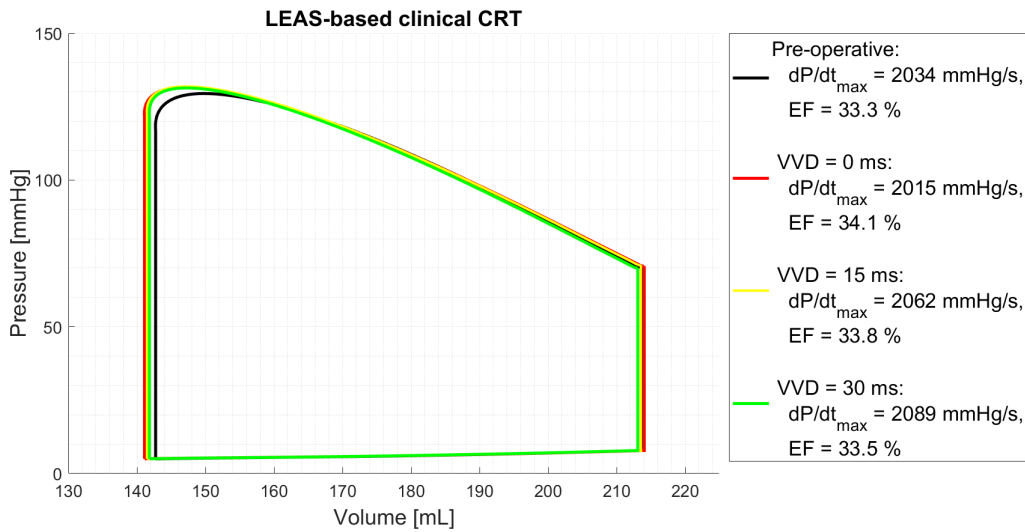
Figure 4.16: PV-loops comparison for patient P8 among *pre-operative* and *LEAS-based* scenarios with VVDs $= 0, 15, 30$ ms. Together with corresponding $dP/dt|_{\max}$ and EF.

4.4.2. Optimization of CRT varying left lead location and delay

Starting from the pacing site variation, in Figure 4.17 we present eight locations, chosen along the reconstructed veins to surrogate possible CRT lead positions and the two points corresponding to the *clinical* and the *computational* LEAS.

The vast fibrotic region characterizing the whole mid-apical LV portion of our interest can be immediately noticed. Indeed, almost the entire reconstructed veins lay in such region, leading to an inevitable left lead location within fibrotic tissue, except for two points, *Veins 2* and *Veins 3*. All the other points, including LEAS, are denoted with $'*'$ to underline that they belong to a slow conduction area.

We run eight preliminary simulations of *virtual* CRT scenarios for the selected points setting VVD $= 0$, that produce the electrical behaviors, coming from the Eikonal solution, reported in Figure 4.18.

- ⊙ Clinical LEAS *
- ◇ Computational LEAS *
- ◇ Location Veins 1 *
- ◇ Location Veins 2
- ◇ Location Veins 3
- ◇ Location Veins 4 *
- ◇ Location Veins 5 *
- ◇ Location Veins 6 *
- ◇ Location Veins 7 *
- ◇ Location Veins 8 *
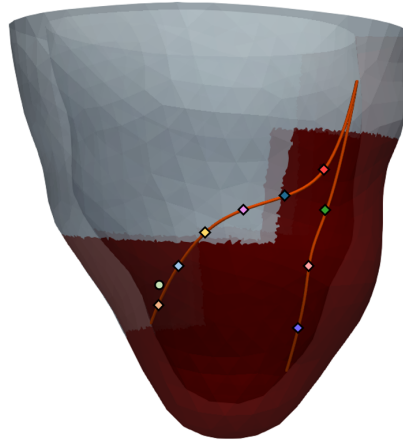
Figure 4.17: Locations of the LV lead for *virtual* CRT scenarios on patient P8. Also the clinical and computational LEAS positions are reported.
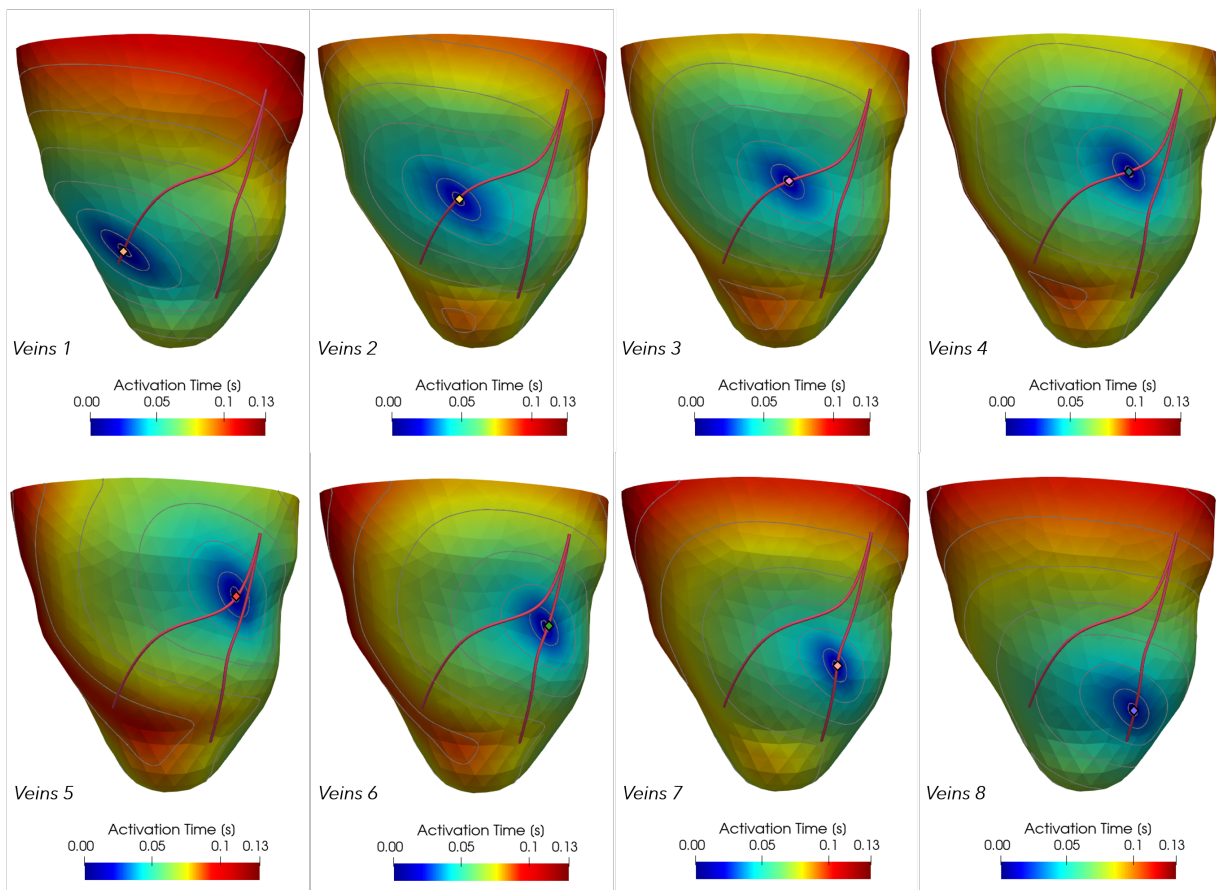
Figure 4.18: Activation maps of patient P8 resulting from Eikonal simulations of *virtual* CRT scenarios with VVD = 0.

The results of the ERM simulations are showed by means of PV-loops with the associated

$dP/dt|_{\max}$ in Figure 4.19, compared to the *pre-operative* and *LEAS-based* scenarios. We observe that the CRT procedure does not produce particular improvements in terms of biomarkers on patient P8, even after changing pacing site. The maximal $\Delta EF = 1.8\%$ corresponds to pacing at *Veins 5* and *Veins 6*, while there are other points in which EF even decreases with respect to the *pre-operative* case. Concerning $dP/dt|_{\max}$, its best, though mild, increase of 2% is obtained for *Veins 8*, but also this quantity is reduced in other selected locations. In particular, the worst outcomes correspond to locations *Veins 2* and *Veins 3*, that are also the only ones positioned outside of the ischemic region. Hence, for this patient-specific case we can say that pacing inside a fibrotic region does not seem to negatively influence the procedure.
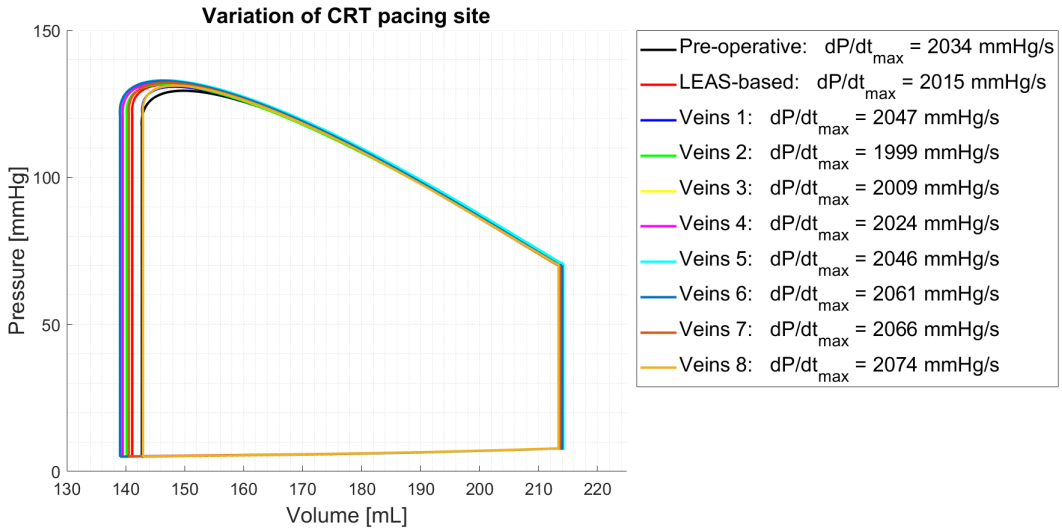
Figure 4.19: PV loops of *virtual* CRT scenarios for patient P8 obtained varying the LV pacing site, keeping VVD = 0. On the right the values of $dP/dt|_{\max}$ are reported.

Then, the locations associated with higher improvements in maximum rate of pressure change are used to perform further simulations varying the inter-ventricular delay:

- *Veins 6* corresponds to $\Delta(dP/dt|_{\max}) = 1.3\%$ and to the highest ΔEF,

- *Veins 7* has a better improvement in pressure change, with $\Delta(dP/dt|_{\max}) = 1.6\%$, but worse EF,

- *Veins 8* was already mentioned as the point ensuring the best value of $dP/dt|_{\max}$, but it concurrently leads to a worsened EF.

The VVD is initially varied between 0, 10 *ms* and 20 *ms* for all three points. A further VVD = 30 *ms* is simulated for *Veins 6*. We also try with negative VVDs equal to -10 *ms* and -20 *ms* for *Veins 6* and *Veins 8*, since these two locations seem to produce more

promising outcomes than *Veins 7*.

The computational biomarkers computed for every *virtual* CRT scenario are all reported in Table 4.3.

Scenario	Delay	$dP/dt\|_{\mathbf{max}}$	$\mathbf{\Delta}(dP/dt\|_{\mathbf{max}})$		SV	$\mathbf{\Delta}$(SV)		EF	$\mathbf{\Delta}$(EF)
	$[ms]$	$[mmHg\ s^{-1}]$	$[mmHg\ s^{-1}]$	$[\%]$	$[mL]$	$[mL]$	$[\%]$	$[\%]$	$[\%]$
Pre-CRT	−	2034	−	−	71.0	−	−	33.3	−
*LEAS**	0	2015	−19	−0.9	73.0	+2.0	+2.8	34.1	+0.8
	15	2062	+28	+1.4	72.0	+1.0	+1.4	33.8	+0.15
	30	2089	+55	+2.7	71.0	+0.0	+0.0	33.5	+0.2
*Veins 1**	0	2047	+13	+0.6	71.0	+0.0	+0.0	33.2	−0.1
Veins 2	0	1999	−35	−1.7	74.0	+3.0	+4.2	34.6	+1.3
Veins 3	0	2009	−25	−1.2	75.0	+4.0	+5.6	34.9	+1.6
*Veins 4**	0	2024	−10	−0.5	75.0	+4.0	+5.6	34.8	+1.5
*Veins 5**	0	2046	+12	+0.6	75.0	+4.0	+5.6	35.1	+1.8
*Veins 6**	−20	2018	−16	−0.8	73.0	+2.0	+2.8	34.4	+1.1
	−10	2037	+3	+0.1	74.0	+3.0	+4.2	34.8	+1.5
	0	2061	+27	+1.3	75.0	+4.0	+5.6	35.1	+1.8
	10	2082	+48	+2.4	75.0	+4.0	+5.6	35.0	+1.7
	20	2091	+57	+2.8	74.0	+3.0	+4.2	34.5	+1.2
	30	2091	+57	+2.8	73.0	+2.0	+2.8	34.1	+0.8
*Veins 7**	0	2066	+32	+1.6	73.0	+2.0	+2.8	34.2	+0.9
	10	2076	+42	+2.1	72.0	+1.0	+1.4	33.9	+0.6
	20	2078	+44	+2.2	71.0	+0.0	+0.0	33.4	+0.1
*Veins 8**	−20	2024	−10	−0.5	70.0	−1.0	−1.4	32.9	−0.4
	−10	2049	+15	+0.7	71.0	+0.0	+0.0	33.1	−0.2
	0	2074	+40	+2.0	71.0	+0.0	+0.0	33.1	−0.2
	10	2094	+60	+2.9	70.0	−1.0	−1.4	32.9	−0.4
	20	2094	+60	+2.9	70.0	−1.0	−1.4	32.9	−0.4

Table 4.3: Biomarkers corresponding to *virtual* CRT configurations for patient P8. (*Locations** are points laying in the fibrotic region).

We choose as best combinations of *location-delay*, i. e. *optimal* CRT scenarios:

- *Veins 6* with VVD = 20 *ms*,

- *Veins 8* with VVD = 10 *ms*.

The respective PV-loops are compared in Figure 4.20, where we can notice that they are still almost overlapping with the *pre-operative* and *LEAS-based* diagrams because of the almost unchanged EF values. Moreover, the maximum rate of pressure change $dP/dt|_{\max}$ is reported for every PV-loop, highlighting once again its poor increase post-CRT: both configurations produce a $\Delta(dP/dt|_{\max}) \sim 3\%$, which is the best that we are able to obtain.
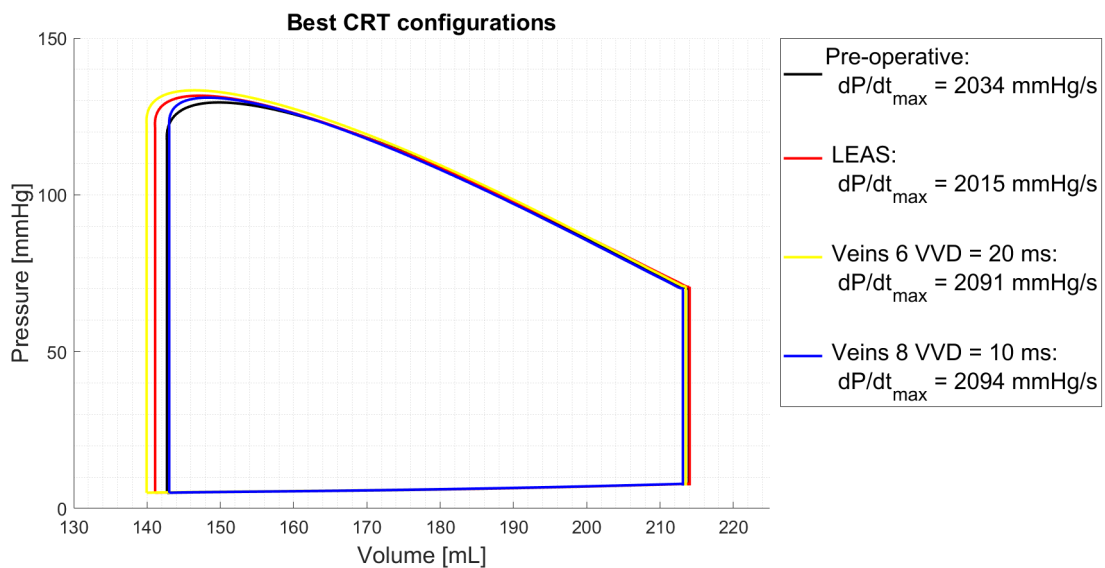
Figure 4.20: PV loops of the *optimal* CRT scenarios for patient P8, obtained varying both the LV pacing site and the VVD. On the right the values of $dP/dt|_{\max}$ are reported.

As we had already deduced from the first simulations of the clinical *LEAS-based* CRT, the *virtual* CRT scenarios reproduced for this patient and collected in Table 4.3 do not reflect a great beneficial effect of the therapy. In general, the increment of EF never goes above 1.8%, while $\Delta(dP/dt|_{\max})$ is always lower than 3%. The difference with the other two patients is that in this case there are several *virtual* scenarios leading to worsened outcomes even compared to the *pre-operative* case.

Moreover, exactly as it was for P2 and P5, setting negative inter-ventricular delays entails worse values of the biomarkers than those obtained for VVD > 0. Positive delays allow to obtain larger $\Delta(dP/dt|_{\max})$, that reaches an almost stationary value for VVD > 10 *ms*.

We select among the two configurations of Figure 4.20, *Veins 6* - VVD = 20 *ms* as *optimal* scenario to carry out a final analysis. We do not choose *Veins 8* because, apart from the lower EF, it is also in an apical position, which is usually not suggested by clinicians.

Comparison of the qualitative mechanical behaviors

We compare the qualitative mechanical behaviors of *pre-operative, LEAS-based* and *optimal* scenarios, looking at the time-evolution of the numerical displacement $\boldsymbol{d}$ in Figure 4.21, representing three intermediate times of the cardiac cycle for each case.
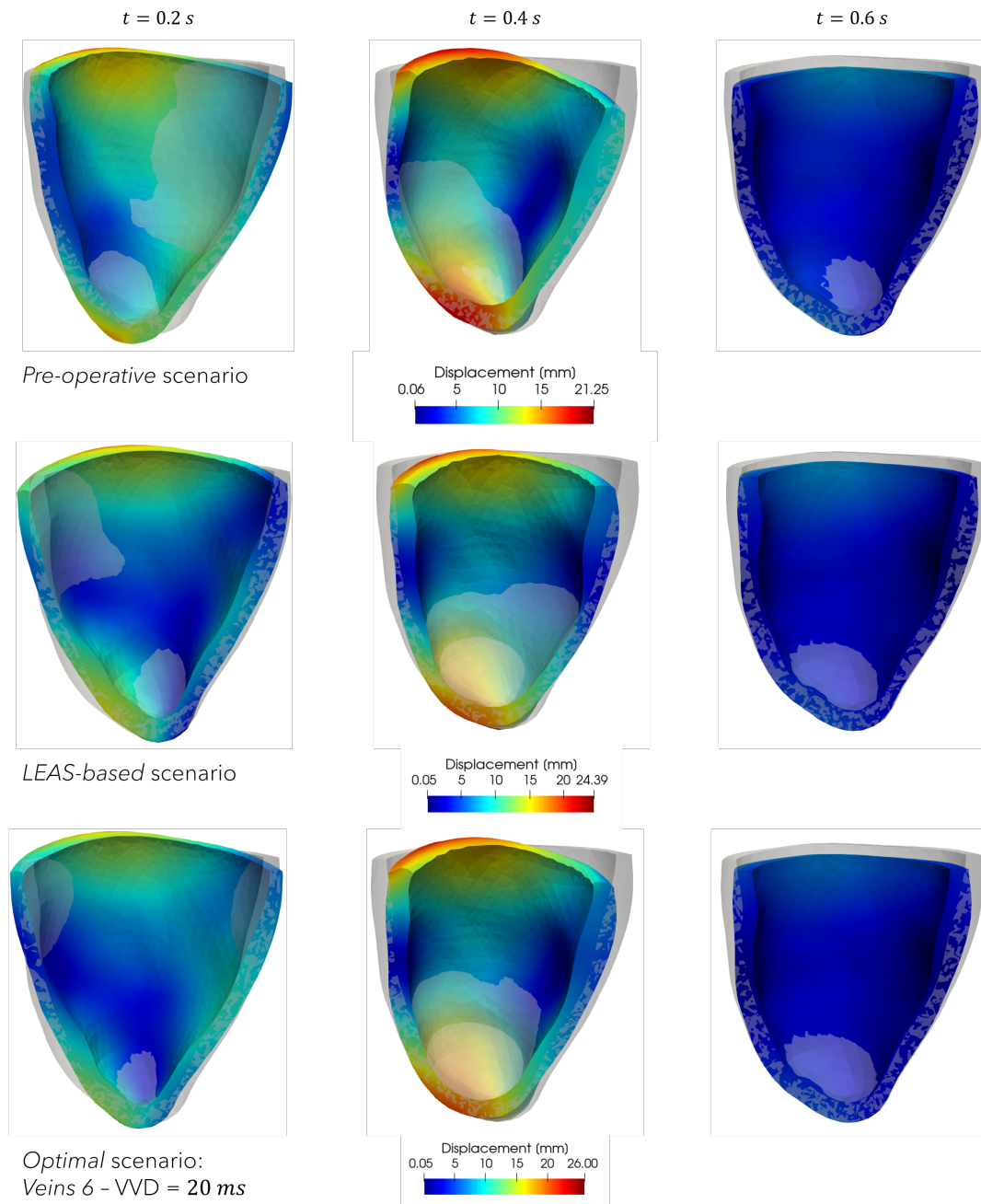
Figure 4.21: Qualitative comparison of displacements $\boldsymbol{d}$ among *pre-operative* (top), *LEAS-based* (middle) and *optimal* (bottom) scenarios, in the anterior portion of the truncated LV of patient P8 during a cardiac cycle.

The two post-CRT mechanical behaviors are qualitatively the same. The poor improvement of biomarkers for any CRT scenario would suggest a practically absent effect of resynchronization of ventricular motion. But actually, we can notice a slightly more coordinated contraction of the left ventricle compared to the dyssynchrony observed pre-CRT, that is evident especially at time instant $t = 0.4 \; s$.

4.5.   Final remarks on CRT virtual simulations

In this Chapter we addressed the application of the calibrated ERM model, retrieved in Chapter 3 for patients P2, P5 and P8, on the electromechanical simulation of the patient's LV undergoing Cardiac Resynchronization Therapy. Since the therapy still needs optimization in order to increase the percentage of responders, we looked for alternative pacing configurations of *virtual* CRT scenarios besides the clinical *LEAS-based* procedure, that imposes the left ventricular electrode to be positioned at LEAS.

In all three patients we were able to find locations along the coronary veins to be used as pacing site which highlighted optimal properties and seem to perform better than LEAS. This is a confirmation of the utility of computational models in predicting the possible CRT acute outcomes before the procedure is actually carried out, so that individualized settings can be defined for a personalized treatment.

Concerning the evaluation of outcomes, we employed the rate of improvement of $dP/dt|_{\mathrm{max}}$ with respect to the *pre-operative* scenario for all patients and the results were very different between each other.

Optimal left lead position.   It is found in diverse regions of the ventricular epicardium depending on the patient.

- For Patient P2 and P8 the best pacing site is found at *Veins 7* and *Veins 6*, respectively, which are both in a mid portion of the anterior surface of the ventricle.

- For P5 the optimal location is determined at *Veins 1*, located in a much more lateral region of the basal portion.

Relative increase of the biomarker. $\Delta(dP/dt|_{\mathrm{max}})$ varies in very different ranges among the three patients.

- Increment of $\sim 5 - 15\%$ for P2,

- Increment of $\sim 10 - 35\%$ for P5,

- Increment of $\sim 0 - 3\%$ for P8.

As a consequence, the effect of resynchronization on patients P2 and P8 is less evident when looking at the time evolution of the myocardial displacement plotted on the truncated anterior LV during a cardiac cycle, in Figures 4.7 and 4.21, respectively.

On the other hand, the best increment of $dP/dt|_{\max}$ is not always reflected in the most coordinated ventricular contraction from a qualitative point of view, as it happens for P5 where the *LEAS-based* scenario seems to be more effective than the *optimal* one (see Figure 4.14).

Optimization of the interventricular delay.   In all patient-specific cases the response to VVD variations is similar:

- Increasing VVD > 0 entails a higher improvement of $dP/dt|_{\max}$,

- Imposing VVD < 0 is never optimal.

Effect of fibrotic tissue.   From our analysis we deduce that choosing a location for the left lead inside the ischemic region does not worsen the acute outcomes of CRT, neither for P5, nor for P8.

Increase of maximum pressure post-CRT.   The main assumption made at the beginning of the Chapter to perform CRT simulations, imposes the calibrated *pre-operative* ERM parameters of Chapter 3 to remain unchanged acutely after CRT implantation. The consequence of keeping fixed the peripheral resistance R when simulating acute *virtual* CRT scenarios is an inevitable increase of the maximal pressure $P_{\max}$ reached during the cardiac cycle.

The explanation relies on the fact that the application of CRT increases the EF, meaning that a higher amount of blood is ejected from the LV in post-CRT context. If the resistances remain the same acutely, the chamber will need to do more work in order to pump more blood, leading to increased values of pressure. Such effect is confirmed by clinicians that also observed a pressure increase immediately after the procedure.

5 | Conclusions and future developments

In this thesis we were able to accomplish the two main purposes addressed at the beginning of the manuscript.

We were provided with three clinical cases by the Hospital of S. Maria del Carmine in Rovereto (TN), Italy, to investigate the application of the *Eikonal-Reaction-Mechanics* (ERM) computational model to the context of *left bundle branch block* (LBBB) and *ventricular dyssynchrony* (VD) pathologies, and, subsequently, to their treatment via Cardiac Resynchronization Therapy (CRT).

First of all, we managed to calibrate on each of the three patients the electrical and mechanical components of the ERM model describing the *pre-operative*, i. e. pre-CRT, LV electromechanical behavior, using clinical patients' data (from MRI and EAMS) that had been already adapted to the present computational framework thanks to a pre-processing procedure. Exploiting this fundamental information, we first calibrated the Eikonal model using all the electrical measurements and obtaining satisfying results. Most importantly, we included regions of slower conduction taking into account the fibrosis distributions of two of the patients. For calibration of the mechanics and the simplified 0D circulation models we introduced the first big improvement with respect to previous works: the use of all clinical data that were currently available, including pressure recordings besides the MRI measured volumes, so that the real PV loops could be computationally reproduced by ERM simulations.

Once the first goal of electromechanical calibration was accomplished, we aimed at applying such personalized models to simulate LV activity after CRT implantation. In particular, we were able to identify the simulated latest electrically activated segment (LEAS) and compare it with the clinical LEAS, so that the *clinical* CRT scenario could be replicated with numerical simulations. This allowed us to establish the ability of the computational tool to virtually reproduce and predict the response of each patient to this particular clinical therapy. Additionally, we ran several simulations moving the left elec-

trode position from LEAS and varying the interventricular delay between right and left lead, so that *virtual* CRT scenarios could be evaluated to determine whether they could be more beneficial to the patient with respect to the usual clinical procedure (*LEAS-based* scenario).

This work represents a first attempt towards the employment of a cardiac computational model to support therapy planning in daily clinical practice. The possibility of such mathematical model to accurately reproduce how a LV would react to a particular configuration of the CRT settings is of utmost importance in reducing the invasiveness of the procedure and optimizing its outcomes. Indeed, a way of improving the percentage of CRT responders is the programming of the procedure settings on a patient-specific level: our results proved that every patient reacts differently to pacing in a certain region of the ventricle with a certain delay. The *optimal* CRT scenario for a patient, could be the worst for another.

Of course, the methods proposed in this thesis have some limitations, leading to possible future improvements to make them more accurate and reliable:

- The Purkinje network is surrogated in the Eikonal model by simple stimuli imposed on the epicardial surface in the septal portion of the ventricle. In order to better describe the initiation of electrical activation, a more sophisticated model for the Purkinje system should be coupled with the Eikonal equation.

- The assignment of a constant degree of fibrosis to the whole unhealthy tissue of the reconstructed fibrosis distribution may be limiting. Allowing the variation of the degree of conductivity reduction among different fibrotic regions could lead to a more accurate reproduction of recorded activation maps.

- The period of a single simulated cardiac cycle is set to a default value of 0.8 s for all considered patients, thus leading to instabilities in the pressure-volume solution especially in patient P2 case. Retrieving the cardiac frequencies measured by cardiologists, if available, and include them as input datum of the personalized ERM model would ensure a better accuracy of the PV loop diagrams and consequently more precise computations of biomarkers for CRT outcomes evaluation.

- The electromechanical calibration could be automatized introducing numerical optimization methods that minimize the error committed in the reproduction of patient-specific measures.

- The ERM model is defined only in a left ventricular domain. Introducing a complete bi-ventricular geometry will allow to obtain more realistic CRT scenarios and a

better understanding of the procedure.

- The validation of CRT simulations could be carried out using clinical data recorded after implantation. So that, the hypothesis of keeping fixed the calibrated pre-operative parameters for acute post-CRT simulations, could be verified. Otherwise, an additional calibration procedure would be needed for a more reliable analysis of CRT outcomes.

- Further research for biomarkers, besides the maximum rate of pressure change, to evaluate acute effects of the therapy could help in the identification of the *optimal* CRT scenario.

- The optimization of CRT may be sped up as well implementing an algorithm able to automatically generate random locations and delays of the left lead, simulate all the possible combinations and evaluate the best one based on the value of the biomarkers.

Bibliography

[1] Zygote solid 3d heart generation ii development report. Technical report, Media Group Inc., 2014.

[2] W. T. Abraham, W. G. Fisher, A. L. Smith, D. B. Delurgio, A. R. Leon, E. Loh, D. Z. Kocovic, M. Packer, A. L. Clavell, D. L. Hayes, M. Ellestad, R. J. Trupp, J. Underwood, F. Pickering, C. Truex, P. McAtee, and J. Messenger. Cardiac resynchronization in chronic heart failure. *The New England Journal of Medicine*, 346(24):1845–1853, 2002.

[3] J. Aguado-Sierra, A. Krishnamurthy, C. Villongco, J. Chuang, E. Howard, M. J. Gonzales, J. Omens, D. E. Krummen, S. Narayan, R. C. Kerckhoffs, and A. D. McCulloch. Patient-specific modeling of dyssynchronous heart failure: A case study. *Progress in Biophysics and Molecular Biology*, 107(1):147–155, 2011.

[4] AMBOSS. Heart, 2022. URL `https://www.amboss.com/us/knowledge/Heart`.

[5] AMBOSS. Cardiac physiology, 2022. URL `https://www.amboss.com/us/knowledge/Cardiac_physiology`.

[6] T. Arts, R. S. Reneman, and P. C. Veenstra. A model of the mechanics of the left ventricle. *Annals of Biomedical Engineering*, 7:299–318, 1979.

[7] A. Auricchio, H. Klein, B. Tockman, S. Sack, C. Stellbrink, J. Neuzner, A. Kramer, J. Ding, T. Pochet, A. Maarse, and J. Spinelli. Transvenous biventricular pacing for heart failure: Can the obstacles be overcome? *The American Journal of Cardiology*, 83(5):130D–135D, 1999.

[8] A. Auricchio, C. Stellbrink, M. Block, S. Sack, J. Vogt, P. Bakker, H. Klein, A. Kramer, J. Ding, R. Salo, B. Tockman, T. Pochet, and J. Spinelli. Effect of pacing chamber and atrioventricular delay on acute systolic function of paced patients with congestive heart failure. *Circulation*, 99(23):2993–3001, 1999.

[9] A. Auricchio, C. Stellbrink, S. Sack, M. Block, J. Vogt, P. Bakker, P. Mortensen, and H. Klein. The pacing therapies for congestive heart failure (path-chf) study:

rationale, design, and endpoints of a prospective randomized multicenter study. *The American Journal of Cardiology*, 83(5):136D–142D, 1999.

[10] J. D. Bayer, R. C. Blake, G. Plank, and N. A. Trayanova. A novel rule-based algorithm for assigning myocardial fiber orientation to computational heart models. *Annals of Biomedical Engineering*, 40:2243–2254, 2012.

[11] G. B. Bleeker, T. A. Kaandorp, H. J. Lamb, E. Boersma, P. Steendijk, A. de Roos, E. E. van der Wall, M. J. Schalij, and J. J. Bax. Effect of posterolateral scar tissue on clinical and echocardiographic improvement after cardiac resynchronization therapy. *Circulation*, 113(7):969–976, 2006.

[12] M. D. Bogaard, P. Houthuizen, F. A. Bracke, P. A. Doevendans, F. W. Prinzen, M. Meine, and B. M. van Gelder. Baseline left ventricular dp/dt max rather than the acute improvement in dp/dtmax predicts clinical outcome in patients with cardiac resynchronization therapy. *European Journal of Heart Failure*, 13(10):1126–1132, 2011.

[13] G. Boriani, M. Biffi, C. P. Müller, K.-H. Seidl, R. Grove, J. Vogt, W. Danschel, A. Schuchert, J.-C. Deharo, T. Becker, E. Boulogne, and H. J. Trappe. A prospective randomized evaluation of vv delay optimization in crt-d recipients: Echocardiographic observations from the rhythm ii icd study. *Pacing and Clinical Electrophysiology*, 32:S120–S125, 2009.

[14] Boston Scientific. How crts work. URL `https://www.bostonscientific.com/en-US/patients/about-your-device/crt-devices/how-crts-work.html`.

[15] P. Bovendeerd, T. Arts, J. M. Huyghe, D. H. van Campen, and R. S. Reneman. Dependence of local left ventricular wall mechanics on myocardial fiber orientation: a model study. *Journal of biomechanics*, 25:1129–40, 1992.

[16] A. Bueno-Orovio, E. M. Cherry, and F. H. Fenton. Minimal model for human ventricular action potentials in tissue. *Journal of Theoretical Biology*, 253(3):544–560, 2008.

[17] C. Butter, A. Auricchio, C. Stellbrink, E. Fleck, J. Ding, Y. Yu, E. Huvelle, and J. Spinelli. Effect of resynchronization therapy stimulation site on the systolic function of heart failure patients. *Circulation*, 104(25):3026–3029, 2001.

[18] R. Buttner and E. Burns. Life in the fastlane: Left bundle branch block (lbbb), 2021. URL `https://litfl.com/left-bundle-branch-block-lbbb-ecg-library/`.

[19] Cardio Secur. Ecg lead systems. URL `https://www.cardiosecur.com/magazine/specialist-articles-on-the-heart/lead-systems-how-an-ecg-works`.

[20] M. D. Cerqueira, N. J. Weissman, V. Dilsizian, A. K. Jacobs, S. Kaul, W. K. Laskey, D. J. Pennell, J. A. Rumberger, T. Ryan, and M. S. Verani. Standardized myocardial segmentation and nomenclature for tomographic imaging of the heart. *Circulation*, 105(4):539–542, 2002.

[21] R. Chabiniok, D. Chapelle, P.-F. Lesault, A. Rahmouni, and J.-F. Deux. Validation of a biomechanical heart model using animal data with acute myocardial infarction. *CI2BM09 - MICCAI Workshop on Cardiovascular Interventional Imaging and Biophysical Modelling*, 2009.

[22] R. Chabiniok, P. Moireau, P. F. Lesault, A. Rahmouni, J. F. Deux, and D. Chapelle. Estimation of tissue contractility from cardiac cine-mri using a biomechanical heart model. *Biomechanics and Modeling in Mechanobiology*, 11(7):609–630, 2012.

[23] R. Chabiniok, V. Y. Wang, M. Hadjicharalambous, L. Asner, J. Lee, M. Sermesant, E. Kuhl, A. A. Young, P. Moireau, M. P. Nash, D. Chapelle, and D. A. Nordsletten. Multiphysics and multiscale modelling, data–model fusion and integration of organ physiology in the clinic: ventricular cardiac mechanics. *Interface Focus*, 6, 2016.

[24] B. T. Chan, C. W. Ong, E. Lim, N. A. Abu Osman, A. Al Abed, N. H. Lovell, and S. Dokos. Simulation of left ventricle flow dynamics with dilated cardiomyopathy during the filling phase. In *2012 Annual International Conference of the IEEE Engineering in Medicine and Biology Society*, 2012.

[25] Y. Cheng, H. Oertel, and T. Schenkel. Fluid-structure coupled cfd simulation of the left ventricular flow during filling phase. *Annals of biomedical engineering*, 33: 567–576, 2005.

[26] G. V. Chow, J. E. Marine, and J. L. Fleg. Epidemiology of arrhythmias and conduction disorders in older adults. *Clinics in Geriatric Medicine*, 28:539–553, 2012.

[27] E. S. Chung, A. R. Leon, L. Tavazzi, J.-P. Sun, P. Nihoyannopoulos, J. Merlino, W. T. Abraham, S. Ghio, C. Leclercq, J. J. Bax, C.-M. Yu, J. G. III, M. S. J. Sutton, J. D. Sutter, and J. Murillo. Results of the predictors of response to crt (prospect) trial. *Circulation*, 117(20):2608–2616, 2008.

[28] P. Colli Franzone, L. F. Pavarino, and G. Savarè. *Computational electrocardiology: mathematical and numerical modeling*, pages 187–241. Springer Milan, 2006.

[29] C. M. Costa, A. Neic, K. Gillette, B. Porter, J. Gould, B. Sidhu, Z. Chen, M. Elliott,

V. Mehta, G. Plank, C. Rinaldi, M. J. Bishop, and S. A. Niederer. Left ventricular endocardial pacing is less arrhythmogenic than conventional epicardial pacing when pacing in proximity to scar. *Heart Rhythm*, 17:1262–1270, 2020.

[30] A. Crozier, B. Blazevic, P. Lamata, G. Plank, M. Ginks, S. Duckett, M. Sohal, A. Shetty, C. A. Rinaldi, R. Razavi, N. P. Smith, and S. A. Niederer. The relative role of patient physiology and device optimisation in cardiac resynchronisation therapy: A computational modelling study. *Journal of Molecular and Cellular Cardiology*, 96:93–100, 2016.

[31] D.Bamira and M.H.Picard. Imaging: Echocardiology—assessment of cardiac structure and function. In R. S. Vasan and D. B. Sawyer, editors, *Encyclopedia of Cardiovascular Research and Medicine*, pages 35–54. 2018.

[32] W. L. de Graaf, K. Vandoorne, F. Arslan, K. Nicolay, and G. J. Strijkers. Contrast-enhanced t1-mapping mri for the assessment of myocardial fibrosis. *Current Cardiovascular Imaging Reports*, 7(4), 2014.

[33] A. de Vecchi, D. A. Nordsletten, E. W. Remme, H. Bellsham-Revell, G. Greil, J. M. Simpson, R. Razavi, and N. P. Smith. Inflow typology and ventricular geometry determine efficiency of filling in the hypoplastic left heart. *The Annals of Thoracic Surgery*, 94:1562–1569, 2012.

[34] A. L. A. J. Dekker, B. Phelps, B. Dijkman, T. van Der Nagel, F. H. van Der Veen, G. G. Geskes, and J. G. Maessen. Epicardial left ventricular lead placement for cardiac resynchronization therapy: Optimal pace site selection with pressure-volume loops. *The Journal of Thoracic and Cardiovascular Surgery*, 127(6):1641–1647, 2004.

[35] M. Del Greco, A. Zorzi, I. Di Matteo, A. Cima, M. Maines, C. Angheben, and D. Catanzariti. Coronary sinus activation patterns in patients with and without left bundle branch block undergoing electroanatomic mapping system–guided cardiac resynchronization therapy device implantation. *Heart Rhythm*, 14(2):225–233, 2017.

[36] V. Delgado and J. J. Bax. Is assessment of systolic dyssynchrony for cardiac resynchronization therapy clinically useful? *Circulation*, 123(6):640–655, 2011.

[37] V. Delgado, R. J. van Bommel, M. Bertini, C. J. W. Borleffs, N. A. Marsan, A. C. Ng, G. Nucifora, N. R. van de Veire, C. Ypenburg, E. Boersma, E. R. Holman, M. J. Schalij, and J. J. Bax. Relative merits of left ventricular dyssynchrony, left ventricular lead position, and myocardial scar to predict long-term survival of ischemic

heart failure patients undergoing cardiac resynchronization therapy. *Circulation*, 123(1):70–78, 2011.

[38] N. Derval, P. Steendijk, L. J. Gula, A. Deplagne, J. Laborderie, F. Sacher, S. Knecht, M. Wright, I. Nault, S. Ploux, P. Ritter, P. Bordachar, S. Lafitte, P. Réant, G. J. Klein, S. M. Narayan, S. Garrigue, M. Hocini, M. Haissaguerre, J. Clementy, and P. Jais. Optimizing hemodynamics in heart failure patients by systematic screening of left ventricular pacing sites. *Journal of the American College of Cardiology*, 55 (6):566–575, 2010.

[39] M. Disertori, M. Masè, and F. Ravelli. Myocardial fibrosis predicts ventricular tachyarrhythmias. *Trends in cardiovascular medicine*, 27(5):363–372, 2017.

[40] Dr. Sanjib Patra. Cardiac resynchronization therapy: Biventricular pacemaker, 2020. URL `https://drsanjibpatra.com/cardiac-resynchronization-therapy-crt/`.

[41] S. G. Duckett, M. Ginks, A. K. Shetty, J. Bostock, J. S. Gill, S. Hamid, S. Kapetanakis, E. Cunliffe, R. Razavi, G. Carr-White, and C. A. Rinaldi. Invasive acute hemodynamic response to guide left ventricular lead implantation predicts chronic remodeling in patients undergoing crt. *Journal of the American College of Cardiology*, 58(11):1128–1136, 2011.

[42] ECG and ECHO learning. Clinical echocardiography: Ventricular pressure-volume relationship. URL `https://ecgwaves.com/topic`.

[43] C. Eitel, G. Hindricks, N. Dagres, P. Sommer, and C. Piorkowski. Ensite velocity™ cardiac mapping system: a new platform for 3d mapping of cardiac arrhythmias. *Expert Review of Medical Devices*, 7(2):185–192, 2010.

[44] M. Fedele and A. Quarteroni. Polygonal surface processing and mesh generation tools for the numerical simulation of the cardiac function. *International Journal for Numerical Methods in Biomedical Engineering*, 37(4):e3435, 2021.

[45] R. FitzHugh. Impulses and physiological states in theoretical models of nerve membrane. *Biophysical Journal*, 1(6):445–466, 1961.

[46] P. C. Franzone, L. Guerri, and S. Rovida. Wavefront propagation in an activation model of the anisotropic cardiac tissue: asymptotic analysis and numerical simulations. *Journal of Mathematical Biology*, 28:121–176, 1990.

[47] P. C. Franzone, L. F. Pavarino, and S. Scacchi. *Mathematical Cardiac Electrophysiology*. Springer Cham, 2014.

[48] P. C. Franzone, L. F. Pavarino, and S. Scacchi. Bioelectrical effects of mechanical feedbacks in a strongly coupled cardiac electro-mechanical model. *Mathematical Models and Methods in Applied Sciences*, 26:27–57, 2016.

[49] M. Glikson, J. C. Nielsen, M. B. Kronborg, Y. Michowitz, A. Auricchio, I. M. Barbash, J. A. Barrabés, G. Boriani, F. Braunschweig, M. Brignole, H. Burri, A. J. S. Coats, J.-C. Deharo, V. Delgado, G.-P. Diller, C. W. Israel, A. Keren, R. E. Knops, D. Kotecha, C. Leclercq, B. Merkely, C. Starck, I. Thylén, J. M. Tolosana, and E. S. D. Group. 2021 esc guidelines on cardiac pacing and cardiac resynchronization therapy: Developed by the task force on cardiac pacing and cardiac resynchronization therapy of the european society of cardiology (esc) with the special contribution of the european heart rhythm association (ehra). *European Heart Journal*, 42(35): 3427–3520, 2021.

[50] C. L. Grines, T. M. Bashore, H. Boudoulas, S. Olson, P. Shafer, and C. F. Wooley. Functional abnormalities in isolated left bundle branch block. the effect of interventricular asynchrony. *Circulation*, 79(4):845–853, 1989.

[51] J. M. Guccione, A. D. McCulloch, and L. K. Waldman. Passive Material Properties of Intact Ventricular Myocardium Determined From a Cylindrical Model. *Journal of Biomechanical Engineering*, 113(1):42–55, 1991.

[52] J. M. Guccione, K. D. Costa, and A. D. McCulloch. Finite element stress analysis of left ventricular mechanics in the beating dog heart. *Journal of Biomechanics*, 28 (10):1167–1177, 1995.

[53] V. Gurev, T. Lee, J. Constantino, H. Arevalo, and N. A. Trayanova. Models of cardiac electromechanics based on individual hearts imaging data. *Biomechanics and Modeling in Mechanobiology*, 10:295–306, 2011.

[54] A. Hadjis, R. Proietti, and V. Essebag. Implantation of cardiac resynchronization therapy devices using three leads by cephalic vein dissection approach. *Europace*, 19(9):1514–1520, 2017.

[55] S. Hinderer and K. Schenke-Layland. Cardiac fibrosis. a short review of causes and therapeutic strategies. *Advanced Drug Delivery Reviews*, 146:77–82, 2019.

[56] E. R. Hyde, J. M. Behar, S. Claridge, T. Jackson, A. W. Lee, E. W. Remme, M. Sohal, G. Plank, R. Razavi, C. A. Rinaldi, and S. A. Niederer. Beneficial effect on cardiac resynchronization from left ventricular endocardial pacing is mediated by early access to high conduction velocity tissue. *Circulation: Arrhythmia and Electrophysiology*, 8(5):1164–1172, 2015.

[57] P. A. Iaizzo. *Handbook of Cardiac Anatomy, Physiology and Devices*. Humana Press, 2005.

[58] A. H. M. Jansen, F. Bracke, J. melle van Dantzig, K. H. Peels, J. C. Post, H. C. M. van den Bosch, B. van Gelder, A. Meijer, H. H. M. Korsten, J. de Vries, and N. M. van Hemel. The influence of myocardial scar and dyssynchrony on reverse remodeling in cardiac resynchronization therapy. *European Journal of Echocardiography*, 9(4):483–488, 2008.

[59] C. Jellis, J. Martin, J. Narula, and T. H. Marwick. Assessment of nonischemic myocardial fibrosis. *Journal of Cardiovascular Electrophysiology*, 56(2):89–97, 2010.

[60] S. Kapetanakis, M. Kearney, A. Siva, N. Gall, M. Cooklin, and M. Monaghan. Real-time three-dimensional echocardiography a novel technique to quantify global left ventricular mechanical dyssynchrony. *Circulation*, 112(7):992–1000, 2005.

[61] E. Kayvanpour, T. Mansi, F. Sedaghat-Hamedani, A. Amr, D. Neumann, B. Georgescu, P. Seegerer, A. Kamen, J. Haas, K. S. Frese, M. Irawati, E. Wirsz, V. King, S. Buss, D. Mereles, E. Zitron, A. Keller, H. A. Katus, D. Comaniciu, and B. Meder. Towards personalized cardiology: Multi-scale modeling of the failing heart. *PLOS ONE*, 10:1–18, 2015.

[62] R. C. Kerckhoffs, A. D. McCulloch, J. H. Omens, and L. J. Mulligan. Effects of biventricular pacing and scar size in a computational model of the failing heart with left bundle branch block. *Medical Image Analysis*, 13(2):362–369, 2009.

[63] R. C. P. Kerckhoffs, O. P. Faris, P. H. M. Bovendeerd, F. W. Prinzen, K. Smits, E. R. McVeigh, and T. Arts. Timing of depolarization and contraction in the paced canine left ventricle: Model and experiment. *Journal of Cardiovascular Electrophysiology*, 14:S188–S195, 2003.

[64] R. C. P. Kerckhoffs, M. L. Neal, Q. Gu, J. B. Bassingthwaighte, J. H. Omens, and A. D. McCulloch. Coupling of a 3d finite element model of cardiac ventricular mechanics to lumped systems models of the systemic and pulmonic circulation. *Annals of biomedical engineering*, 35(1):1–18, 2007.

[65] Kevin James Cyr. Heart health. what is ventricular dyssynchrony?, 2021. URL https://www.verywellhealth.com/ventricular-dyssynchrony-5193815#toc-prognosis.

[66] F. Z. Khan, M. S. Virdee, S. P. Fynn, and D. P. Dutka. Left ventricular lead

placement in cardiac resynchronization therapy: where and how? *Europace*, 11(5): 554–561, 2009.

[67] F. Z. Khan, M. S. Virdee, C. R. Palmer, P. J. Pugh, D. O'Halloran, M. Elsik, P. A. Read, D. Begley, S. P. Fynn, and D. P. Dutka. Targeted left ventricular lead placement to guide cardiac resynchronization therapy. *Journal of the American College of Cardiology*, 59(17):1509–1518, 2012.

[68] S. G. Khan, D. Klettas, S. Kapetanakis, and M. J. Monaghan. Clinical utility of speckle-tracking echocardiography in cardiac resynchronisation therapy. *Echo Research and Practice*, 3(1):R1–R11, 2016.

[69] J. A. Kirk and D. A. Kass. Electromechanical dyssynchrony and resynchronization of the failing heart. *Circulation Research*, 113(6):765–776, 2013.

[70] P. Lamata, R. Casero, V. Carapella, S. A. Niederer, M. J. Bishop, J. E. Schneider, P. Kohl, and V. Grau. Images as drivers of progress in cardiac computational modelling. *Progress in Biophysics and Molecular Biology*, 115:198–212, 2014.

[71] C. T. Lambert, M. Kanj, and V. Menon. Wobbly and weak. wolff-parkinson-white associated cardiomyopathy because of intrinsic dyssynchrony. *Circulation: Heart Failure*, 11(8):e004981, 2018.

[72] G. Lecoq, C. Leclercq, E. Leray, C. Crocq, C. Alonso, C. de Place, P. Mabo, and C. Daubert. Clinical and electrocardiographic predictors of a positive response to cardiac resynchronization therapy in advanced heart failure. *European Heart Journal*, 26(11):1094–1100, 2005.

[73] A. Lee, U. Nguyen, O. Razeghi, J. Gould, B. Sidhu, B. Sieniewicz, J. Behar, M. Mafi-Rad, G. Plank, F. Prinzen, C. Rinaldi, K. Vernooy, and S. Niederer. A rule-based method for predicting the electrical activation of the heart with cardiac resynchronization therapy from non-invasive clinical data. *Medical Image Analysis*, 57:197–213, 2019.

[74] A. W. C. Lee, A. Crozier, E. R. Hyde, P. Lamata, M. Truong, M. Sohal, T. Jackson, J. M. Behar, S. Claridge, A. Shetty, E. Sammut, G. Plank, C. A. Rinaldi, and S. Niederer. Biophysical modeling to determine the optimization of left ventricular pacing site and av/vv delays in the acute and chronic phase of cardiac resynchronization therapy. *Journal of Cardiovascular Electrophysiology*, 28(2):208–215, 2017.

[75] Y. Liang, H. Yu, W. Zhou, G. Xu, Y. I. Sun, R. Liu, Z. Wang, and Y. Han. Left ventricular lead placement targeted at the latest activated site guided by electrophysio-

logical mapping in coronary sinus branches improves response to cardiac resynchronization therapy. *Journal of Cardiovascular Electrophysiology*, 26(12):1333–1339, 2015.

[76] J.-M. Lin, L.-P. Lai, C.-S. Lin, N.-K. Chou, C.-Y. Chiu, and J.-L. Lin. Left ventricular extracellular matrix remodeling in dogs with right ventricular apical pacing. *Journal of Cardiovascular Electrophysiology*, 21(10):1142–1149, 2010.

[77] L.-Y. Lin, Cho-KaiWu, J.-M. J. Juang, Yi-ChihWang, M.-Y. M. Su, L.-P. Lai, J.-J. Hwang, Fu-TienChiang, W.-Y. I. Tseng, and J.-L. Lin. Myocardial regional interstitial fibrosis is associated with left intra-ventricular dyssynchrony in patients with heart failure: A cardiovascular magnetic resonance study. *Scientific Reports*, 6(20711), 2016.

[78] A. M. Maceira, S. K. Prasad, M. Khan, and D. J. Pennell. Normalized left ventricular systolic and diastolic function by steady state free precession cardiovascular magnetic resonance. *Journal of Cardiovascular Magnetic Resonance*, 8:417–426, 2006.

[79] S. Marchesseau, H. Delingette, M. Sermesant, and N. Ayache. Fast parameter calibration of a cardiac electromechanical model from medical images based on the unscented transform. *Biomechanics and Modeling in Mechanobiology*, 12:815–831, 2013.

[80] Mayo Clinic. Bundle branch block. URL `https://www.mayoclinic.org/diseases-conditions/bundle-branch-block/diagnosis-treatment/drc-20370518`.

[81] W. Mazur and E. S. Chung. The role of echocardiography in cardiac resynchronization therapy. *Current Heart Failure Reports*, 6(1):37–43, 2009.

[82] K. S. McDowell, F. Vadakkumpadan, R. Blake, J. Blauer, G. Plank, R. S. MacLeod, and N. A. Trayanova. Methodology for patient-specific modeling of atrial fibrosis as a substrate for atrial fibrillation. *Journal of Electrocardiology*, 45:640–645, 2012.

[83] J. Moini. *Phlebotomy: Principles and Practice*, chapter 5, pages 35–51. Jones and Bartlett Publishers, 2013.

[84] M. P. Nash and A. V. Panfilov. Electromechanical model of excitable tissue to study reentrant cardiac arrhythmias. *Progress in Biophysics and Molecular Biology*, 85: 501–522, 2004.

[85] National Heart, Lung and Blood Institute, NIH. Arrhythmias, conduction disorders. URL `https://www.nhlbi.nih.gov/health/conduction-disorders`.

[86] A. Neic, F. O. Campos, A. J. Prassl, S. A. Niederer, M. J. Bishop, E. J. Vigmond, and G. Plank. Efficient computation of electrograms and ecgs in human whole heart simulations using a reaction-eikonal model. *Journal of Computational Physics*, 346: 191–211, 2017.

[87] S. Oiseth, L. Jones, and E. Maza. Bundle branch and fascicular blocks, 2022. URL `https://www.lecturio.com/concepts/bundle-branch-and-fascicular-blocks/`.

[88] S. Palamara, C. Vergara, E. Faggiano, and F. Nobile. An effective algorithm for the generation of patient-specific purkinje networks in computational electrocardiology. *Journal of Computational Physics*, 283:495–517, 2015.

[89] C. Pappone, Žarko Ćalović, G. Vicedomini, A. Cuko, L. C. McSpadden, K. Ryu, E. Romano, M. Saviano, M. Baldi, A. Pappone, C. Ciaccio, L. Giannelli, B. Ionescu, A. Petretta, R. Vital, A. Fundaliotis, L. Tavazzi, and V. Santinelli. Multipoint left ventricular pacing improves acute hemodynamic response assessed with pressure-volume loops in cardiac resynchronization therapy patients. *Heart Rhythm*, 11(3): 394–401, 2014.

[90] P.A.Stapleton, T.L.Knuckles, V.C.Minarchick, G.Gautam, and T.R.Nurkiewicz. Cardiovascular system. In *Encyclopedia of Toxicology*, volume 3, pages 730–747. Elsevier, 2014.

[91] J. Peirò and A. Veneziani. *Reduced models of the cardiovascular system*, pages 347–394. Springer Milan, 2009.

[92] G. B. Perego, R. Chianca, M. Facchini, A. Frattola, E. Balla, S. Zucchi, S. Cavaglià, I. Vicini, M. Negretto, and G. Osculati. Simultaneous vs. sequential biventricular pacing in dilated cardiomyopathy: an acute hemodynamic study. *The European Journal of Heart Failure*, 5:305–313, 2003.

[93] M. R. Pfaller, J. M. Hörmann, M. Weigl, A. Nagler, R. Chabiniok, C. Bertoglio, and W. A. Wall. The importance of the pericardium for cardiac biomechanics: from physiology to computational modeling. *Biomechanics and Modeling in Mechanobiology*, 18:503–529, 2019.

[94] E. R. Pfeiffer, J. R. Tangney, J. H. Omens, and A. D. McCulloch. Biomechanics

of cardiac electromechanical coupling and mechanoelectric feedback. *Journal of Biomechanical Engineering*, 136:021007, 2014.

[95] R. Piersanti, P. C. Africa, M. Fedele, C. Vergara, L. Dedè, A. F. Corno, and A. Quarteroni. Modeling cardiac muscle fibers in ventricular and atrial electrophysiology simulations. *Computer Methods in Applied Mechanics and Engineering*, 373:113468, 2021.

[96] A. Quarteroni and L. Formaggia. Mathematical modelling and numerical simulation of the cardiovascular system. In *Computational Models for the Human Body*, volume 12 of *Handbook of Numerical Analysis*, pages 3–127. Elsevier, 2004.

[97] A. Quarteroni and A. Veneziani. Modeling and simulation of blood flow problems. *Computational science for the 21st century*, pages 369–379, 1997.

[98] A. Quarteroni, T. Lassilaa, S. Rossia, and R. Ruiz-Baier. Integrated heart - coupling multiscale and multiphysics models for the simulation of the cardiac function. *Computer Methods in Applied Mechanics and Engineering*, 314:345–407, 2016.

[99] A. Quarteroni, A. Veneziani, and C. Vergara. Geometric multiscale modeling of the cardiovascular system, between theory and practice. *Computer Methods in Applied Mechanics and Engineering*, 302:193–252, 2016.

[100] A. Quarteroni, A. Manzoni, and C. Vergara. The cardiovascular system: Mathematical modelling, numerical algorithms and clinical applications. *Acta Numerica*, 26:365–590, 2017.

[101] F. Regazzoni, L. Dedè, and A. Quarteroni. Biophysically detailed mathematical models of multiscale cardiac active mechanics. *PLOS Computational Biology*, 16 (10):1–42, 2020.

[102] F. Regazzoni, L. Dedè, and A. Quarteroni. Machine learning of multiscale active force generation models for the efficient simulation of cardiac electromechanics. *Computer Methods in Applied Mechanics and Engineering*, 370:113268, 2020.

[103] F. Regazzoni, M. Salvador, P. C. Africa, M. Fedele, L. Dedè, and A. Quarteroni. A cardiac electromechanics model coupled with a lumped parameters model for closed-loop blood circulation. part i: model derivation, 2020. URL `https://arxiv.org/abs/2011.15040`.

[104] J. Relan, P. Chinchapatnam, M. Sermesant, K. Rhode, M. Ginks, H. Delingette, C. A. Rinaldi, R. Razavi, and N. Ayache. Coupled personalization of cardiac electro-

physiology models for prediction of ischaemic ventricular tachycardia. *Biomechanics and Modeling in Mechanobiology*, 1:396–407, 2011.

[105] M. Reumann, D. Farina, R. Miri, S. Lurz, B. Osswald, and O. Dössel. Computer model for the optimization of av and vv delay in cardiac resynchronization therapy. *Medical and Biological Engineering and Computing*, 45:845–854, 2007.

[106] C. A. Rinaldi, C. Leclercq, W. Kranig, S. Kacet, T. Betts, P. Bordachar, K.-J. Gutleben, A. Shetty, E. Donal, A. Keel, K. Ryu, T. G. Farazi, M. Simon, and T. Z. Naqvi. Improvement in acute contractility and hemodynamics with multipoint pacing via a left ventricular quadripolar pacing lead. *Journal of Interventional Cardiac Electrophysiology*, 40:75–80, 2014.

[107] G. Savarese, P. M. Becher, L. H. Lund, P. Seferovic, G. M. Rosano, and A. J. Coats. Global burden of heart failure: a comprehensive and updated review of epidemiology. *Cardiovascular Research*, 0:1–16, 2022.

[108] M. Sermesant, R. Chabiniok, P. Chinchapatnam, T. Mansi, F. Billet, P. Moireau, J. Peyrat, K. Wong, J. Relan, K. Rhode, M. Ginks, P. Lambiase, H. Delingette, M. Sorine, C. Rinaldi, D. Chapelle, R. Razavi, and N. Ayache. Patient-specific electromechanical models of the heart for the prediction of pacing acute effects in crt: A preliminary clinical validation. *Medical Image Analysis*, 16(1):201–215, 2011.

[109] J. P. Singh, H. U. Klein, D. T. Huang, S. Reek, M. Kuniss, A. Quesada, A. Barsheshet, D. Cannom, I. Goldenberg, S. McNitt, J. P. Daubert, W. Zareba, and A. J. Moss. Left ventricular lead position and clinical outcome in the multi-center automatic defibrillator implantation trial–cardiac resynchronization therapy (madit-crt) trial. *Circulation*, 123(11):1159–1166, 2011.

[110] P. Sogaard, H. Egeblad, A. K. Pedersen, W. Y. Kim, B. O. Kristensen, P. S. Hansen, and P. T. Mortensen. Sequential versus simultaneous biventricular resynchronization for severe heart failure. *Circulation*, 106(16):2078–2084, 2002.

[111] M. Spartalis, E. Tzatzaki, E. Spartalis, C. Damaskos, A. Athanasiou, E. Livanis, and V. Voudris. Pathophysiology and current evidence for detection of dyssynchrony. *Cardiology Research*, 8(5):179—183, 2017.

[112] P. Steendijk, S. A. Tulner, J. J. Bax, P. V. Oemrawsingh, G. B. Bleeker, L. van Erven, H. Putter, H. F. Verwey, E. E. van der Wall, and M. J. Schalij. Hemodynamic effects of long-term cardiac resynchronization therapy. *Circulation*, 113(10):1295–1304, 2006.

[113] S. Stella. *Data-driven mathematical and numerical models for the ventricular elec-tromechanics with application to cardiac resynchronization therapy*. PhD thesis, Politecnico di Milano, 2021.

[114] S. Stella, C. Vergara, M. Maines, D. Catanzariti, P. C. Africa, C. Demattè, M. Centonze, F. Nobile, M. Del Greco, and A. Quarteroni. Integration of activation maps of epicardial veins in computational cardiac electrophysiology. *Computers in Biology and Medicine*, 127:104047, 2020.

[115] S. Stella, F. Regazzoni, C. Vergara, L. Dedè, and A. Quarteroni. A fast cardiac electromechanics model coupling the eikonal and the nonlinear mechanics equations. *MOX-Report*, 59:1–24, 2021.

[116] M. Strocchi, C. M. Augustin, M. A. F. Gsell, E. Karabelas, A. Neic, K. Gillette, O. Razeghi, A. J. Prassl, E. J. Vigmond, J. M. Behar, J. Gould, B. Sidhu, C. A. Rinaldi, M. J. Bishop, G. Plank, and S. A. Niederer. A publicly available virtual cohort of four-chamber heart meshes for cardiac electro-mechanics simulations. *PLOS ONE*, 15(6):1–26, 2020.

[117] M. Strocchi, M. A. Gsell, C. M. Augustin, O. Razeghi, C. H. Roney, A. J. Prassl, E. J. Vigmond, J. M. Behar, J. S. Gould, C. A. Rinaldi, M. J. Bishop, G. Plank, and S. A. Niederer. Simulating ventricular systolic motion in a four-chamber heart model with spatially varying robin boundary conditions to model the effect of the pericardium. *Journal of Biomechanics*, 101:109645, 2020.

[118] M. G. S. J. Sutton, T. Plappert, W. T. Abraham, A. L. Smith, D. B. DeLurgio, A. R. Leon, E. Loh, D. Z. Kocovic, W. G. Fisher, M. Ellestad, J. Messenger, K. Kruger, K. E. Hilpisch, and M. R. Hill. Effect of cardiac resynchronization therapy on left ventricular size and function in chronic heart failure. *Circulation*, 107(15):1985–1990, 2003.

[119] H. Suzuki, M. Shimano, Y. Yoshida, Y. Inden, T. Muramatsu, Y. Tsuji, N. Tsuboi, H. Hirayama, R. Shibata, and T. Murohara. Maximum derivative of left ventricular pressure predicts cardiac mortality after cardiac resynchronization therapy. *Clinical Cardiology*, 33(12):E18–23, 2010.

[120] M. Sweeney, B. Corden, and S. A. Cook. Targeting cardiac fibrosis in heart failure with preserved ejection fraction: mirage or miracle? *EMBO Molecular Medicine*, 12:e10865, 2020.

[121] F. Tabrizi, A. Englund, M. Rosenqvist, L. Wallentin, and U. Stenestrand. Influ-

ence of left bundle branch block on long-term mortality in a population with heart failures. *European Heart Journal*, 28:2449–2455, 2007.

[122] N. Y. Tan, C. M. Witt, J. K. Oh, and Y.-M. Cha. Left bundle branch block. current and future perspectives. *Circulation: Arrhythmia and Electrophysiology*, 13 (4):e008239, 2020.

[123] K. H. W. J. ten Tusscher and A. V. Panfilov. Alternans and spiral breakup in a human ventricular tissue model. *American Journal of Physiology-Heart and Circulatory Physiology*, 291(3):H1088–H1100, 2006.

[124] B. Thibault, M. Dubuc, P. Khairy, P. G. Guerra, L. Macle, L. Rivard, D. Roy, M. Talajic, E. Karst, K. Ryu, P. Paiement, and T. G. Farazi. Acute haemodynamic comparison of multisite and biventricular pacing with a quadripolar left ventricular lead. *Europace*, 15:984–991, 2012.

[125] C. Thébault, E. Donal, C. Meunier, R. Gervais, B. Gerritse, M. R. Gold, W. T. Abraham, C. Linde, and f. t. R. s. g. J. Claude Daubert. Sites of left and right ventricular lead implantation and response to cardiac resynchronization therapy observations from the reverse trial. *European Heart Journal*, 33(21):2662–2671, 2012.

[126] N. A. Trayanova and R. Winslow. Whole-heart modeling. *Circulation Research*, 108(1):113–128, 2011.

[127] K. H. W. J. T. Tusscher, A. Mourad, M. P. Nash, R. H. Clayton, C. P. Bradley, D. J. Paterson, R. Hren, M. Hayward, A. V. Panfilov, and P. Taggart. Organization of ventricular fibrillation in the human heart: experiments and models. *Experimental Physiology*, 94:553–562, 2009.

[128] W. van Everdingen, J. Schipper, J. van't Sant, K. R. Misier, M. Meine, and M. Cramer. Echocardiography and cardiac resynchronisation therapy, friends or foes? *Netherlands Heart Journal*, 24(1):25–38, 2015.

[129] C. Vergara, S. Palamara, D. Catanzariti, F. Nobile, E. Faggiano, C. Pangrazzi, M. Centonze, M. Maines, A. Quarteroni, and G. Vergara. Patient-specific generation of the purkinje network driven by clinical measurements of a normal propagation. *Medical and Biological Engineering and Computing*, 52:813–826, 2014.

[130] C. Vergara, M. Lange, S. Palamara, T. Lassila, A. F. Frangi, and A. Quarteroni. A coupled 3d–1d numerical monodomain solver for cardiac electrical activation in

the myocardium with detailed purkinje network. *Journal of Computational Physics*, 308:218–238, 2016.

[131] C. Vergara, S. Stella, M. Maines, D. Catanzariti, C. Demattè, M. Centonze, F. Nobile, A. Quarteroni, and M. Del Greco. Computational electrophysiology to support the mapping of coronary sinus branches for cardiac resynchronization therapy. *MOX-Report*, 84:1–24, 2020.

[132] C. T. Villongco, D. E. Krummen, J. H. Omens, and A. D. McCulloch. Non-invasive, model-based measures of ventricular electrical dyssynchrony for predicting crtoutcomes. *Europace*, 18(4):iv104–iv112, 2016.

[133] S. T. Wall, J. M. Guccione, M. B. Ratcliffe, and J. S. Sundnes. Electromechanical feedback with reduced cellular connectivity alters electrical activity in an infarct injured left ventricle: a finite element model study. *American Journal of Physiology-Heart and Circulatory Physiology*, 302(1):H206–H214, 2012.

[134] N. Westerhof, J.-W. Lankhaar, and B. E. Westerhof. The arterial windkessel. *Medical and Biological Engineering and Computing*, 47:131–141, 2009.

[135] Z. I. Whinnett, D. P. Francis, A. Denis, K. Willson, P. Pascale, I. van Geldorp, M. D. Guillebon, S. Ploux, K. Ellenbogen, M. Haïssaguerre, P. Ritter, and P. Bordachar. Comparison of different invasive hemodynamic methods for av delay optimization in patients with cardiac resynchronization therapy: Implications for clinical trial design and clinical practice. *International Journal of Cardiology*, 168:2228–2237, 2013.

[136] World Health Organization. Cardiovascular diseases (cvds), 2021. URL `https://www.who.int/`.

[137] J. Xi, P. Lamata, J. Lee, P. Moireau, D. Chapelle, and N. Smith. Myocardial transversely isotropic material parameter estimation from in-silico measurements based on a reduced-order unscented kalman filter. *Journal of the Mechanical Behavior of Biomedical Materials*, 4(7):1090–1102, 2011.

[138] C. Ypenburg, R. J. van Bommel, V. Delgado, S. A. Mollema, G. B. Bleeker, E. Boersma, M. J. Schalij, and J. J. Bax. Optimal left ventricular lead position predicts reverse remodeling and survival after cardiac resynchronization therapy. *Journal of the American College of Cardiology*, 52(17):1402–1409, 2008.

[139] C.-M. Yu, H. Lin, Q. Zhang, and J. E. Sanderson. High prevalence of left ventricular

systolic and diastolic asynchrony in patients with congestive heart failure and normal qrs duration. *Heart*, 89(1):54–60, 2003.

[140] F. Zanon, E. Baracca, G. Pastore, C. Fraccaro, L. Roncon, S. Aggio, F. Noventa, A. Mazza, and F. Prinzen. Determination of the longest intrapatient left ventricular electrical delay may predict acute hemodynamic improvement in patients after cardiac resynchronization therapy. *Circulation: Arrhythmia and Electrophysiology*, 7(3):377–383, 2014.

[141] F. Zanon, E. Baracca, G. Pastore, L. Marcantoni, C. Fraccaro, D. Lanza, C. Picariello, S. Aggio, L. Roncon, F. Dell'Avvocata, G. Rigatelli, D. Pacetta, F. Noventa, and F. W. Prinzen. Multipoint pacing by a left ventricular quadripolar lead improves the acute hemodynamic response to crt compared with conventional biventricular pacing at any site. *Heart Rhythm Society*, 12(5):975–981, 2015.

List of Figures

List of Tables

List of Acronyms

CVDs Cardiovascular Diseases

CRT Cardiac Resynchronization Therapy

LBBB Left Bundle Branch Block

VD Ventricular Dyssynchrony

RA Right Atrium

LA Left Atrium

RV Right Ventricle

LV Left Ventricle

CCS Cardiac Conduction System

CS Coronary Sinus

AP Action Potential

IVC Isovolumetric Contraction

IVR Isovolumetric Relaxation

EDV End Diastolic Volume

ESV End Systolic Volume

SV Stroke Volume

EF Ejection Fraction

SW Stroke Work

IVC Isovolumetric Contraction

IVR Isovolumetric Relaxation

HF Heart Failure

ECG/EKG Electrocardiogram

CMRI Cardiac Magnetic Resonance Imaging

CT Computed Tomography

TDI Tissue Doppler Imaging

STE Speckle Tracking Echocardiography

SPWMD Septal to Posterior Wall Motion Delay

IVMD Interventricular Mechanical Delay

SD Standard Deviation

SDI Systolic Dyssynchrony Index

ICD Implantable Cardioverter Defibrillator

HR Heart Rate

CO Cardiac Output

EDP End Diastolic Pressure

ESP End Systolic Pressure

PP Pulse Pressure

LEAS Latest Electrically Activated Segment

RR Reverse Remodeling

AVD Atrio-Ventricular Delay

VVD Ventriculo-Ventricular Delay

ODE Ordinary Differential Equation

PDE Partial Differential Equation

DAE Differential Algebraic Equation

EM Electromechanical

EP Electrophysiology

FSI Fluid-structure Interaction

EFSI Electrical Fluid-structure Interaction

CFD Computational Fluid Dynamics

DCM Dilated Cardiomyopathy

MI Myocardial Infarction

RE Reaction-Eikonal

ERM Eikonal-Reaction-Mechanics

RDQ20-MF Regazzoni Dedè Quarteroni 2020 - Mean Field

BDF Backward Differentiation Formula

FEM Finite Element Method

EAMS Electro-Anatomical Mapping System

BC Boundary Conditions